

An ab initio Study
of
Electronic States and Transitions
of
Tellurium Monohalides

a Dissertation submitted to the Faculty of Chemistry
of the Bergische Universität Wuppertal
in partial fulfillment of
the requirements for the degree of
Doctor of Natural Science
(Dr. rer. nat.)

by
Vidisha Rai
from Varanasi

Wuppertal 2002

Acknowledgement

It is my pleasure to thank Professor Robert J. Buenker for suggesting the theme of the dissertation and for his valuable guidance through each stage of my work.

I am very grateful to my parents for their support all through my work. I would like to specially thank my father for his very helpful suggestions and discussions during my work.

I express my most sincere thank to late Dr. Gerhard Hirsch for his very helpful discussions and his guidance during the initial stages of my work.

My warmest thanks are due to Herr Heinz-Peter Liebermann for his invaluable discussions and guidance to using the programs employed in the calculations. His suggestions have been of immense help to me during the whole course of my work. I would also like to express my thanks to Herr Peter Funke for his continual help with all the technical problems related to the computer.

I would like to express my appreciation to Dr. A. B. Alekseyev for taking time for invaluable discussions with me. His suggestions and guidance have been of immense help to me throughout. I would also like to thank my colleague Herr Rainer Lingott for his ready help regarding my doubts and questions.

My most sincere thanks are also due to all the faculty members and friends who have been wishing me luck during the course of my work.

Lebenslauf

Angaben zur Person

Name: Vidisha Rai
Geburtsdatum: 9. 12. 1974
Geburtsort: Varanasi, Indien
Familienstand: ledig

Ausbildung

1990: High School
1990 - 1992: Pre-University
1992 - 1995: Bachelor of Science (with Honours in Chemistry)
an der North-Eastern Hill University, Shillong, Indien
1995 - 1997: Masters of Science (in Chemistry)
an der North-Eastern Hill University, Shillong, Indien
1. 6. 1998: Beginn der Promotion bei Prof. Dr. R. J. Buenker
an der Bergischen Universität Wuppertal
seit 1. 6. 1998: tätig als wissenschaftliche Mitarbeiterin
im Arbeitskreis von Prof. Dr. R. J. Buenker
23. 9. 2001 - 27. 9. 2001: Teilnahme am
Symposium für Theoretische Chemiker 2001, Heidelberg
16. 9. 2002 - 20. 9. 2002: Teilnahme an
der SPHERS Summer School

Contents

Introduction	3
1 Theoretical Background	9
1.1 Born-Oppenheimer Approximation	9
1.2 Hartree-Fock Approximation	13
1.3 Roothaan SCF-LCAO-MO Method	16
1.4 Configuration Interaction	19
1.5 MRD-CI Method	20
1.6 Pseudopotential Theory	23
1.7 Pseudopotentials in Molecular Calculations	24
1.8 Relativistic Effects	27
1.9 Spectroscopic Properties using the CI Wave Functions	28
2 Tellurium Fluoride (TeF)	31
2.1 Details of the Theoretical Treatment	31
2.2 Potential Curves	35
2.3 Transition Moments and Radiative Lifetimes	42
3 Tellurium Chloride (TeCl)	53
3.1 Details of the Theoretical Treatment	53

3.2	Potential Curves	56
3.3	Transition Moments and Radiative Lifetimes	61
4	Tellurium Bromide (TeBr)	67
4.1	Details of the Theoretical Treatment	67
4.2	Potential Curves	70
4.3	Transition Moments and Radiative Lifetimes	74
5	Tellurium Iodide (TeI)	81
5.1	Details of the Theoretical Treatment	81
5.2	Potential Curves	84
5.3	Transition Moments and Radiative Lifetimes	88
	Conclusion	93
	References	95
	List of Tables	99
	List of Figures	101

Introduction

Group VI is the last main group which contains an element which is metallic, polonium. Oxygen and sulphur are insulators whereas selenium and tellurium behave as semiconductors. From top to bottom of the group, atomic sizes increase and electronegativity decreases. The ionization energies fall steadily down the group. All elements have the electronic structure s^2p^4 . Whereas oxygen and sulphur have only s and p electrons, others have d electrons as well.

Oxygen is the most important element in the group. Besides being the most abundant of all the elements, making up about 49.4 % of the earth's crust and 23 % (by weight) of the atmosphere, oxygen reacts with almost all other elements. Sulphur, selenium and tellurium are moderately active whereas polonium is strongly radioactive. Also, oxygen differs from the rest of the group in that it is more electronegative and therefore more ionic in its compounds.

In comparison to their corresponding IV A elements, the group VI elements are more easily volatilized. Also in forming compounds with the halogens, elements of the group VI show valencies of 2, 4 and 6. In addition, all elements readily form covalent hydrides. All these combined with other experimental intricacies make observation of clean spectra of diatomic halides of these elements more cumbersome. As a matter

of fact, present knowledge about the spectroscopic properties of the group VI monohalides is quite limited.

A thorough survey of literature and search through the Huber-Herzberg compendium [1] and database for diatomic molecules [2] reveal that although oxygen monohalides because of their importance in atmospheric processes are most studied, information on other group VI monohalides is rather meagre. Among sulphur monohalides, only the lightest SF radical is mentioned in the Huber-Herzberg compendium [1], and even in this case the spectroscopic data reported are far from complete and the assignment of the only known excited state as $A^2\Pi$ is not reliable. In the case of selenium monohalides, spectroscopic constants are available for three systems, SeF, SeCl, and SeBr [1,3], but this information is also limited and tentative. No other data for the above systems have come to our attention so far.

Remarkably, more is known about the spectroscopy of tellurium monohalides [4-12]. Oldershaw et al. [4-6] observed the UV absorption spectra of TeCl, TeBr and TeI. They assigned most of the observed bands to $B \rightarrow X_1^2\Pi_{3/2}$ and $B \rightarrow X_2^2\Pi_{1/2}$ transitions. Assuming that there is no fine-structure splitting in the B state, Huber and Herzberg [1] report the doublet splittings of the ground states to be 1674 (TeCl), 1719 (TeBr), and 1815 (TeI) cm^{-1} . In 1979, Newlin et al. [7] observed the chemiluminescence emission spectrum of TeF from a mixture of H_2Te/D_2Te with fluorine in the region of 3900 – 5200 Å and assigned it to $A(^2\Pi_i) \rightarrow X(^2\Pi_i)(i = 1/2 \text{ or } 3/2)$ transitions based on analogy with the SF radical [13]. They reported the difference in spin-orbit constants for the ground and excited states to be 394 cm^{-1} . In the following investigations of the lower-lying states of TeF, Newlin et al. [8] observed the corresponding transitions in the 5000 – 8000 Å region and reassigned the previously observed spectrum [7] to $B^2\Sigma^+ \rightarrow X(^2\Pi_i)$ transitions. They also estimated the spin-orbit constants for the ground

$X(^2\Pi_i)$ and $A(^2\Pi_i)$ states as $X(^2\Pi) = -531\text{ cm}^{-1}$, and $A(^2\Pi) = -909\text{ cm}^{-1}$. Thorpe et al. [9] in 1985 observed the same band systems from the chemiluminescence reactions produced by heating metallic tellurium in the presence of fluorine. They assigned the bands to the transitions $B^2\Sigma^+ \rightarrow X_1^2\Pi_{3/2}$ and $B^2\Sigma^+ \rightarrow X_2^2\Pi_{1/2}$ (in the region extending from approximately 3800 – 5400 Å) and $A^2\Pi_{3/2} \rightarrow X_1^2\Pi_{3/2}$ and $A^2\Pi_{1/2} \rightarrow X_2^2\Pi_{1/2}$ (in the region extending from above 5300 Å). They reported the spin-orbit coupling of the $X(^2\Pi_i)$ state to be -497 cm^{-1} , as determined from the $^2\Sigma^+ - ^2\Pi_i$ transition. Fink and coworkers [10-12] reported high-resolution Fourier transform emission spectra for all four tellurium monohalides in the near-infrared spectral region. They analysed the 0 – 0 bands of the transitions $X_2^2\Pi_{1/2} \rightarrow X_1^2\Pi_{3/2}$ in TeF, TeCl, TeBr, and TeI and determined the fine-structure splittings of the $X(^2\Pi_i)$ ground states to be $4187 \pm 1\text{ cm}^{-1}$ for TeF, $4022.5 \pm 1\text{ cm}^{-1}$ for TeCl, $4067 \pm 3\text{ cm}^{-1}$ for TeBr, and $4130 \pm 10\text{ cm}^{-1}$ for TeI.

It is always useful to analyse the results reported for less studied systems with those for previously more extensively investigated similar systems. Since TeF is isovalent with OF, it was natural to expect a $\sigma^2\pi^4\pi^{*3}$ electronic configuration for its ground state and that its lowest excited state would result from a $\pi \rightarrow \pi^*$ transition. Relativistic configuration interaction (CI) calculations for another halogen monoxide, IO [14], have shown, however, that in this case the lowest excited state is $^4\Sigma^-$, which results from a $\pi^* \rightarrow \sigma^*$ excitation relative to its $\sigma^2\pi^4\pi^{*3}$ ground state. Spin-orbit effects cause the $^4\Sigma^-$ state to have a regular multiplet ordering ($1/2 < 3/2$) as opposed to the inverted order expected and observed for the $^2\Pi$ state. This is an interesting result because in many ways IO and TeF are complementary systems. They both are group VIA halides with one atom from each of the first and fourth rows of the periodic table, but they differ in the way this selection is made. This distinction can be expected to produce significant differences in the bonding and antibonding character of their respective molecular orbitals (MOs) because of the contrasting electronegativity relationships between these

two pairs of constituent atoms. In TeF the electronic charge distribution is expected to be far more polar than is the case in IO, for which the electronegativity difference of its constituents is much smaller. Experience with group VA halides [15-19] has demonstrated that the degree of antibonding in the π^* and σ^* MOs markedly decreases with the increased polarity of the system and this in turn produces qualitative differences in the shapes of potential curves for states with equivalent electronic configurations. The relative strengths of electronic transitions can also be greatly affected by such considerations. They also can have a significant impact on the magnitude of spin-orbit splittings, particularly in the present case where the two atoms come from widely differing rows of the periodic table. In this case the key question is what is the composition of the open-shell MO most responsible for the splitting, particularly what portion of it is derived from the heavier atom. In IO the $X^2\Pi$ zero-field splitting is only 2091 cm^{-1} [20], which is a little more than one-quarter of the corresponding value for atomic iodine, a clear indication of the high proportion of oxygen character in this system's π^* MO. One expects the corresponding MO in TeF to be heavily localized on the tellurium atom, causing significantly larger spin-orbit splitting for this system. One also expects the π^* and σ^* orbitals to be far less antibonding in TeF for the same reason. These distinctions should also play a key role in determining whether $\pi \rightarrow \pi^*$ or $\pi^* \rightarrow \sigma^*$ transitions produce the lowest excited state in this system. Also, based on their interpretation of spin-orbit constants, Fink et al. [10] emphasized the need of re-investigation of the $A \rightarrow X$ and $B \rightarrow X$ systems of the tellurim halides including quantum-mechanical calculations of the corresponding energy levels and transitions moments.

For other monohalides of tellurium, TeCl, TeBr, and TeI, knowledge about the spectroscopic properties is still more obscure than for TeF. Although spectroscopic constants for the X_1 and X_2 states of TeCl have been determined experimentally [11], for TeBr and TeI no observed results except for the ground state splittings can be found in

the literature. Over all, the accuracy of experimental determination of relative quantities such as radiative lifetimes and whether the transitions are electric or magnetic dipole in nature are always rather limited. Under these circumstances, quantum mechanical *ab initio* calculations often provide the best means of obtaining reliable estimates and aid experimentalists in developing new techniques to increase the accuracy of their measurements.

In order to study the points discussed above, a series of *ab initio* spin-orbit configuration interaction (SO-CI) calculations have been carried out for the first time for TeX (X=F, Cl, Br, and I) radicals by employing relativistic effective core potentials (RECPs). The methods employed are particularly well suited for computing energy-related quantities and determining electric-dipole transition moments. A large number of such applications have already been reported [15-19,21-24]. Energetic properties, dipole transition moments and radiative lifetimes have been computed for a number of low-lying states which have been studied experimentally [7-12], and predictions regarding the strongest transitions in the low-energy spectra of these systems have been made which should be useful for future spectroscopic investigations.

The remainder of this dissertation is organised as follows. In Chapter 1, the salient features of the theoretical methods employed in the present studies have been described. Results obtained from the present calculations, their interpretation, and comparisons with available experimental data for TeF, TeCl, TeBr, and TeI are reported in Chapters 2, 3, 4, and 5, respectively.

Chapter 1

Theoretical Background

1.1 Born-Oppenheimer Approximation

The wave function $|\Psi(r, R)\rangle$, obtained as a solution of the time-independent Schrödinger equation:

$$(\hat{H}(r, R) - E)\Psi(r, R) = 0 \quad (1.1)$$

describes an atom or a molecule in non-relativistic quantum mechanics. Here r and R are the coordinates of the electrons and the nuclei of the system, respectively. The non-relativistic Hamilton operator \hat{H} can be written as:

$$\hat{H}(r, R) = \hat{T}^N(R) + \hat{H}_R^{el}(r) \quad (1.2)$$

where

$$\hat{T}^N \equiv \hat{T}^N(R) = -\frac{1}{2} \sum_K \frac{1}{M_K} \nabla_K^2$$

$$\begin{aligned}
\hat{H}_R^{el}(r) &= -\frac{1}{2} \sum_i \nabla_i^2 - \sum_{i,K} \frac{Z_K}{r_{iK}} + \sum_{i<j} \frac{1}{r_{ij}} + \sum_{K<L} \frac{Z_K Z_L}{R_{KL}} \\
&= \sum_i \left[-\frac{1}{2} \nabla_i^2 - \sum_K \frac{Z_K}{r_{iK}} \right] + \sum_{i<j} \frac{1}{r_{ij}} + \sum_{K<L} \frac{Z_K Z_L}{R_{KL}} \\
&\equiv \sum_i \hat{h}^{el}(i) + \sum_{i<j} \frac{1}{r_{ij}} + \sum_{K<L} \frac{Z_K Z_L}{R_{KL}}
\end{aligned}$$

and

$$\vec{r}_i \equiv \begin{pmatrix} x_i \\ y_i \\ z_i \end{pmatrix}, \quad \vec{R}_K \equiv \begin{pmatrix} X_K \\ Y_K \\ Z_K \end{pmatrix},$$

$$\nabla_i^2 = \frac{\partial^2}{\partial x_i^2} + \frac{\partial^2}{\partial y_i^2} + \frac{\partial^2}{\partial z_i^2}$$

$$\nabla_K^2 = \frac{\partial^2}{\partial X_K^2} + \frac{\partial^2}{\partial Y_K^2} + \frac{\partial^2}{\partial Z_K^2}$$

$$r_{iK} \equiv |\vec{r}_i - \vec{R}_K|, \quad r_{ij} \equiv |\vec{r}_i - \vec{r}_j|, \quad R_{KL} \equiv |\vec{R}_K - \vec{R}_L|$$

It is obvious that atomic units are used. Here \hat{T}^N is the kinetic energy operator of the nuclei and $\hat{H}_R^{el}(r)$ is the non-relativistic electronic Hamiltonian operator (for fixed nuclear coordinates R). The nuclear mass and charge are represented by M_K and Z_K , respectively¹. The position vectors of i^{th} electron and the K^{th} nucleus in the system are \vec{r}_i and \vec{R}_K , respectively. It is assumed that electrons and the nuclei are point mass/charges. Also, all the nuclear and electronic coordinates have been referred to the centre of mass of the system. The total energy of an atom can be seen as that of the electrons relative to a stationary center of mass. In a molecule, the energy consists

¹Block letters have been used to label the nuclear terms and small letters for the electronic terms.

of contributions from several different types of motion, namely, that of the electrons, vibrational motion of the nuclei, and rotational motion of the nuclei. To make matters more complex, all these motions couple with each other, making the solution of equation (1.1) a challenging problem.

A starting point for computational, structural tools is the Born-Oppenheimer approximation. It is an extremely significant concept, because it is only within the Born-Oppenheimer separation of electronic and nuclear motion that a potential energy surface exists. The equilibrium structure of a species corresponds to a minimum on such a surface. Moreover, the approximation reduces the complete quantum mechanical problem to one of electronic structure, as shall be discussed later, in this section.

According to Born and Oppenheimer [25], the solutions of the Schrödinger equation (1.1) can be expanded in a power series in the quantity $M^{-1/4}$ (where M is the average mass of the nuclei). If this function is very much smaller than unity, then one can approximate solutions to equation (1.1) by first solving the wave equation for a series of fixed nuclear positions, thus obtaining the electronic energy for a particular arrangement of nuclei. This electronic energy (which depends on the nuclear positions) can then be used as the potential energy for the wave function involving the nuclei alone.

The Born-Oppenheimer approximation in simple quantitative terms amounts to separating off the nuclear kinetic energy terms from the total Hamiltonian, and considering only the part which depends on the positions but not on the momenta of the nuclei. The physical picture leading to this approximation is quite simple. Both electrons and nuclei experience forces of equal magnitude ($F = ma$). Due to their heavier mass, the nuclei move much more slowly in the center-of-mass coordinate system as

compared to the electrons of the system. Hence, it is possible to approximate the real system to be one in which the electrons move in the field of fixed nuclei.

According to this approximation then, one can write the total wave function as

$$\Psi(r, R) = \Phi_R(r)\chi(R), \quad (1.3)$$

where $\Phi_R(r)$ is an electronic wave function for fixed nuclear coordinates and $\chi(R)$ are the corresponding nuclear wave functions, and

$$\hat{H}_R^{el}(r)\Phi(r, R) = E_{el}(R)\Phi(r, R), \quad (1.4)$$

where $E_{el}(R)$ is the electronic energy and depends on the nuclear coordinates. The total energy for fixed nuclei also includes the constant nuclear repulsion term

$$\sum_{A=1}^M \sum_{B>A}^M \frac{Z_A Z_B}{R_{AB}}$$

R_{AB} being the internuclear separation between nuclei A and B , and M is the total number of nuclei in the system.

Once the electronic problem has been solved, one can subsequently solve the nuclear Schrödinger equation using the same assumptions which were used to formulate the electronic problem. Since the motion of the electrons is much faster than that of the nuclei, in equation (1.2) the electronic coordinates can be replaced by their values obtained by averaging over the electronic wave function. The nuclear Hamiltonian thus

generated is:

$$\begin{aligned}
 \hat{H}_{nucl} &= -\sum_{A=1}^M \frac{1}{M_A} \nabla_A^2 + \left\langle -\sum_{i=1}^N \frac{1}{2} \nabla_i^2 - \sum_{i=1}^N \sum_{A=1}^M \frac{Z_A}{r_{iA}} + \sum_{i=1}^N \sum_{j>i}^N \frac{1}{r_{ij}} \right\rangle + \sum_{A=1}^M \sum_{B>A}^M \frac{Z_A Z_B}{R_{AB}} \\
 &= -\sum_{A=1}^M \frac{1}{M_A} \nabla_A^2 + E_{el}(R) + \sum_{A=1}^M \sum_{B>A}^M \frac{Z_A Z_B}{R_{AB}} \\
 &= -\sum_{A=1}^M \frac{1}{M_A} \nabla_A^2 + E_{tot}(R) \tag{1.5}
 \end{aligned}$$

where N is the total number of electrons in the system. The total energy $E_{tot}(R)$ provides a potential for the nuclear motion that constitutes a potential energy surface. The nuclei in the Born-Oppenheimer approximation move on a potential surface obtained by solving the electronic Schrödinger equation.

1.2 Hartree-Fock Approximation

Another approximation central to solving the many-electron problem in quantum chemistry is the Hartree-Fock approximation. The basic idea underlying this approach is to treat the relatively complicated many-electron interaction as a one-electron problem in which electron-electron repulsion is treated in an average way. Physically, the approximation is a neglect of instantaneous electron-electron repulsions. Within it electrons see each other as distributions in space rather than as individual particles.

It is assumed that each electron is described by a Schrödinger equation for an electron moving in an effective field. This effective field includes the field arising from the nuclei of the molecule, as well as the average field created by the other electrons. Following separation of the many-electron Schrödinger equation (as discussed above),

the one-electron Schrödinger equation can be written as

$$(h_i + u_i)\phi_i = E_i\phi_i, \quad (1.6)$$

where u_i is the average field and h_i is the one-electron operator

$$h_i = -\frac{1}{2}\nabla_i^2 + \sum_{A=1}^M \left(-\frac{Z_A}{r_{iA}} \right), \quad (1.7)$$

and the wave function ϕ_i depends on the coordinates of a single electron i only. The difficulty here is that the potential u_i is unknown and depends on the one-electron wave functions of all the other electrons in the molecule. An initial guess has to be then made for u_i . The one-electron Schrödinger equation (1.6) is then solved for this u_i to obtain a set of orbitals which are then used to construct an improved potential u_i . The one-electron Schrödinger equations are then solved repeatedly to obtain improvements over the initial guess. The process is continued until the orbitals describing the movement of the electrons do not change. Each electron is then said to be moving in a self-consistent field (SCF).

It is to be noted that the spin of the electrons has to be taken into consideration, as well as the condition that the wave function for the N -electron system be antisymmetric with respect to permutation of both the spin and space coordinates of the electrons. The wave function of the N -electron system is, hence, represented by an antisymmetrized product of spin orbitals ψ such that

$$\psi_i = \phi_i\alpha$$

or,

$$\psi_i = \phi_i \beta,$$

where α and β are two spin functions, corresponding to spin up and down, respectively.

The total wave function can be written as a Slater determinant [26]:

$$\Phi = (N!)^{-1/2} \begin{vmatrix} \psi_1(\tau_1) & \psi_2(\tau_1) & \cdots & \psi_N(\tau_1) \\ \psi_1(\tau_2) & \psi_2(\tau_2) & \cdots & \psi_N(\tau_2) \\ \vdots & \vdots & \ddots & \vdots \\ \psi_1(\tau_N) & \psi_2(\tau_N) & \cdots & \psi_N(\tau_N) \end{vmatrix} \quad (1.8)$$

where the τ_i is the space coordinate of the i^{th} electron.

The best solution of equation (1.8) is chosen by invoking the variational theorem according to which the Rayleigh quotient:

$$\frac{\langle \Phi | \hat{H} | \Phi \rangle}{\langle \Phi | \Phi \rangle} = \frac{\int \int \cdots \int \Phi^* \hat{H} \Phi d\tau_1 d\tau_2 \cdots d\tau_N}{\int \int \cdots \int \Phi^* \Phi d\tau_1 d\tau_2 \cdots d\tau_N} \quad (1.9)$$

provides an upper bound to the exact solution of the Schrödinger equation for any choice of approximate wave function Φ . A wave equation of the form (1.8) is associated with a total energy, in this case the electronic energy:

$$E_{el} = 2 \sum_i H_{ii}^{core} + \sum_{i,j} (2J_{ij} - K_{ij}) \quad (1.10)$$

where H_{ii}^{core} is the core Hamiltonian matrix element, J_{ij} is the Coloumb integral, and

K_{ij} is the exchange integral, defined as follows:

$$H_{ii}^{core} = \left\langle \psi_i \left| -\frac{\hbar^2}{2m} \Delta_1 - \sum_A \frac{Z_A}{r_{1A}} \right| \psi_i \right\rangle \quad (1.11)$$

$$J_{ij} = \left\langle \psi_i(r_1)\psi_j(r_2) \left| \frac{1}{r_{12}} \right| \psi_i(r_1)\psi_j(r_2) \right\rangle = (ii, jj) \quad (1.12)$$

$$K_{ij} = \left\langle \psi_i(r_1)\psi_j(r_2) \left| \frac{1}{r_{12}} \right| \psi_i(r_2)\psi_j(r_1) \right\rangle = (ij, ij) \quad (1.13)$$

Minimising the electronic energy, as given in equation (1.10) with respect to ψ_i , leads to the Hartree-Fock equations and the determination of the orbital energies ϵ_i :

$$\hat{F}\psi_i = \epsilon_i\psi_i \quad (1.14)$$

$$\epsilon_i = H_{ii}^{core} + \sum_j (2J_{ij} - K_{ij}) \quad (1.15)$$

where \hat{F} is the Fock operator. It has a very complicated form in general and, hence, is used mostly for atomic calculations only.

1.3 Roothaan SCF-LCAO-MO Method

Roothaan [27] showed that instead of solving the Hartree-Fock equations numerically, one can put them in matrix form by expansion into a basis of atomic orbital functions and then utilise the standard matrix techniques to solve the equations. The basic idea involved in the method is:

1. the many-electron wavefunction is described as a Slater determinant of one-electron wave functions (1.8),
2. the interelectronic interactions are considered as an average electrostatic field, and
3. equation (1.4) is solved in an one-dimensional space which is formed from a given basis set of atomic orbitals (LCAO-approximation).

The unknown molecular orbitals ψ_i are expanded in terms of a set of K known basis functions $\{\phi_\mu(r)|\mu = 1, 2, \dots, K\}$ in the linear expansion

$$\psi_i = \sum_{\mu=1}^K c_{\mu i} \phi_\mu, \quad i = 1, 2, \dots, K \quad (1.16)$$

A complete set $\{\phi_\mu\}$ would lead to an exact expansion and any such basis could be used. But in practice one is restricted to using a finite set of functions and, hence, it is important to choose the basis functions in such a manner that they provide the best possible expansion for the exact molecular orbitals (MOs) $\{\psi_i\}$. The indices i, j, k, ℓ, \dots correspond to the molecular orbitals (MOs), and indices $\mu, \nu, \lambda, \sigma, \dots$ correspond to the atomic orbitals (AOs).

Substitution of (1.16) in (1.11)-(1.13) leads to (for closed shells):

$$H_{ij}^{core} = \sum_{\mu} \sum_{\nu} c_{\mu i} c_{\nu j} H_{\mu\nu}^{core} \quad (1.17)$$

$$(ij, k\ell) = \sum_{\mu} \sum_{\nu} \sum_{\lambda} \sum_{\sigma} c_{\mu i} c_{\nu j} c_{\lambda k} c_{\sigma \ell} (\mu\nu, \lambda\sigma) \quad (1.18)$$

$$H_{\mu\nu}^{core} = \left\langle \phi_\mu \left| -\frac{\hbar^2}{2m} \Delta_1 - \sum_A \frac{Z_A}{r_{1A}} \right| \phi_\nu \right\rangle \quad (1.19)$$

$$(\mu\nu, \lambda\sigma) = \left\langle \phi_\mu(1)\phi_\nu(1) \left| \frac{1}{r_{12}} \right| \phi_\lambda(2)\phi_\sigma(2) \right\rangle \quad (1.20)$$

$$E_{el} = \sum_{\mu} \sum_{\nu} P_{\mu\nu} H_{\mu\nu}^{core} + \frac{1}{2} \sum_{\mu} \sum_{\nu} \sum_{\lambda} \sum_{\sigma} P_{\mu\nu} P_{\lambda\sigma} \left[(\mu\nu, \lambda\sigma) - \frac{1}{2}(\mu\lambda, \nu\sigma) \right] \quad (1.21)$$

$$P_{\mu\nu} = 2 \sum_i^{occupied} c_{\mu i} c_{\nu i} \quad (1.22)$$

In the expression for energy (1.21), the $H_{\mu\nu}^{core}$, $(\mu\nu, \lambda\sigma)$ and $(\mu\lambda, \nu\sigma)$ integrals have a constant value for a given basis of atomic orbitals (AOs) ϕ . The electronic energy E_{el} is thus only dependent on the density matrix elements $P_{\mu\nu}$ and, hence, on the LCAO-coefficients $c_{\mu i}$ (1.22).

Using the variation theorem to minimise the energy E_{el} with respect to the coefficients $c_{\mu i}$ the Roothaan equations are obtained [27]:

$$\sum_{\nu} F_{\mu\nu} C_{\nu i} = \epsilon_i \sum_{\nu} S_{\mu\nu} C_{\nu i}, \quad i = 1, 2, \dots, K \quad (1.23)$$

The Fock matrix elements $F_{\mu\nu}$ are defined as follows:

$$F_{\mu\nu} = H_{\mu\nu}^{core} + \sum_{\lambda} \sum_{\sigma} P_{\lambda\sigma} \left[(\mu\nu, \lambda\sigma) - \frac{1}{2}(\mu\lambda, \nu\sigma) \right] \quad (1.24)$$

and the overlap integrals $S_{\mu\nu}$ are defined as:

$$S_{\mu\nu} = \langle \phi_\mu | \phi_\nu \rangle \quad (1.25)$$

The equations above are valid for closed-shell systems, but modified sets for various combinations of open shells are also known.

At the completion of the SCF calculations, one has K orbitals ψ_i (which depend on the coefficients $c_{\mu i}$ (1.16)), with the lowest n orbitals doubly occupied and the rest of the orbitals unoccupied. The SCF calculations also provide K orbital energies ϵ_i and the electronic energy E_{el} .

1.4 Configuration Interaction

The SCF method ignores the instantaneous part of the electron-electron interaction (*electron correlation*). Correlation energies and correlation effects are required for improvement of the corresponding SCF results. Mathematically this can be done by configuration mixing, which simply means allowing the wave functions to be a linear combination of electronic structures (configurations).

The configuration interaction (CI) method is an attempt to determine the correlation energies and correlation effects. The basic idea involved in the CI method is the diagonalization of the N -electron Hamiltonian in a basis of N -electron functions (Slater determinants). In other words, it involves a representation of the exact wave function as a linear combination of N -electron trial functions followed by application of the linear variational method. Though theoretically the CI method can yield the exact solution of a many-electron problem, restrictions are imposed due to enormous determinants involved in the calculation process even for small molecules.

1.5 MRD-CI Method

These restrictions lead to development of various truncated CI methods. The Multi-Reference-Double-Excitation-Configuration-Interaction (MRD-CI) method developed by Buenker and Peyerimhoff [28] is found to yield very good results in practice and the results obtained for the systems discussed in the following chapters confirm this. The MRD-CI method includes single and double excitations relative not only to the Hartree-Fock wave function but also relative to other important configurations (which may themselves be doubly excited with respect to the HF wavefunction). Thus, the method effectively takes into account higher than double excitations from the HF wave function.

The MRD-CI method has the following algorithm:

1. All the singly and doubly excited (with respect to the main or leading configurations) symmetry adapted functions (SAFs) are generated.
2. The CI-secular matrix generated on the basis of the main configuration is diagonalised.
3. Since the size of such matrices is of the order of $10^5 - 10^7$ a selection is made for each configuration generated, based on the energy lowering caused by each configuration with respect to the lowest-lying root of the CI matrix.
4. The final CI-secular matrix includes only those SAFs which cause an energy lowering greater than a given threshold energy T .
5. The contribution of the unselected SAFs is taken into account by employing an energy extrapolation technique. A correction is also made for triple or higher excitations with respect to the main configuration.

The molecular orbitals (MOs) resulting from the SCF calculations are used for

constructing determinantal trial functions employed in the ensuing CI calculations.

Each configuration is described separately from the others in the restricted Hartree-Fock (RHF) method. In order to account for the correlation effects, the configuration interaction (CI) method describes the electronic states for a many-electron system as a linear combination of determinants $\Psi = \sum_i \Phi_i$, where Φ_i are determinants that result from single- and double-excitations of the HF ground state configuration. The electronic-state wave functions are then determined by variational calculations in the linear space of the excited determinants. If one considers all the resulting excitations from the ground state configuration, then it is a Full-CI (FCI) calculation. A FCI calculation leads to very large eigenvalue problems even for very small molecules. Hence, it is necessary to select only those excitations that are really important. The Multi-Reference-Double-Excitation-Configuration-Interaction (MRD-CI) method uses the following strategies to choose the important excitations:

1. Use of orthogonal single-determinant state functions causes all configuration interactions between states that differ by more than two excitations to disappear. Thus, in the following direct CI one can limit oneself to only single and double excitations.
2. In order to take into consideration the interaction of higher excited determinants with the ground state configuration, those single- and double- excitations that interact most strongly with the ground state or excited state of interest are put together in a so called "reference space". From this reference space the final configuration space is determined once again through single- and double- excitations (substitutions). All these excitations which are generated need not be taken into the

configuration space, however. Instead all the generated excitations are tested to determine the lowering in energy caused by them relative to the reference space. Those excitations that cause an energy lowering greater than a certain limit T are included in the final CI-space.

3. A correction term is used to consider those excitations that have been ignored. The correction formula

$$E_{T=0} = E_T + \lambda \sum_{i=1}^n \Delta E_i$$

helps in estimating that energy contribution due to the excitations ignored because the energy lowering ΔE_i caused by them was less than T (λ is a linear extrapolation parameter). The so called Davidson-Correction [29]

$$\Delta E_{Davidson} = \left(1 - \sum_{i=1}^n c_i^2 \right) (E_{Ref} - E_{T=0})$$

helps estimate the energy contribution due to excitations not considered in the FCI-method (originating just from a single reference configuration). The c_i 's are the expansion coefficients of the reference configurations and $(E_{Ref} - E_{T=0})$ is the energy difference for a given root between that for reference space and the corresponding extrapolated energy.

A word about the choice of basis sets used in the calculations discussed in the following chapters also should be given. There are two types of basis functions commonly employed in quantum chemistry calculations, namely exponential-type functions and Gaussian-type functions. The exponential-type functions have the form

$$N_n r^{n-1} \exp(-\zeta r) Y_{\ell m} \quad (1.26)$$

where N_n is a radial normalization factor and $Y_{\ell m}$ is a (normalized) spherical harmonic. These functions provide a realistic representation of the wave function in the region of space close to the nucleus upon which they are centered as well as in the long-range region. They are not preferred, however, because accurate evaluation of integrals over such functions is quite difficult in the multicenter case.

The most widely used basis functions are the Gaussian-type functions. They have the form

$$N_n r^{n-1} \exp(-\zeta r^2) Y_{\ell m} \quad (1.27)$$

where N_n is again a normalization constant and $Y_{\ell m}$ is a spherical harmonic. The integrals over Gaussian-type basis functions are easily evaluated because of the Gaussian product theorem which states that the product of two Gaussians on different centres is itself a Gaussian with a center somewhere on the line joining these centres [30].

1.6 Pseudopotential Theory

The starting point for the pseudopotential theory is the assumption that the nature of the bond is mostly determined by the valence electrons involved in its formation. This allows for the assumption that the electrons close to the nuclei can be considered

as having a constant potential (frozen-core), so that in the quantum mechanical calculations only the valence electrons are treated explicitly. In order to construct these “frozen-core” potentials, one has to take into consideration the effect of such a core on the valence electrons. The first effect is the electrostatic repulsion that each electron has for the other electrons present. The second effect is due to the Pauli principle, which states that no two electrons can exist in the absolutely identical quantum mechanical states. The Pauli principle is satisfied in that only those wave functions are allowed for the valence electrons that are orthogonal to those of the core electrons.

1.7 Pseudopotentials in Molecular Calculations

The concept of a frozen core leads to division of the electrons in a molecule into two types. One type is that comprising the valence electrons of all the atoms involved, and the second group is that comprised of the core electrons. The valence electrons can be treated by the usual electronic calculations. The core electrons allow for the following approximations:

1. The core electron charge distribution of different atoms do not overlap with each other. This results in elimination of exchange integrals between their state functions on various nuclei.
2. The Coulomb-interaction between core electrons of different nuclei can be considered as point potentials concentrated only on the corresponding atoms.

$$\int \frac{\psi_a(\tau_1)^* \psi_a(\tau_1) \psi_b(\tau_2)^* \psi_b(\tau_2)}{(r_1 - r_2)} d\tau_1 d\tau_2 = \frac{e_1 e_2}{|R_A - R_B|} = \frac{1}{|R_A - R_B|}$$

The effect of the core electrons on the nucleus-nucleus interaction is therefore that of a shielding effect,

$$\frac{Z_A Z_B}{R_{AB}} \rightarrow \frac{(Z_A - N_A)(Z_B - N_B)}{R_{AB}}.$$

Using these assumptions, the Hamilton operator for a molecule consisting of M atoms with N valence electrons and $\sum_{A=1}^M N_A$ core electrons can be written as:

$$\begin{aligned} \hat{H} = & - \sum_{i=1}^N \frac{1}{2} \nabla_i^2 - \sum_{i=1}^N \sum_{A=1}^M \frac{Z_A}{r - R_A} + \sum_{A=1}^M \hat{U}_A \\ & + \sum_{i>j}^N \frac{1}{r_{ij}} + \sum_{A=1}^M \hat{H}_A + \sum_{A<B} \frac{(Z_A - N_A)(Z_B - N_B)}{R_{AB}} \end{aligned} \quad (1.28)$$

This is the usual HF-Hamiltonian with additional terms:

1. $\sum_{A=1}^M \hat{U}_A$

where

$$\begin{aligned} \hat{U}_A = & U_{L_A+1}(r - R_A) \\ & + \sum_{\ell=0}^L \sum_{m=-\ell}^{\ell} |\ell_A m_A\rangle (U_{\ell_A}(r - R_A) - U_{L_A+1}(r - R_A)) \langle \ell_A m_A| \end{aligned} \quad (1.29)$$

L is generally taken to be one greater than the largest ℓ quantum number among the core electrons. The operator \hat{U}_A is the sum over all the projections of the pseudopotentials of the core electrons of all the M atoms.

2. $\sum_{A=1}^M \hat{H}_A$

where

$$\hat{H}_A = - \sum_{i=1}^{N_A} \frac{1}{2} \nabla_i^2 - \sum_{i=1}^{N_A} \frac{Z_A}{r_i - R_B} + \sum_{i>j}^{N_A} \frac{1}{r_{ij}}$$

This is the sum over all the constant HF-energies of the core electrons of all the nuclei.

$$3. \sum_{A<B} \frac{(Z_A - N_A)(Z_B - N_B)}{R_{AB}}$$

is the sum over the shielding effect of the core electrons on the nuclei. It is a measure of the lowered nucleus-nucleus repulsion.

The additional terms 2 and 3 contribute a constant value to the Hamilton operator. The term 1 leads to additional one-electron integrals. The pseudopotentials $U_{\ell_A}(r - R_A)$ are a sum over radial Gaussian functions. Hence, for the basis functions ψ_A and ψ_B the following new integrals are obtained:

$$\chi_{AB} = \int_{-\infty}^{\infty} \psi_A(\tau)(r - R_C)^{n-2} \exp(-\eta(r - R_C)^2) \psi_B(\tau) d\tau \quad (1.30)$$

and

$$\begin{aligned} \gamma_{AB}^{\ell} &= \sum_{m=-\ell}^{\ell} \int_0^{\infty} (r - R_C)^n \exp(-\eta(r - R_C)^2) \int_0^{2\pi} \int_0^{\pi} \psi_A(\theta_C, \varphi_C) Y_{\ell m}(\theta, \varphi) d\theta d\varphi d\tau \\ &\times \int_0^{2\pi} \int_0^{\pi} \psi_B(\theta_C, \varphi_C) Y_{\ell m}(\theta, \varphi) d\theta d\varphi. \end{aligned} \quad (1.31)$$

The basis functions are localised on nucleus A and nucleus B, respectively. The algorithm for the explicit calculations of integrals (in the case that ψ_A and ψ_B are Cartesian Gaussian functions) can be found in reference [31].

1.8 Relativistic Effects

The following reasons can be given for considering relativistic effects in quantum chemistry:

1. The velocities of the electrons close to the nucleus lie in the range $\approx \frac{Z}{137}c$ (SI units), and therefore we can expect that relativistic effects are quite important in the chemical behaviour of heavy atoms.
2. The relativistic treatment of electrons allows that the electron spin can be accounted for without assuming the Pauli approximation. It also provides for a qualitatively better description of electron properties such as spin, shape of the orbitals, and existence of states with negative energies (Positrons).

The most important effects on the chemical properties are:

1. Due to the dependence of relativistic mass on velocity, the mass of the electrons close to the nucleus increases. This leads to orbital contraction and stabilisation of s - and p - orbitals.
2. An indirect effect of the s - and p - orbital contraction is the increased shielding which leads to expansion and destabilisation of d - and f - orbitals.
3. The relativistic treatment of an electron in a hydrogen atom type system leads directly to a coupling term between spin and orbital angular momentum. This spin-orbit splitting is $\propto Z^4$ and leads, especially in the case of heavy atoms, to destabilisation of all orbitals with $\ell > 0$.

1.9 Spectroscopic Properties using the CI Wave Functions

In order to calculate the spectroscopic properties of a molecule it is necessary to solve the Schrödinger equation for the nuclei. The nuclear Schrödinger equation can be written as follows for a diatomic molecule:

$$-\frac{1}{2\mu} \frac{\partial^2}{\partial R^2} R\Psi(Q) + \frac{1}{2\mu R^2} \hat{J}^2 \Psi(Q) + V(R)\Psi(Q) = E\Psi(Q) \quad (1.32)$$

where $Q(R, \varphi, \theta)$ are the internal coordinates of the nuclei, and the square of the angular momentum operator (\hat{J}^2) is:

$$\hat{J}^2 = - \left(\frac{1}{\sin^2\theta} \frac{\partial^2}{\partial \varphi^2} + \frac{1}{\sin\theta} \frac{\partial}{\partial \theta} \sin\theta \frac{\partial}{\partial \theta} \right) \quad (1.33)$$

In the above equations, μ is the reduced mass, $V(R)$ is the potential energy of the electrons (obtained from the MRD-CI calculations), $\Psi(Q)$ is the vibrational wave function, and E is the corresponding energy eigenvalue.

Equation (1.32) is a simple second order differential equation which may be solved using the Numerov-Cooley methods [32,33] for a given analytical potential function. The vibrational levels which are the eigenvalue of eq. (1.32) can be written as:

$$E_v = T_e + \omega_e \left(v + \frac{1}{2}\right) - \omega_e x_e \left(v + \frac{1}{2}\right)^2 + \dots + E_J, \quad (1.34)$$

and the rotational levels can be written as:

$$E_J = B_v[J(J+1)] - D_v[J(J+1)]^2. \quad (1.35)$$

The energy difference of two neighbouring vibrational levels is:

$$E_{v+1} - E_v = \omega_e - 2(v+1)\omega_e x_e, \quad (1.36)$$

and that between two neighbouring rotational levels is:

$$E_{J+1} - E_J = 2(J+1)B_v - 4(J+1)^3 D_v. \quad (1.37)$$

One can determine the vibrational frequency ω_e , the anharmonicity constant $\omega_e x_e$, and the rotational constant B_v with the help of the above equations.

The lifetime (τ_n) of a non-degenerate electronic state is inversely proportional to the Einstein coefficient for spontaneous emission. Thus, for a transition $n \rightarrow m$:

$$\tau_n = \sum_{E_m < E_n} \frac{1}{A_{nm}} \quad (1.38)$$

The Einstein coefficient mentioned above relates to the transition moment according to the following equation:

$$A_{nm} = 2.026 \times 10^{-6} \Delta \bar{E}_{nm}^3 |\langle \Psi_n | \vec{r} | \Psi_m \rangle|^2 \quad (1.39)$$

According to the Born-Oppenheimer approximation the complete wave function can be written as a product of the electronic and nuclear wavefunction

$$\Phi(R, q) = \Psi(R)\psi(q). \quad (1.40)$$

This helps in establishing following relationship between the Einstein coefficient and the electronic transition moment $\mu_{nm}^{elc} = \langle \psi_n(q) | \vec{r} | \psi_m(q) \rangle_R$:

$$A_{nm} = 2.026 \times 10^{-6} \Delta \bar{E}_{nm}^3 \left| \langle \Psi_n(R) | \mu_{nm}^{elc}(R) | \Psi_m(R) \rangle \right|^2, \quad (1.41)$$

where $\Delta \bar{E}$ is in the units of cm^{-1} and μ is in the units of ea_0 [15]. The $n \times m$ integrals

$$\langle \Psi_n(R) | \mu_{nm}^{elc}(R) | \Psi_m(R) \rangle$$

can be determined numerically.

Chapter 2

Tellurium Fluoride (TeF)

The theoretical methods described in Chapter 1 have been used extensively to study the electronic states and transitions of the lightest tellurium monohalide, namely, tellurium fluoride (TeF). Details of the calculations, results obtained and their comparison with available experimental data, as well as predictions and conclusions derived therefrom are presented in the present Chapter.

2.1 Details of the Theoretical Treatment

The 16-electron core potential as reported by La John et. al [34] has been employed to describe the inner shells of the Te atom. The original ($3s3p4d$) atomic orbital (AO) basis set given in ref. [34] was used to treat explicitly the $4d$, $5s$, and $5p$ valence electrons with the ($4d$)/[$1d$] contraction applied. It was further augmented by one d and two f polarization functions with optimized exponents of 0.46, 3.4 and $1.1 a_0^{-2}$, respectively. Two diffuse exponents, s ($0.021 a_0^{-2}$) and p ($0.016 a_0^{-2}$) were also added, resulting in a ($4s4p5d2f$)/[$4s4p2d2f$] basis set for the Te atom. A core-potential was used to describe the $1s$ electrons of the fluorine atom [35]. The AO basis of ($4s4p$) type from ref.

[35] was used in uncontracted form and was augmented by single d and f polarization functions with optimized Gaussian exponents of 0.7 and $1.5 a_0^{-2}$, respectively.

The starting point for the present studies, SCF calculations, were performed for the neutral molecule in its first excited state $^4\Sigma^- (\sigma^2\pi^4\pi^{*2}\sigma^*)$, for the ground state $^2\Pi (\sigma^2\pi^4\pi^{*3})$, and for the corresponding cation in the $^3\Sigma^- (\sigma^2\pi^4\pi^{*2})$ state. The latter two electronic configurations result in the breaking of the $p_{x,y}$ symmetry and thus creating some SCF convergence problems for certain internuclear distances. However, such problems did not exist for the $^4\Sigma^-$ SCF and therefore, these MO's were conveniently chosen for final investigations.

The SCF calculations provide the symmetry adapted molecular orbitals for the construction of configurations to be used in the CI calculations. Details of the MRD-CI treatment of TeF, without the spin-orbit (SO) interaction, are given in Table 2.1 for the equilibrium bond length of $3.65 a_0$ for the ground state. The calculations were performed in formal C_{2v} symmetry, but the one-electron basis, which is employed to construct the various configurations, transforms according to the irreducible representations of the linear $C_{\infty v}$ point group. The configuration selection threshold was selected at $T = 2.0 \times 10^{-6} E_h$. Typically 6 – 8 roots of each C_{2v} irreducible representation are obtained for the doublet states. For the quartet states a lesser number of roots, 2 – 5, were calculated. The number of roots calculated are more than actually required. This was done to ensure as complete a description of the states of interest as possible. The leading electronic configurations for the lowest roots of each symmetry are also listed in Table 2.1 in terms of the linear MO notation. The generated configuration spaces are of the order $(12 - 13) \times 10^6$ symmetry adapted functions (SAFs) and result from 110 – 170 reference configurations. At the selection threshold chosen, the number of SAFs included in the final secular equations falls uniformly in the range of 50 000 – 60 000. For

the 4A_1 symmetry somewhat smaller numbers are obtained, but only two states have been treated in this irreducible representation and they are satisfactorily described.

A standard perturbative procedure [28], has been used to estimate the total CI energy eigenvalues at the unselected ($T = 0$) level of treatment. In addition, the multireference Davidson correction [29,36] is used to estimate the energy of each state at the full CI level of treatment, i.e., by taking into account the effects of higher than double excitations with respect to the reference configurations. The $\sum c_i^2$ ¹ values for the reference configurations (Table 2.1) are seen to fall in the range of 0.92–0.94. Such high values are achieved due to the fact that the tellurium $4d$ -type MOs are treated as a frozen core in the CI treatment and only 13 electrons are available for the excitation process. The present theoretical work aims at providing the best possible description of the low-lying states of the TeF radical and hence placing the tellurium $4d$ -electrons in the CI core was considered acceptable. A series of calculations were carried out for the internuclear distance range of 3.0–10.0 a_0 , with varying increments of 0.05–0.25 a_0 , depending on the region of interest.

The variational wave functions themselves are used to compute properties such as electric dipole and also radiative lifetimes. These functions are also employed in the second step of the LSC-SO-CI procedure [37] to form a matrix representation of the full relativistic Hamiltonian including SO-coupling. Since TeF has an odd number of electrons, each spatial symmetry contributes to the spin-mixed wave functions (Ω -states). There are two degenerate sets [38], with one M_s function included for each doublet and two for each quartet $\Lambda - S$ eigenfunction. Both sets of degenerate functions are required to obtain quantities such as the perpendicular (x, y) transition moments. All Ω values (1/2, 3/2, 5/2, and 7/2) result from each of the secular problems and thus

¹ $\sum c_i^2$ is the total contribution of the reference configurations in the final wave function.

Table 2.1: Technical details of the MRD-CI calculations of TeF.^a

C_{2v}	N_{ref}/N_{root}	SAFTOT/SAFSEL	$C_{\infty v}$	Leading conf.	Σc_i^2
${}^2B_{1,2}$	164/8	13969769/61565	$1^2\Pi$	$\sigma^2\pi^4\pi^*3$	0.940
			$2^2\Pi$	$\sigma^2\pi^4\pi^*\sigma^{*2}$	0.934
			$3^2\Pi$	$\sigma^2\pi^3\pi^*4$	0.920
			$4^2\Pi$	$\sigma^2\pi^4\pi^*2\pi^{**}$	0.929
			$1^2\Phi$	$\sigma^2\pi^4\pi^*2\pi^{**}$	0.929
			$5^2\Pi$	$\sigma^2\pi^4\pi^*2\pi^{**}$	0.929
2A_1	174/8	12726534/48992	$1^2\Delta$	$\sigma^2\pi^4\pi^*2\sigma^*$	0.940
			$1^2\Sigma^+$	$\sigma^2\pi^4\pi^*2\sigma^*$	0.943
			$2^2\Sigma^+$	$\sigma\pi^4\pi^*4$	0.934
			$2^2\Delta$	$\sigma^2\pi^4\pi^*2\sigma^{**}$	0.939
			$3^2\Sigma^+$	$\sigma^2\pi^4\pi^*2\sigma^{**}$	0.929
2A_2	129/6	13553228/56831	$1^2\Sigma^-$	$\sigma^2\pi^4\pi^*2\sigma^*$	0.939
			$1^2\Delta$	$\sigma^2\pi^4\pi^*2\sigma^*$	0.941
			$2^2\Sigma^-$	$\sigma^2\pi^4\pi^*2\sigma^{**}$	0.939
			$2^2\Delta$	$\sigma^2\pi^4\pi^*2\sigma^{**}$	0.939
			$3^2\Sigma^-$	$\sigma^2\pi^4\pi^*2\sigma^{***}$	0.936
${}^4B_{1,2}$	131/4	12682493/50972	$1^4\Pi$	$\sigma^2\pi^4\pi^*2\pi^{**}$	0.928
4A_1	73/2	7374825/15966	$2^4\Pi$	$\sigma\pi^4\pi^*3\sigma^*$	0.922
			$1^4\Delta$	$\sigma^2\pi^3\pi^*3\sigma^*$	0.918
4A_2	110/5	13129232/53304	$1^4\Sigma^+$	$\sigma^2\pi^3\pi^*3\sigma^*$	0.918
			$1^4\Sigma^-$	$\sigma^2\pi^4\pi^*2\sigma^*$	0.940
			$2^4\Sigma^-$	$\sigma^2\pi^4\pi^*2\sigma^{**}$	0.928
			$3^4\Sigma^-$	$\sigma^2\pi^4\pi^*2\sigma^{***}$	0.928
			$1^4\Delta$	$\sigma^2\pi^3\pi^*3\sigma^*$	0.924

^a The number of selected SAFs and the Σc_i^2 values over reference configurations are given for $r = 3.65 a_0$. SAFTOT designates the total number of generated, SAFSEL the number of selected SAFs, N_{ref} and N_{root} refer to the number of reference configurations and roots treated, respectively.

it is necessary to examine the coefficients of the eigenvectors to assign them to definite symmetries. This procedure has the disadvantage of delivering eigenfunctions of mixed symmetry. However, in the present study this was not a major problem as the attention was focused mainly on the low-lying states which are seen to be energetically well separated except near the dissociation limit.

The final spin-mixed functions are then combined with the $\Lambda - S$ transition moments to obtain the corresponding Ω -state electronic transition moments at each r value. The Numerov-Cooley numerical integration procedure [32,33] was employed to solve the nuclear Schrödinger equations in order to obtain the corresponding vibrational energies and wave functions.

2.2 Potential Curves

Fig. 2.1 shows the computed potential curves for all the 23 $\Lambda - S$ states corresponding to the three lowest dissociation limits, namely $\text{Te}(^3P)+\text{F}(^2P^o)$, $\text{Te}(^1D)+\text{F}(^2P^o)$, and $\text{Te}(^1S)+\text{F}(^2P^o)$. The symmetry of the ground state was found to be $^2\Pi(\sigma^2\pi^4\pi^{*3})$ as predicted experimentally. The first excited state is the $A^4\Sigma^-$ state generated from the $\pi^* \rightarrow \sigma^*$ electronic transition. The electronic configuration of this state is $\sigma^2\pi^4\pi^{*2}\sigma^*$. This result is analogous to the case of oxygen monohalides [39-51] and does not agree with the suggested experimental assignment as $^2\Pi$ [7]. The cause for the misassignment by experimentalists could be that in OX radicals the observed transition is a $2^2\Pi \leftarrow X^2\Pi$ transition, the first excited state $^4\Sigma^-$ being repulsive. Moreover, both $^2\Pi$ and $^4\Sigma^-$ undergo SO interactions to produce 1/2 and 3/2 Ω states, which could also have been the cause for confusion. The σ^* MO, occupied in the $A^4\Sigma^-$ state, is localized mostly on the Te-atom in the FC region of the ground state and thus is only weakly

antibonding, in sharp contrast to what is found in the case of IO [14], for which the electronegativity difference between the constituent atoms is much less. The equilibrium bond length of $A^4\Sigma^-$ is slightly larger than that of the ground state. This increase is only about half as great in TeF as in IO [14]. The $2^2\Pi$ excited state actually has a smaller r_e value than $X^2\Pi$ (Fig. 2.1), but it corresponds to a Rydberg $\pi^* \rightarrow 6p\pi$ state near its potential minimum and lies about $6.5 eV$ higher in energy than the $X^2\Pi$. Its potential curve is cut by several other $^2\Pi$ states near this minimum. Hence, experimental observation of this state should be difficult. Besides the $2^2\Pi$ mentioned above, the $2^4\Sigma^-$ and $2^2\Sigma^-$ states also have a potential minimum at $\approx 3.5 a_0$ and correspond to Rydberg states. The $2^4\Sigma^-$ occupies the Rydberg $5s$ orbital and thus has a similar potential curve to the of $X^3\Sigma^-$ for TeF^+ . They do not dissociate directly to the first dissociation limit and their potential curves are eventually crossed by repulsive states of similar symmetry.

The second excited state is computed to be a $^2\Sigma^-$. It is generated by the same electronic transition ($\pi^* \rightarrow \sigma^*$) as the $A^4\Sigma^-$ state. The $B^2\Sigma^-$ state is even more weakly bound because it dissociates to the first atomic limit (Fig. 2.1). The $^2\Delta$ state generated by the same electronic transition mentioned above, referred to as the $C^2\Delta$ state, lies above the B state. The corresponding $^2\Sigma^+$ lies slightly above the $\text{Te}(^3P)$ asymptote. All other quartet states that go on to this limit are computed to have repulsive potentials. These include two $^4\Pi$, a $^4\Delta$, and a $^4\Sigma^+$ as well as the $2^4\Sigma^-$ state mentioned above.

The $23 \Lambda - S$ states dissociating to the first three atomic limits (Fig. 2.1) undergo SO-coupling to generate a total of 45 Ω states. Calculations have been performed for the first 27 Ω states dissociating to the first limit, namely, $\text{Te}(^3P)+\text{F}(^2P^o)$. Fig. 2.2 shows the computed potential curves converging to the first limit of $\text{Te}(^3P_2)+\text{F}(^2P_{3/2}^o)$. In the present study we will concentrate on the lowest five states which have been studied

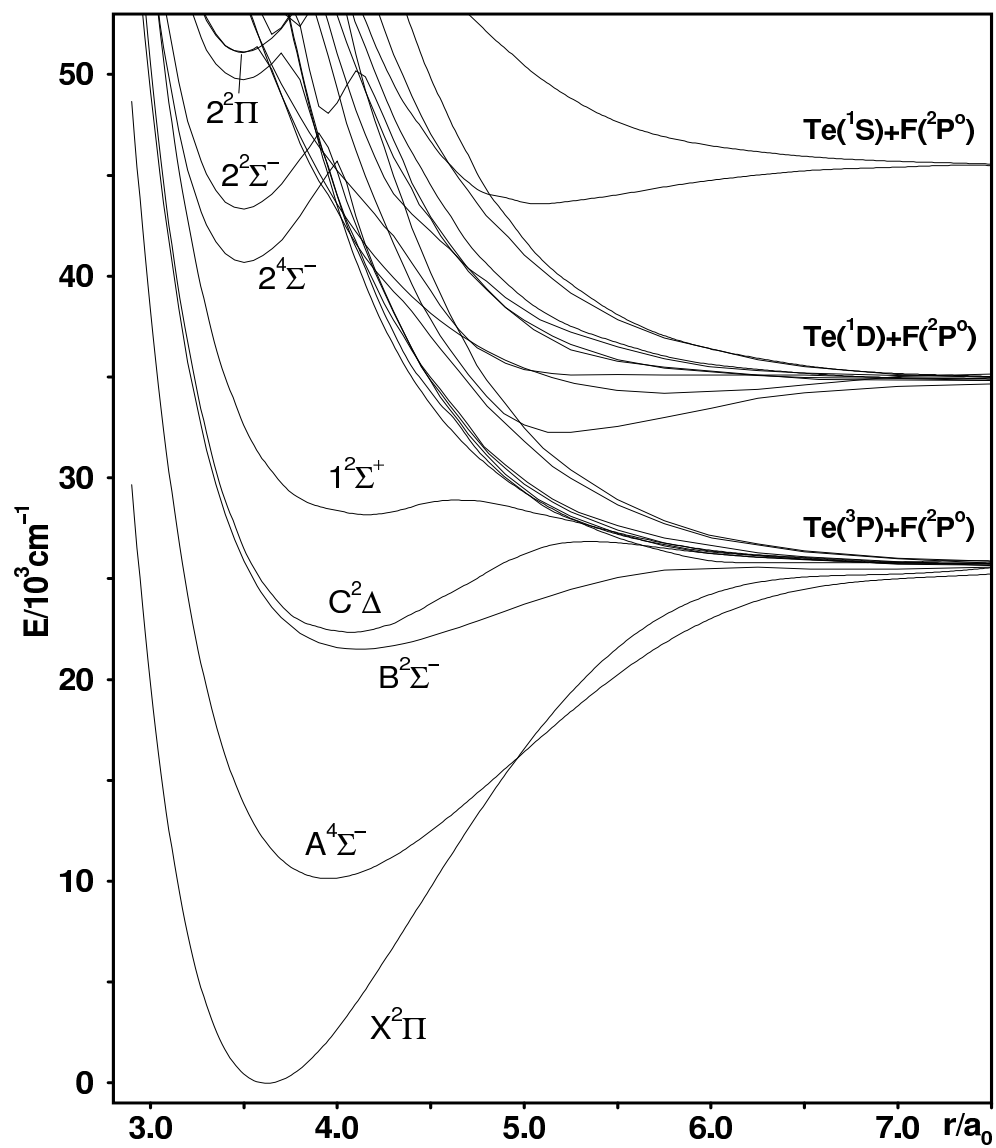


Figure 2.1: Computed potential energy curves for the low-lying $\Lambda - S$ states of TeF obtained without inclusion of spin-orbit interaction.

Table 2.2: Calculated (this work) and experimental spectroscopic properties of ^{130}TeF (transition energy T_e , bond length r_e , and vibrational frequency ω_e).

State	T_e/cm^{-1}		$r_e/\text{\AA}$		ω_e/cm^{-1}	
	calc.	exp.	calc.	exp.	calc.	exp.
$X_1^2\Pi_{3/2}$	0	0	1.929	1.90675 [12]	605	616.3 [12]
$X_2^2\Pi_{1/2}$	4382	4183 [11]	1.924	1.90155 [12]	612	624.3 [12]
$A_1^4\Sigma_{1/2}^-$	12164	13262 [12]	2.094	2.08876 [12] ^a	428	432.0 [12]
$A_2^4\Sigma_{3/2}^-$	13054	14160 [12]	2.087	2.07870 [12]	434	435.8 [12]
$B^2\Sigma_{1/2}^-$	23189	21579 [12]	2.178	-	321	384.5 [12]
$C_1^2\Delta_{5/2}$	24816	22992 [52]	2.167	-	342	403 [52]
$C_2^2\Delta_{3/2}$	24964	23036 [52]	2.127	-	378	408 [52]

^a An r_0 value.

experimentally [7,8,10-12]. The computed dissociation energy is 25480 cm^{-1} (3.16 eV), as compared to 25740 cm^{-1} at the $\Lambda - S$ level, and corresponds to the results obtained for calculations at an internuclear distance of $10.0 a_0$. The corresponding LSC-SO-CI value for IO at a similar level of treatment is 9500 cm^{-1} [14] lower. This is consistent with the fact that the π^* MO is less antibonding in TeF, being mostly concentrated on the Te atom, and the molecular bonding is notably more ionic in this case. There is, however, no experimental result available for comparison. A few states converging to the second limit $\text{Te}(^3P_2)+\text{F}(^2P_{1/2}^o)$ are also included in Fig. 2.2. Most of the 27 Ω states calculated are repulsive and have not been included in Fig. 2.2. The computed spectroscopic constants, along with the available experimental data are listed in Table 2.2.

The $X^2\Pi$ ground state splits as a result of SO coupling into 1/2 and 3/2 Ω states,

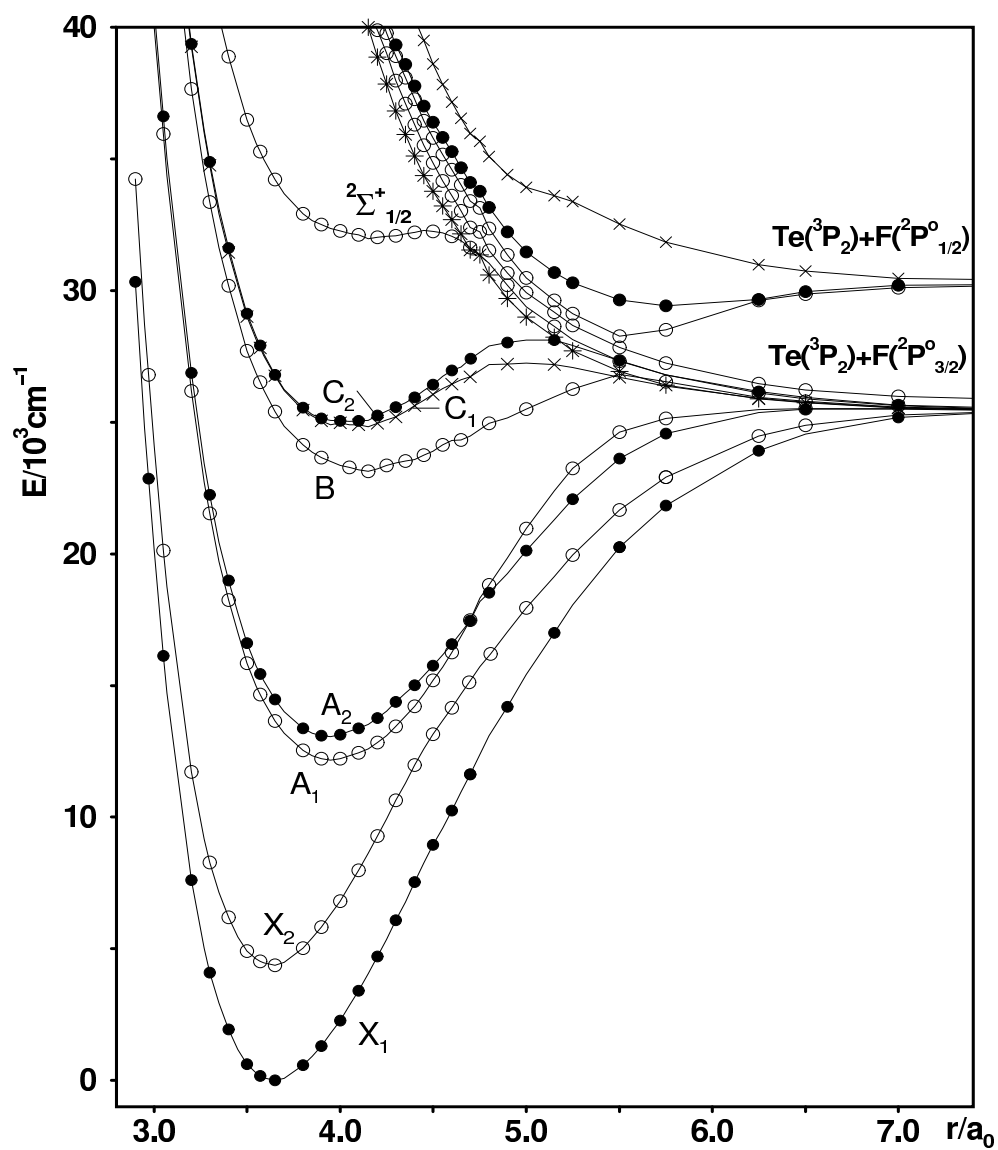


Figure 2.2: Computed potential energy curves for the low-lying Ω states of TeF: \circ - $\Omega = 1/2$ states; \bullet - $\Omega = 3/2$ states; \times - $\Omega = 5/2$ states; and $*$ - $\Omega = 7/2$ state.

with the 3/2 component lying lower in energy. The r_e value of the $X_1^2\Pi_{3/2}$ ground state is overestimated by $\approx 0.02\text{\AA}$ at the present level of treatment. The computed ω_e frequency is 11 cm^{-1} ($\approx 2\%$) too small (Table 2.2), consistent with the bond length result. The computed SO splitting is 4382 cm^{-1} and is about 199 cm^{-1} higher than the experimentally measured value [12]. The overestimation of this quantity is in agreement with the fact that the π^* open-shell MO has predominantly tellurium character. This is to be expected from the fact that the fluorine atom is much more electronegative. The IO ground state splitting is considerably lower (2091 cm^{-1}), even though the corresponding spin-orbit matrix element for the heavy atom in this molecule, iodine, is notably larger than that for tellurium, 2534 vs 2136 cm^{-1} . This is again a clear indication of the composition of the π^* MO in IO, specifically that it has a fairly large amount of oxygen character because of the much smaller electronegativity difference in this system as compared to TeF. The r_e value of the $X_2^2\Pi_{1/2}$ state is 0.0055\AA shorter than that of the $X_1^2\Pi_{3/2}$. This shortening of bond length is in almost perfect agreement with that observed experimentally.

The first excited state, $^4\Sigma^-$, shows a much smaller SO splitting. The $\Omega = 1/2$ component is lower in energy than the corresponding 3/2 component, despite the fact that it is repelled more by the $X_2^2\Pi_{1/2}$ component than the other by X_1 . This can be explained by the presence of the $B^2\Sigma^-$ state, which lies only 7000 cm^{-1} above the $A^4\Sigma^-$ and counteracts the upward repulsion due to the X_2 state. For the $A_2^4\Sigma_{3/2}^-$ state there is no such counteracting repulsion relative to the X_1 state. The A_1 and A_2 states cross each other at $r = 4.6 a_0$, at which point the X_2 state lies much closer than the B state, resulting in a net upward repulsion of the A_1 state. The $A^4\Sigma^-$ bond lengths determined experimentally are $\approx 0.16\text{\AA}$ larger than those for X_1 and X_2 states, which result in very good agreement with the present calculations (Table 2.2). This difference is much smaller than for IO. The $A_1 - A_2$ splitting is computed to be 890 cm^{-1} and agrees well

with the experimental value of 897 cm^{-1} [12]. The emission spectra for transitions from the $A^4\Sigma^-$ components are expected to contain shorter progressions than in IO because of the smaller $A - X r_e$ difference. There should also be more bound vibrational levels from which emission can occur, although this distinction is somewhat offset by the lower ω_e value of the IO A state [14]. These frequencies have been calculated for TeF and the values are in good agreement with those measured experimentally (Table 2.2). The T_e values of the $A^4\Sigma^-$ states are underestimated by about $\sim 1100 \text{ cm}^{-1}$ in the present work.

The $B^2\Sigma_{1/2}^-$ state shows a potential maximum at $r \approx 5.8 a_0$. We know that there are four $\Omega = 1/2$ states converging to the $\text{Te}(^3P_2)$ atomic limit, and the highest one comes from the $^2\Sigma^+$ state, which is repulsive at large distances. The $B^2\Sigma^-$ state has a deeper minimum but it also appears to have a repulsive limb starting much farther out than $^2\Sigma^+$, although the effect could also be due to deficiencies in the present theoretical treatment. The B state has been observed experimentally [7-9,12]. The computed T_e value is about 1600 cm^{-1} higher than that measured (Table 2.2). This is probably an indication that the higher-lying $\Omega = 1/2$ states which tend to interact with the B state are not very well described. This presumption is supported by the fact that the error in the computed ω_e value for the B state is greater than for the X and A Ω components. The longer r_e value is consistent with the fact that its potential well is shallower than for the A states. No experimental results are available for comparison of the r_e value.

Above the B state lie the two bound Ω components of the $C^2\Delta$ state, namely $C_1^2\Delta_{5/2}$ and $C_2^2\Delta_{3/2}$, with a quite small SO splitting between them. The computed T_e values for the C states are about 1824 cm^{-1} higher than that measured during recent experiments [52]. Due to the small SO splitting the assignment as the 3/2 and 5/2 Ω states should be considered as tentative. Both components show an avoided crossing

with the higher-lying repulsive states of similar Ω symmetry. The maxima at $r \approx 5.0 a_0$ also support this conclusion. Though the C_1 and C_2 states are shallow, their potential wells nonetheless support quite a few vibrational levels and, hence, their discrete spectra should be experimentally observable. The computed spectroscopic constants for these states are also listed in Table 2.2. The $1^2\Sigma^+$ state lying above the C states has a potential minimum at $\approx 4.15 a_0$. It has a very shallow potential well and supports a single vibrational level.

2.3 Transition Moments and Radiative Lifetimes

In order to calculate the transition moment between the various Ω states, it is necessary to know their composition in terms of $\Lambda - S$ eigenfunctions. The c^2 percentage contributions of the various $\Lambda - S$ states in the eight lowest Ω states of TeF are listed in Table 2.3 for various internuclear distances. The calculation of transition moments also requires the electric dipole and transition moments between the various $\Lambda - S$ eigenfunctions. From Table 2.3 it is clear that in the Franck-Condon (FC) region of the ground state, there is very little mixing and the states are predominantly $\Lambda - S$ in character. The $A_1^4\Sigma_{1/2}^-$ state is, however, seen to have a 3.4 – 4.0 % admixture of the $^2\Sigma^+$ state in the FC region of the ground state. There is a gradual increase in $X^2\Pi$ character, being 3.0 % at $r = 3.95 a_0 \approx r_e(A_1)$, 9.7 % at $r = 5.0 a_0$, and 29.3 % at $r = 6.25 a_0$. The A_2 wavefunctions also show a gradual increase in $X^2\Pi$ character, but mixing with other $\Lambda - S$ states at $r \leq 5.0 a_0$ does not occur. The $B^2\Sigma_{1/2}^-$ state mixes over the whole internuclear distance range rather strongly with $^2\Sigma^+$. At longer bond lengths it also mixes with the $X^2\Pi$ and from $r = 6.25 a_0$ onwards the SO mixing is quite strong. The $C_1^2\Delta_{5/2}$ exhibits almost pure $^2\Delta$ $\Lambda - S$ character in the FC region. From $r = 5.0 a_0$ the SO mixing becomes obvious in this state. The $C_2^2\Delta_{3/2}$ mixes to a small extent with

the ${}^2\Pi \Lambda - S$ states throughout the FC region. From $r = 5.0 a_0$ onwards it shows strong mixing with various $\Lambda - S$ states. The $1^2\Sigma^+$ state is predominantly ${}^4\Sigma^-$ in character at very short internuclear distances. In the FC region of the ground state, however, it has mostly ${}^2\Sigma^+$ character with small admixtures of the ${}^2\Sigma^-$ and ${}^4\Sigma^- \Lambda - S$ states. For $r \geq 5.0 a_0$ this state exhibits the strongest SO mixing of all the states discussed here.

In the present system it is found that the perpendicular transitions are more intense than the parallel ($\Delta\Omega = 0$) ones, which is the opposite of the usual situation for the diatomic molecules. This behaviour can be very simply explained from the fact that there are only two allowed $\Lambda - S$ transitions among the low-lying states, namely, $B^2\Sigma^- - X^2\Pi$ and $C^2\Delta - X^2\Pi$, and they are both perpendicular. The $1^2\Sigma^+ - X^2\Pi$, which also plays a small role, is also perpendicular. The parallel (μ_z) low-lying transitions are quite weak and arise mainly from the dipole moment values that come into play because both upper and lower Ω states involved have contributions from the same $\Lambda - S$ state. The computed parallel and perpendicular transition moments are shown in Figs. 2.3 and 2.4, respectively.

The parallel transition moments for TeF are quite small at short internuclear distances because the Ω states are of almost pure $\Lambda - S$ character and even dipole moment contributions are negligible. As the SO mixing starts becoming significant, it is mostly the dipole moment difference between the states involved that determine the magnitude of the parallel transition moments. For example, the $X^2\Pi$ and $A^4\Sigma^-$ dipole moments values are 1.09 and 1.13 ea_0 at $r = 3.65 a_0$, 1.35 and 1.49 ea_0 at $r = 3.95 a_0$, and 1.45 and 1.65 ea_0 at $r = 4.10 a_0$. Hence, parallel transition moments in the FC region of the ground state are quite small (Fig. 2.3). As the internuclear distance increases ($r \geq 5.0 a_0$), the two values change in the opposite direction and their difference increases. At the same time, the mixing between the corresponding $\Lambda - S$ states

Table 2.3: Composition of the eight lowest Ω states of TeF (c^2 , %) at various bond distances r . Entries are only made for contributions with $c^2 \geq 1.0$ %.

State	r/a_0	$X^2\Pi$	$B^2\Sigma^-$	$1^2\Sigma^+$	$1^2\Delta$	$A^4\Sigma^-$	$1^4\Sigma^+$	$1^4\Pi$	$1^4\Delta$
$X_1^2\Pi_{3/2}$	3.00	98.0							
	3.65 ^a	96.8				2.5			
	3.95	94.2			1.0	4.6			
	4.00	93.8			1.0	5.0			
	4.10	92.5			1.2	6.1			
	4.15	91.7			1.3	6.9			
	5.00	70.5			1.6	27.0			
	6.25	55.2			1.6 ^b	38.5			
$X_2^2\Pi_{1/2}$	3.00	98.0							
	3.65 ^a	98.2				1.3			
	3.95	96.0				3.4			
	4.00	95.3				4.0			
	4.10	93.4				6.0			
	4.15	92.0				7.6			
	5.00	10.0		1.5		85.3			
	6.25	1.4	2.9	3.7 ^b		74.0		12.9 ^b	
$A_1^4\Sigma_{1/2}^-$	3.00			2.9		96.0			
	3.65	1.0		3.5		95.0			
	3.95 ^a	3.0		3.7		92.6			
	4.00	3.6		3.8		92.0			
	4.10	5.4		4.0		90.0			
	4.15	7.0		4.2		89.0			
	5.00	84.0	3.0	2.7 ^b		9.1			
	6.25	29.3	50.0			2.5	1.5	14.4	
$A_2^4\Sigma_{3/2}^-$	3.00					99.0			
	3.65	2.4				97.1			
	3.95 ^a	4.5				94.8			
	4.00	5.0				94.8			
	4.10	6.0				94.0			
	4.15	6.8				93.1			
	5.00	25.4				70.4			
	6.25	24.6			3.4	30.5	5.7	32.7	

Continued ...

Table 2.3: Composition of the eight lowest Ω states of TeF (c^2 , %) at various bond distances r . Entries are only made for contributions with $c^2 \geq 1.0$ %.

State	r/a_0	$X^2\Pi$	$B^2\Sigma^-$	$1^2\Sigma^+$	$1^2\Delta$	$A^4\Sigma^-$	$1^4\Sigma^+$	$1^4\Pi$	$1^4\Delta$
$B^2\Sigma_{1/2}^-$	3.00		92.2	6.3					
	3.65		91.1	7.6					
	3.95		91.0	7.4					
	4.00		90.8	7.5					
	4.10 ^a		90.7	7.4					
	4.15		90.5	7.6					
	5.00	2.9	82.8	7.8					
	6.25	3.2 ^b	31.8	31.3		15.1	14.3		
$C_1^2\Delta_{5/2}$	3.00				99.6				
	3.65				99.5				
	3.95				98.7				
	4.00				99.2				
	4.10 ^a				98.8				
	4.15				98.2				
	5.00				73.6			21.1	3.8
	6.25				43.0 ^b			46.3	7.2
$C_2^2\Delta_{3/2}$	3.00				99.4				
	3.65	1.3 ^b			98.4				
	3.95	1.3 ^b			97.9				
	4.00 ^a	2.4 ^b			97.2				
	4.10	2.7 ^b			97.0				
	4.15	2.3 ^b			97.0				
	5.00	13.1 ^b			70.7	3.3 ^b		6.1	4.9
	6.25	30.5 ^b			17.3	29.6 ^b		20.4	
$1^2\Sigma_{1/2}^+$	3.00		3.0 ^b	5.0 ^b		91.4 ^b			
	3.65		8.3	87.7		2.7			
	3.95	1.5 ^b	8.0	87.0		2.7			
	4.00	1.6 ^b	8.2	86.6		2.8			
	4.10	1.9 ^b	8.1	86.1		2.8			
	4.15 ^a	2.0 ^b	8.2	85.5		2.8			
	5.00	3.5 ^b	20.7 ^b	38.0 ^b		9.8 ^b		25.0 ^b	
	6.25	31.2 ^b	9.3	10.6		15.3 ^b	16.2	10.1 ^b	

^a An approximate equilibrium distance for this state.

^b Contributions from the higher-lying roots of this symmetry are included.

Table 2.4: Partial and total radiative lifetimes (in s) for transitions from the $v' = 0$ level of the TeF excited states to the $X_1^2\Pi_{3/2}$ (τ_1) and $X_2^2\Pi_{1/2}$ (τ_2) states.

State	τ_1	τ_2			τ_{tot}
		τ_{\perp}	τ_{\parallel}	τ	
$X_2^2\Pi_{1/2}$	8.2 (-3) ^a				8.2 (-3)
$A_1^4\Sigma_{1/2}^-$	7.2 (-3)	91.4 (-3)	2.5 (-3)	2.4 (-3)	1.8 (-3)
$A_2^4\Sigma_{3/2}^-$	217 (-6)	63.7 (-3)			216 (-6)
$B^2\Sigma_{1/2}^-$	9.5 (-6)	36.1 (-6)	149 (-6)	29.1 (-6)	7.2 (-6)
$C_1^2\Delta_{5/2}$	14.5 (-6)				14.5 (-6)
$C_2^2\Delta_{3/2}$	18.6 (-3)	24.5 (-6)			24.5 (-6)

^a Numbers in parentheses indicate powers of ten.

increases (Table 2.3) and the parallel transition moments increase sharply (Fig. 2.3) for both $\Omega = 1/2$ and $3/2$ $A - X$ transitions. The $B - X_2$ transition is quite weak as expected from the composition of these states (Table 2.3). These two states have no common $\Lambda - S$ components other than contributions from $^2\Sigma^+$ and $^4\Sigma^-$ states at larger r values. The $C_2 - X_1$ and $X_2 - ^1\Sigma^+$ parallel transitions are also quite weak for the same reason. Since all these states dissociate to the same atomic limit, the transition moments connecting them fall off to zero at the dissociation limit.

The partial and total radiative lifetimes for the $v' = 0$ levels of the various excited states of TeF discussed in the present work are given in Table 2.4. The $X_2 - X_1$ fine structure transition is very weak, as is obvious from Fig. 2.4. The computed lifetime is 8.3 m.s. The $A_1 - X_1$ transition is of comparable strength, whereas the parallel $A_1 - X_2$

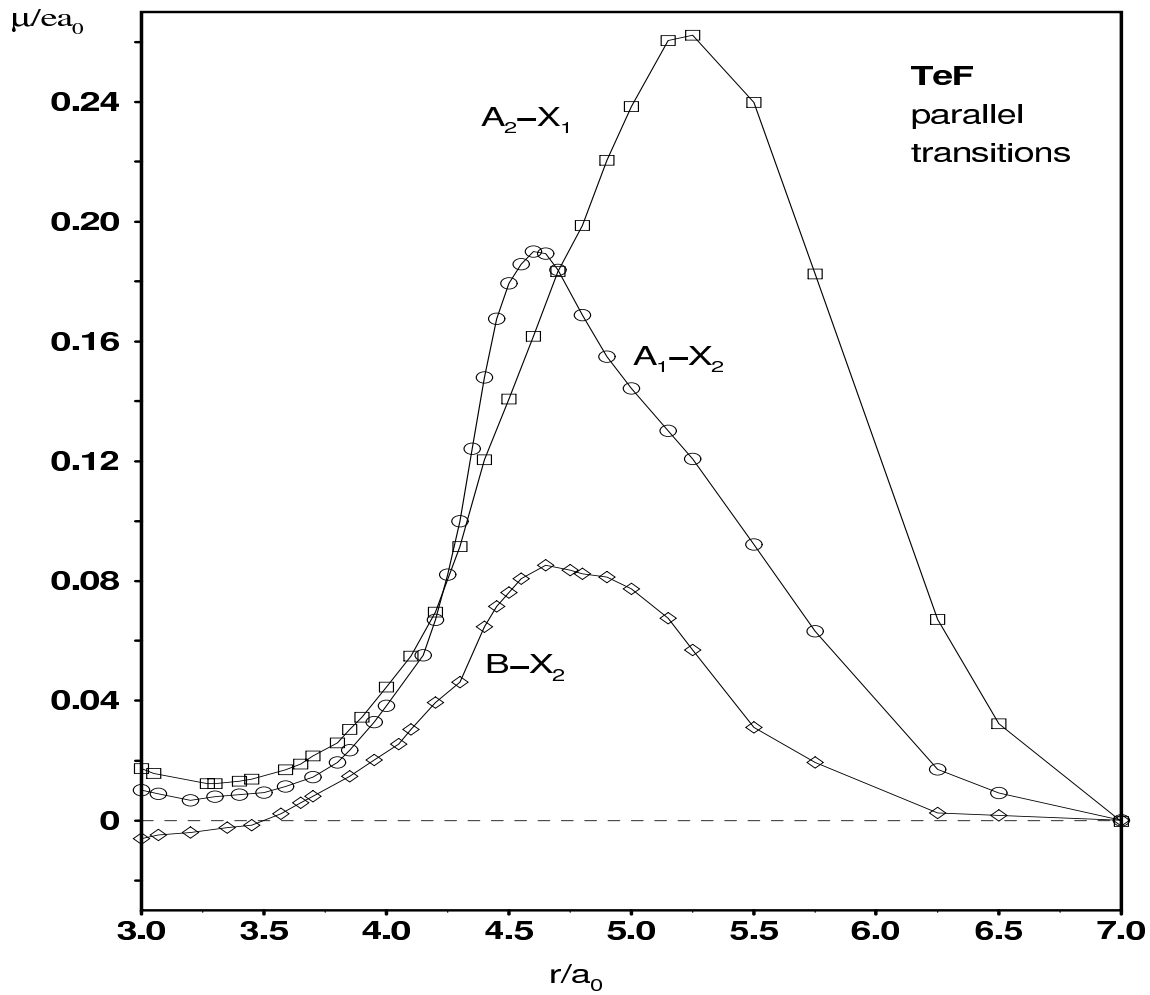


Figure 2.3: Computed electric dipole moments for parallel transitions from the $A_1 \ 4\Sigma_{1/2}^-$, $A_2 \ 4\Sigma_{3/2}^-$, and $B \ 2\Sigma_{1/2}^-$ states to the $X_1 \ 2\Pi_{3/2}$ and $X_2 \ 2\Pi_{1/2}$ states of TeF.

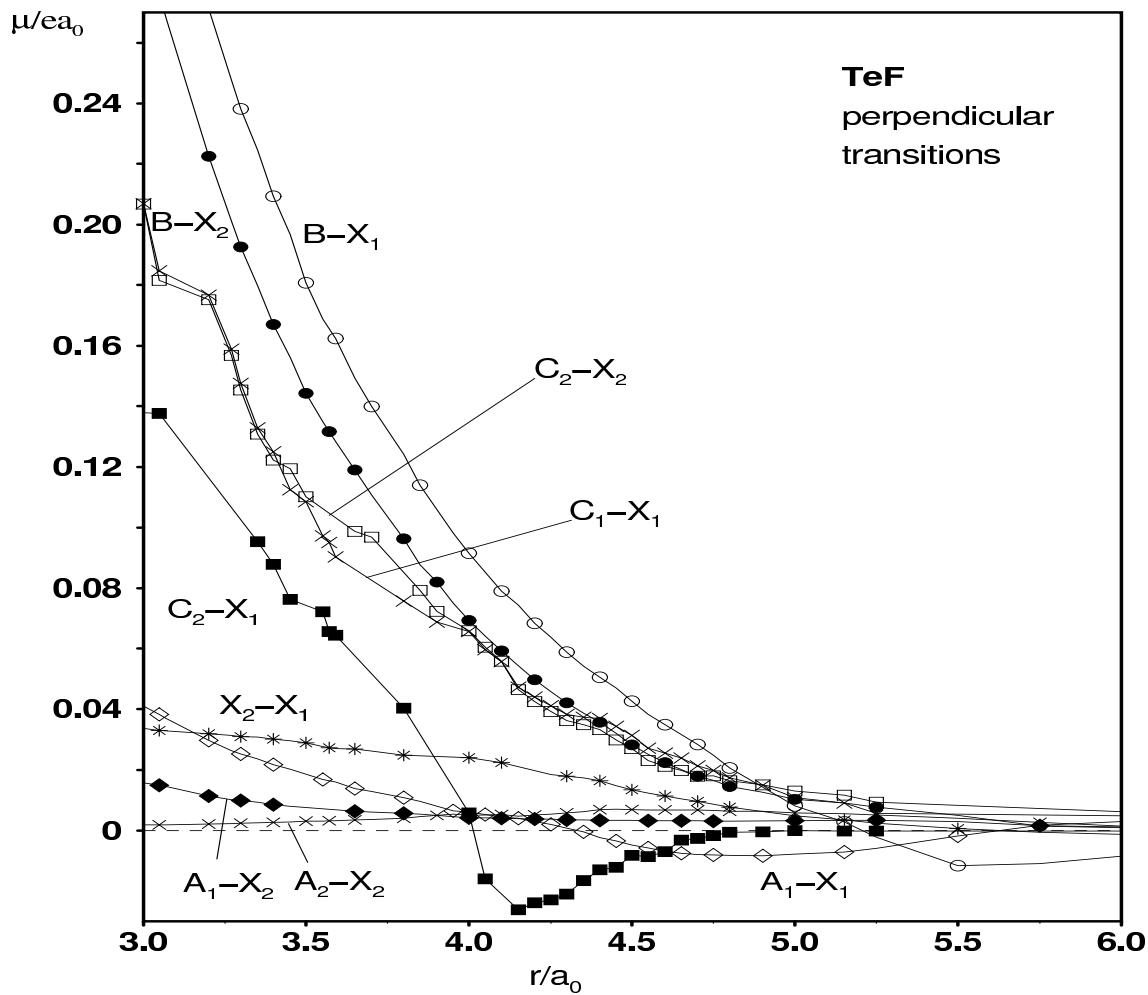


Figure 2.4: Computed electric dipole moments for perpendicular transitions from the $X_2 \ ^2\Pi_{1/2}$, $A_1 \ ^4\Sigma_{1/2}^-$, $A_2 \ ^4\Sigma_{3/2}^-$, $B \ ^2\Sigma_{1/2}^-$, $C_1 \ ^2\Delta_{5/2}$, and $C_2 \ ^2\Delta_{3/2}$ states to the X_1 and X_2 states of TeF.

Table 2.5: Calculated partial (τ_{\perp} , τ_{\parallel} , τ) and total (τ_{tot}) radiative lifetimes (in μs) for the $B \rightarrow X_1, X_2$ transitions from the $v' = 0 - 5$ vibrational levels of the upper state.

v'	$B \rightarrow X_1$	$B \rightarrow X_2$			$B \rightarrow X_1, X_2$
	τ_{\perp}	τ_{\perp}	τ_{\parallel}	τ	τ_{tot}
0	9.5	36.1	149	29.1	7.2
1	9.1	32.7	134	26.3	6.8
2	8.7	30.1	113	23.8	6.4
3	8.3	27.9	108	22.2	6.0
4	7.9	26.0	113	21.1	5.7
5	7.5	24.2	117	20.1	5.5

transition has a lifetime about 3 times shorter, resulting in a total lifetime of $1.8ms$ for the A_1 state. The A_2 lifetime is much shorter than that of the A_1 state. Its measured lifetime is $44 \mu s$ [12]. The present calculations show that the $A_2 - X_1$ partial lifetime is $217 \mu s$ which is still about 5 times longer than that reported experimentally. The disagreement could be due to the problematics arising in calculations of such small transition moments, but it may also be due to experimental difficulties in measuring such weak transition.

The strongest low-energy transition in the present study of TeF is calculated to be $B - X_1$. Both the X_1 and X_2 states are accessible for the B state via $\Delta\Omega = \pm 1$ transitions. Though most of the computed perpendicular transition moment values are quite small ($\leq 0.04 ea_0$), the values corresponding to the $B - X$ transitions are relatively large. The composition of the B and X wave functions (Table 2.3) shows that the allowed $B^2\Sigma^- - X^2\Pi$ transition at the $\Lambda - S$ level is responsible for the computed Ω

transition moments. The transition moments drop fairly quickly towards the dissociation limit. To explain this, it is to be noted that in this region the leading configuration for $X^2\Pi$ changes from $\sigma^2\pi^4\pi^{*3}$ to $\sigma\pi^4\pi^{*3}\sigma^*$. The latter configuration corresponds to neutral atoms, which means that the charge distribution is very compact and hence there is little possibility of overlap. In the FC region the charge is more delocalized and the transition moment values increase rapidly. Such rapid changes cause strong variations in the radiative lifetimes with vibrational quantum number. This can be seen from the values listed in Table 2.5. There is a decrease of 21 % in lifetime from $v' = 0$ to 5 for the $B \rightarrow X_1$ transition and 33 % for the $B \rightarrow X_2$ transition. The computed partial radiative lifetime is $9.5 \mu s$ for the $B \rightarrow X_1$ transition, but no experimental result is as yet available for comparison. The $B \rightarrow X_2$ transition moment has both a parallel and a perpendicular component, with the parallel transitions about 4 – 5 times longer lived than their perpendicular counterparts (Table 2.4). The partial lifetime of the $B - X_2$ transition is about four times longer than that of $B - X_1$ (Table 2.4). Both $B \rightarrow X$ transitions have the same $\Lambda - S$ origin, the difference in their lifetimes is mainly due to the $\Delta\bar{E}^3$ [see equation (1.41)] factor involved in the lifetime calculation. The measured $B - X_2$ transition would include both parallel and perpendicular transitions and should have a radiative lifetime of $29.1 \mu s$ according to the present calculations. This value has been obtained by adding the two Einstein coefficients and then taking the reciprocal. The total lifetime of the B state also includes a contribution from the $B - X_1$ transition. Calculating similarly, the value obtained as the total radiative lifetime of the B state is $7.2 \mu s$. Meanwhile new experimental studies have been carried out on TeF [52] and the radiative lifetime of the B state has been observed to be $8.5 \pm 0.5 \mu s$, which is in very good agreement with the value obtained from the theoretical computations.

The calculated partial radiative lifetimes for transitions from the C_1 and C_2 states are also listed in Table 2.4. The corresponding perpendicular transitions are of compa-

Table 2.6: Partial and total radiative lifetimes (in s) for transitions from the $v' = 0$ level of the TeF $C_{1,2}$ states to the $X_{1,2}$ states at various internuclear distances.

r/a_0	$C_1 \rightarrow X_1$	$C_2 \rightarrow X_1$			$C_2 \rightarrow X_2$
		τ_{\perp}	τ_{\parallel}	τ_{tot}	
3.85	5.3 (-6) ^a	234 (-6)	395 (-3)	234 (-6)	99.6 (-6)
3.95	11.1 (-6)	25 (-6)	27.7 (-3)	24.9 (-6)	21.4 (-6)
4.00 ^b	9.5 (-6)	1.28 (-3)	11.9 (-3)	1.28 (-3)	18.8 (-6)
4.05	12.9 (-6)	178 (-6)	13.5 (-3)	175 (-6)	25.5 (-6)
4.10 ^c	15.2 (-6)	467 (-6)	714 (-6)	282 (-6)	31.8 (-6)
4.15	26.9 (-6)	66 (-6)	228 (-6)	51.1 (-6)	51.5 (-6)
4.25	37.9 (-3)	116 (-6)	324 (-6)	85.3 (-6)	85.9 (-6)

^a Numbers in parantheses indicate powers of ten.

^b approximate r_e for C_2 state.

^c approximate r_e for C_1 state.

rable strength to those from the B state. The calculated Ω transition moments are also shown in Fig. 2.4 and it is clear that the values are relatively large though smaller than that for the $B - X$ transitions. There is a change of sign in the transition moment at the approximate r_e value for the upper C_2 state in the case of the $C_2 - X_1$ perpendicular transition (Fig. 2.4). The swift change in the transition moment values for this process results in a change of radiative lifetime values with internuclear distance (Table 2.6). Recent experiments carried out on TeF report the radiative lifetimes of the C_1 and C_2 states to be $7 \pm 1 \mu s$ [52]. The lifetime for the C states measured is shorter than that for the B state, whereas the calculated lifetimes have the opposite trend.

Chapter 3

Tellurium Chloride (TeCl)

This chapter describes a series of *ab initio* spin-orbit configuration interaction (SO-CI) calculations carried out for the TeCl radical by employing relativistic effective core potentials (RECPs). Various energetic properties, dipole transition moments and radiative lifetimes have been computed for the low-lying valence states and predictions about the strongest transitions in the low-energy spectra of these systems have been made.

3.1 Details of the Theoretical Treatment

The $(4s4p5d2f)/(4s4p2d2f)$ basis set for Te, as described in the previous chapter, has been used to treat the $4d$, $5s$, and $5p$ electrons of the Te atom in the present theoretical treatment. For the chlorine atom only seven outer electrons have been treated explicitly. The inner shells were treated by employing the RECP of ref. [35]. A $(7s7p3d1f)$ basis set for the Cl atom has been taken from ref. [53].

The theoretical treatment follows a $\Lambda - S$ contracted spin-orbit CI (LSC-SO-CI)

scheme, [37,54] taking into account the relativistic effects at a correlated level and hence allowing a simple calculation and analysis of the one-electron properties. The calculations have been carried out employing the Table-Direct CI version [55,56] of the MRD-CI program package including configuration selection and perturbative corrections [28]. As explained in the previous chapter, the SCF calculations have been carried out for the first excited state $^4\Sigma^-(\sigma^2\pi^4\pi^{*2}\sigma^*)$ in order to obtain the MOs to be used at the CI level of calculations.

Details of the multireference CI treatment for the $\Lambda - S$ states (without inclusion of the spin-orbit interaction) are given in Table 3.1 for the TeCl equilibrium distance. The calculations have been carried out in C_{2v} symmetry. The configuration selection threshold T was set to be $1.0 \times 10^{-6} E_h$. To estimate the full CI energy at $T = 0$, the generalized Davidson correction [29,36] which takes into account the effects of higher than double excitations with respect to the reference configurations, was applied to the extrapolated energies at $T = 0$ for each root. The total number of symmetry adapted functions (SAFs) lies in the range of $(8 - 35) \times 10^6$ and are generated from 56 - 178 reference configurations, depending on the $\Lambda - S$ symmetry. For the doublet states of each C_{2v} irreducible representation six to nine roots have been calculated. For the quartet the number of roots is between two and five. The $\sum c_i^2$ values over reference configurations fall in the 0.88 - 0.91 range in each case. The leading electronic configurations are also given in Table 3.1. The calculations have been carried out over a distance range of $3.5 a_0$ to $10.0 a_0$, with a typical increment of $0.1 a_0$ in the FC region.

The $4d$ electrons of the tellurium atom have been treated as a frozen core in the CI and spin-orbit calculations because they are not very important for describing the low-lying states that are of interest in the present work. Thus only 13 electrons are involved in the CI excitation process.

Table 3.1: Technical details of the MRD-CI calculations of TeCl.^a

C_{2v}	N_{ref}/N_{root}	SAFTOT/SAFSEL	$C_{\infty v}$	Leading conf.	Σc_i^2
${}^2B_{1,2}$	178/7	35147942/149440	$1^2\Pi$	$\sigma^2\pi^4\pi^*3$	0.91
			$2^2\Pi$	$\sigma^2\pi^3\pi^*4$	0.88
			$3^2\Pi$	$\sigma^2\pi^4\pi^*\sigma^*2$	0.90
			$4^2\Pi$	$\sigma^2\pi^4\pi^*2\pi^{**}$	0.88
			$1^2\Phi$	$\sigma\pi^4\pi^*3\sigma^*$	0.88
			$5^2\Pi$	$\sigma^2\pi^4\pi^*2\pi^{***}$	0.88
			$6^2\Pi$	$\sigma^2\pi^4\pi^*2\pi^{**}$	0.88
2A_1	160/7	25146740/128899	$1^2\Delta$	$\sigma^2\pi^4\pi^*2\sigma^*$	0.90
			$1^2\Sigma^+$	$\sigma^2\pi^4\pi^*2\sigma^*$	0.90
			$2^2\Sigma^+$	$\sigma\pi^4\pi^*4$	0.89
			$2^2\Delta$	$\sigma^2\pi^4\pi^*2\sigma^{**}$	0.89
			$3^2\Delta$	$\sigma^2\pi^3\pi^*3\sigma^*$	0.89
			$3^2\Sigma$	$\sigma^2\pi^3\pi^*3\sigma^*$	0.88
			$4^2\Delta$	$\sigma^2\pi^3\pi^*3\sigma^*$	0.88
2A_2	113/7	25896632/114143	$1^2\Sigma^-$	$\sigma^2\pi^4\pi^*2\sigma^*$	0.90
			$1^2\Delta$	$\sigma^2\pi^4\pi^*2\sigma^*$	0.90
			$2^2\Sigma^-$	$\sigma^2\pi^4\pi^*2\sigma^{**}$	0.89
			$3^2\Sigma^-$	$\sigma^2\pi^3\pi^*3\sigma^*$	0.88
			$2^2\Delta$	$\sigma^2\pi^4\pi^*2\sigma^{**}$	0.89
			$4^2\Sigma$	$\sigma^2\pi^4\pi^*2\sigma^{***}$	0.89
			$3^2\Delta$	$\sigma^2\pi^3\pi^*3\sigma^*$	0.89
${}^4B_{1,2}$	129/2	31704976/50702	$1^4\Pi$	$\sigma\pi^4\pi^*3\sigma^*$	0.90
			$2^4\Pi$	$\sigma^2\pi^4\pi^*2\pi^{**}$	0.89
4A_1	102/2	21646934/33745	$1^4\Delta$	$\sigma^2\pi^3\pi^*3\sigma^*$	0.89
			$1^4\Sigma^+$	$\sigma^2\pi^3\pi^*3\sigma^*$	0.89
4A_2	109/3	24622451/81434	$1^4\Sigma^-$	$\sigma^2\pi^4\pi^*2\sigma^*$	0.91
			$2^4\Sigma^-$	$\sigma^2\pi^4\pi^*2\sigma^{**}$	0.89
			$1^4\Delta$	$\sigma^2\pi^3\pi^*3\sigma^*$	0.89

^a The number of selected SAFs and the Σc_i^2 values over reference configurations are given for $r = 4.4$ $a_0 \approx r_e$. SAFTOT designates the total number of generated, SAFSEL the number of selected SAFs, N_{ref} and N_{root} refer to the number of reference configurations and roots treated, respectively.

The $\Lambda - S$ eigenfunctions are then used as a basis for the final spin-orbit CI calculations. Since TeCl is a system with an odd number of electrons, all $\Lambda - S$ symmetries contribute to the spin-mixed Ω states in the C_{2v} double group. The actual symmetry is higher, however, which allows a relatively simple assignment of definite Ω values to the resulting eigenvectors. The eigenvectors obtained are of mixed-spin symmetry, the spin-orbit mixing being very weak for the low-lying states of interest in the FC region, and it becomes relatively strong only near the dissociation limit. Hence, the symmetry analysis in this case, as in that of TeF, is fairly easy.

Finally, the calculated potential energy curves for the Ω states employed to solve one-dimensional nuclear motion Schrödinger equations by means of the Numerov-Cooley method [32,33]. The electronic transition moments are averaged over various pairs of vibrational functions and combined with transition energy data to compute Einstein emission coefficients with all lower-lying vibrational states and then inverting to obtain the radiative lifetime value.

3.2 Potential Curves

Potential energy curves have been calculated for all 23 $\Lambda - S$ states converging to the three lowest dissociation limits, $\text{Te}(^3P) + \text{Cl}(^2P^o)$, $\text{Te}(^1D) + \text{Cl}(^2P^o)$, and $\text{Te}(^1S) + \text{Cl}(^2P^o)$. Most of the states are repulsive, however, and therefore only the 12 states going to the lowest $\text{Te}(^3P)$ limit and three of the nine states correlating with the second $\text{Te}(^1D)$ asymptote are shown in Fig. 3.1. The ground state symmetry is found to be $^2\Pi(\sigma^2\pi^4\pi^*3)$, similar to TeF. The ground state dissociation energy calculated without inclusion of spin-orbit coupling is 19440 cm^{-1} . The lowest excited states are $A^4\Sigma^-$,

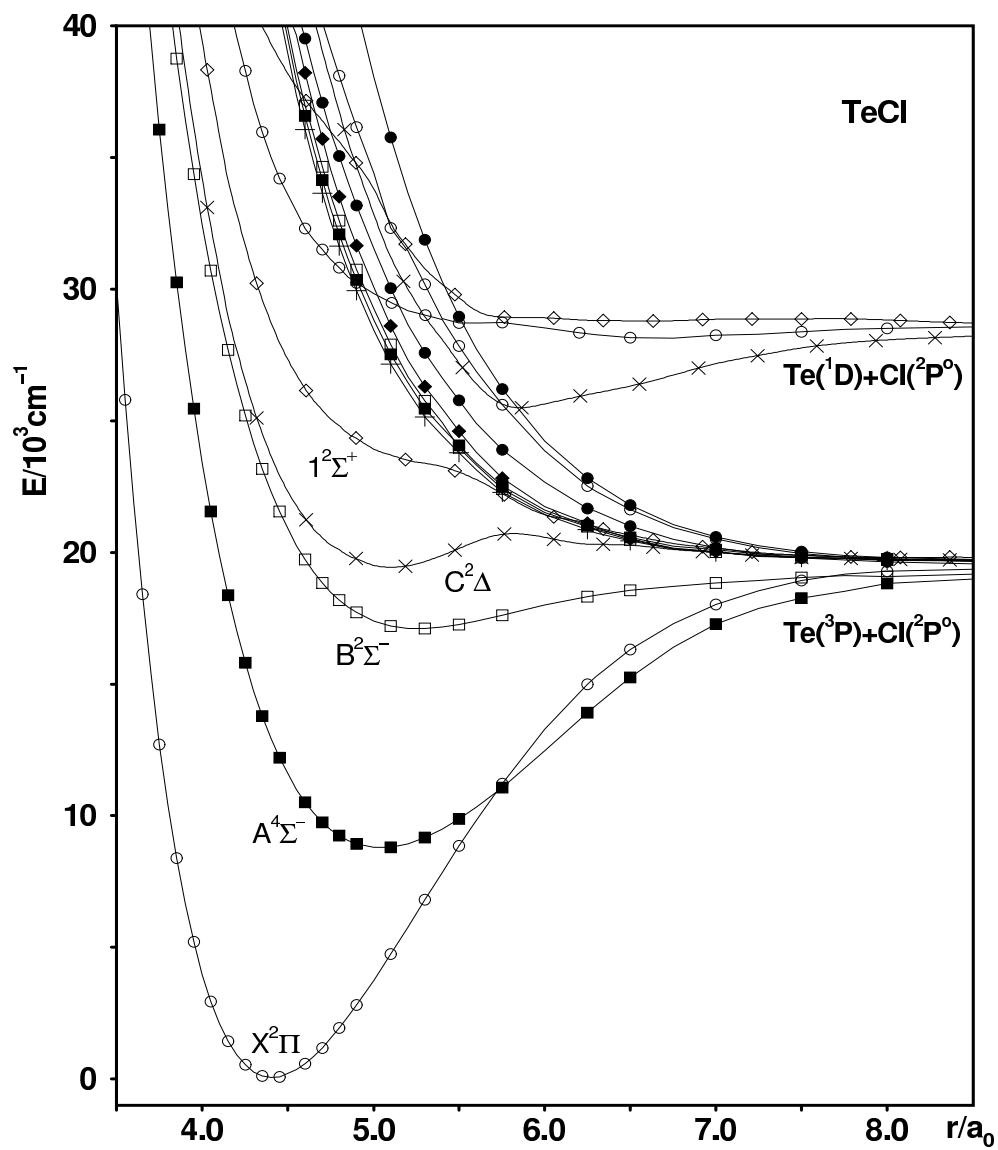


Figure 3.1: Computed potential energy curves for the low-lying $\Lambda - S$ states of TeCl obtained without inclusion of the spin-orbit interaction.

$B^2\Sigma^-$, $C^2\Delta$, and $1^2\Sigma^+$ in ascending order of energy. All these states have the same $\sigma^2\pi^4\pi^{*2}\sigma^*$ leading configuration in the FC region, which corresponds to the $\pi^* \rightarrow \sigma^*$ excitation relative to the ground state. As can be seen in Fig. 3.1, the $1^2\Sigma^+$ is repulsive as opposed to the slightly bound character found in TeF. This is an indication of the trend to be continued as we move on to the heavier systems, namely the states gradually lose their bound character and become increasingly more repulsive. The trend can be quite simply explained looking at the nature of the MOs. The $\pi^* \rightarrow \sigma^*$ excitation involves a transition from the lone-pair π^* orbital, which is almost completely localized on the Te atom, to the antibonding σ^* orbital. The antibonding character increases in the heavier TeX systems as the electronegativity difference between the Te and X atom becomes smaller, and this in turn leads to a decrease in bonding for the states generated from $\pi^* \rightarrow \sigma^*$ excitation as we move down the halide group.

The full spin-orbit Hamiltonian was diagonalised in the basis of $\Lambda - S$ states given in Table 3.1. The calculated potential energy curves for the resulting Ω are given in Fig. 3.2. The first ten Ω states dissociate to the $\text{Te}(^3P_2)+\text{Cl}(^2P_{3/2}^o)$ atomic limit. The computed D_e value for the $X_1^2\Pi_{3/2}$ ground state is obtained from calculations carried out for $r = 9.0 a_0$ and is found to be 19100 cm^{-1} . The lowering in the dissociation energy caused due to SO coupling is $\approx 340 \text{ cm}^{-1}$. The SO effect is not very large for TeCl because the open-shell π^* orbital has almost pure Te character, as already mentioned above, and thus its effect on the energy of this state is only weakly dependent on r .

There are five Ω states that dissociate to the second atomic limit, $\text{Te}(^3P_2)+\text{Cl}(^2P_{1/2}^o)$. They are all repulsive and only three have been included in Fig. 3.2. Two Ω states converge to the third $\text{Te}(^3P_0)+\text{Cl}(^2P_{3/2}^o)$ dissociation limit and one of them, a $1/2$ state possesses a shallow minimum at $r_e = 6.48 a_0$. The calculated spectroscopic constants for TeCl are listed in Table 3.2 along with the available experimental data. The $X^2\Pi$

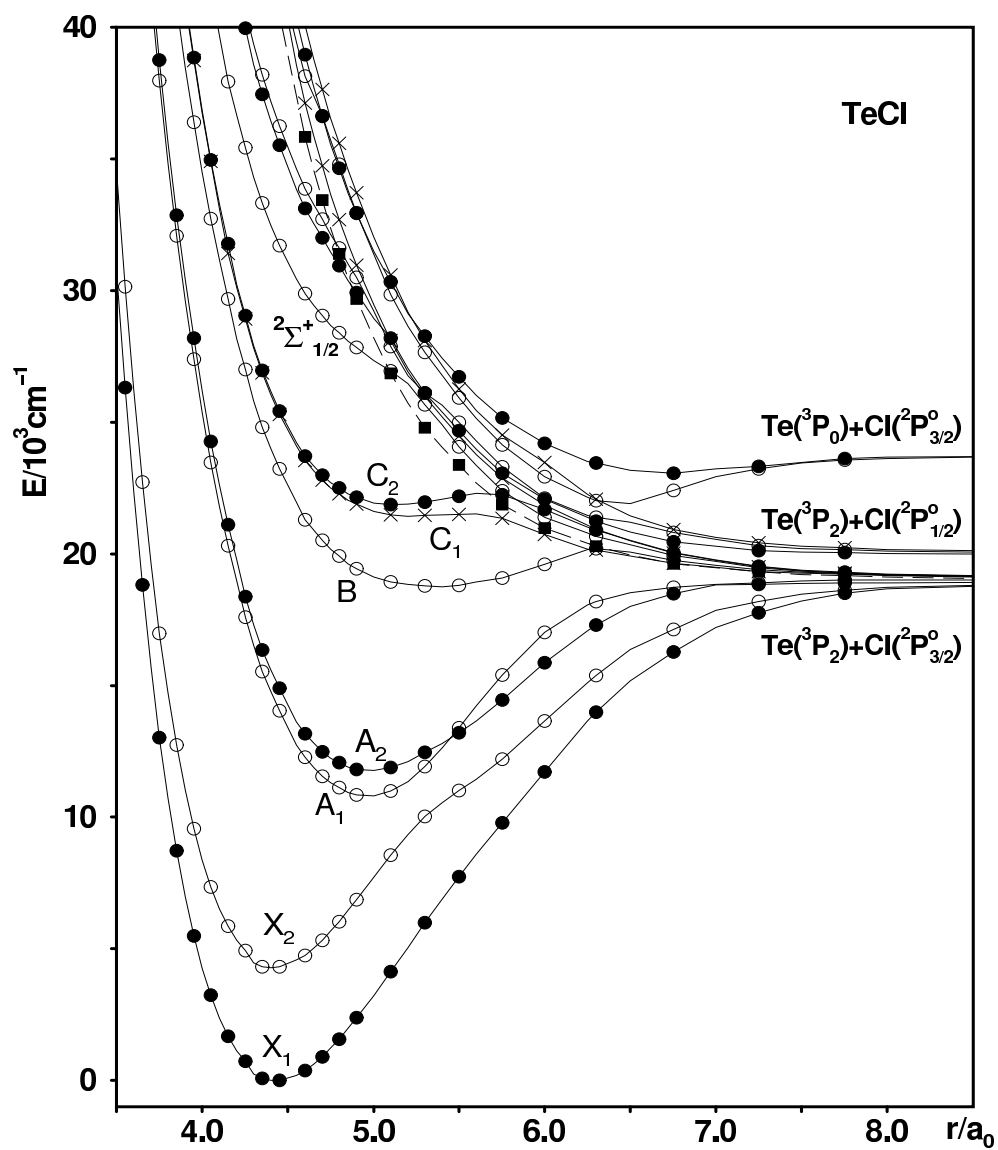


Figure 3.2: Computed potential energy curves for the low-lying Ω states of TeCl: \circ - $\Omega = 1/2$ states; \bullet - $\Omega = 3/2$ states; \times - $\Omega = 5/2$ states; and \blacksquare - $\Omega = 7/2$ state.

Table 3.2: Calculated (this work) and experimental spectroscopic properties of $^{130}\text{TeCl}$ (transition energy T_e , bond length r_e , and vibrational frequency ω_e).

State	T_e/cm^{-1}		$r_e/\text{\AA}$		ω_e/cm^{-1}	
	calc.	exp.	calc.	exp.	calc.	exp.
$X_1^2\Pi_{3/2}$	0	0	2.349	2.3206 [10]	374	386 [10]
$X_2^2\Pi_{1/2}$	4303	4022 [10]	2.342	2.3132 [10]	382	391 [10]
$A_1^4\Sigma_{1/2}^-$	10792	-	2.622	-	311	-
$A_2^4\Sigma_{3/2}^-$	11584	-	2.632	-	254	-
$B^2\Sigma_{1/2}^-$	18624	-	2.821	-	153	-

spin-orbit splitting of the ground state is overestimated by 281 cm^{-1} . The r_e values are calculated to be $\approx 0.03\text{ \AA}$ larger than the corresponding experimental results. The vibrational frequencies are underestimated by ca. 10 cm^{-1} . This indicates a slight underestimation of bonding strength in the present study. The reason could be the freezing of d -electrons at the CI stage and incompleteness of the AO basis sets employed. That the relative accuracy of the calculations is good can be demonstrated by the fact that the X_2 equilibrium value is calculated to be 0.007 \AA shorter than that of X_1 state and this is in almost perfect agreement with the shortening observed experimentally [10]. The sign and strength of the vibrational frequency change from X_1 to X_2 is also correctly predicted by the calculations.

The $A^4\Sigma^-$ state shows a much smaller SO splitting (792 cm^{-1}) than that of the $X^2\Pi$ ground state. The $A_1^4\Sigma_{1/2}^-$ component is lower in energy and exhibits an avoided crossing with $X_2^2\Pi_{1/2}$, resulting in a steep attractive branch of the A_1 branch, and as

a consequence, in a significantly larger ω_e value for the A_1 state than that of A_2 . The repulsion between these two states also reveals itself through a slight shoulder in the X_2 potential curve in the $5.2 - 5.5 a_0$ distance range. This distortion should be experimentally observable as irregular behaviour in the X_2 vibrational level spacings.

The next higher-lying state is $B^2\Sigma^-$. This state has a shallow minimum at $r_e = 5.3 a_0$. At an internuclear distance of approximately $6.2 a_0$, it undergoes an avoided crossing with the repulsive $1/2$ state which leads to the formation of a barrier on the B potential curve and causes the slightly bound $1/2$ state to dissociate to the third limit. The $C_1^2\Delta_{5/2}$ and $C_2^2\Delta_{3/2}$ states, which are bound in TeF, are repulsive in TeCl. The $C_2^2\Delta_{3/2}$ state shows a slight minimum but is not deep enough to support any vibrational levels. The $1^2\Sigma_{1/2}^+$ state shows no potential minimum in TeCl.

The $\Lambda - S$ compositions of the five lowest Ω states of TeCl are listed in Table 3.3. As was observed for TeF, the SO mixing in this case is also not very strong in the FC region of the ground state, but increases notably towards the dissociation limit.

3.3 Transition Moments and Radiative Lifetimes

As discussed in the previous chapter, the low-energy spectrum of the TeF radical is dominated by the allowed perpendicular transitions, $B^2\Sigma^-, C^2\Delta \rightarrow X^2\Pi$. For TeCl there are fewer bound states taking part in the transition process, however.

The calculated transition moments for parallel and perpendicular transitions of TeCl have been plotted in Figs. 3.3 and 3.4, respectively. The $X_2 - X_1$ fine structure transition is quite weak (Fig. 3.4). The corresponding lifetime for the X_2 state is calcu-

Table 3.3: Composition of the five lowest Ω states of TeCl (c^2 , %) at various bond distances r . Entries are only made for contributions with $c^2 \geq 1.0$ %.

State	r/a_0	$X^2\Pi$	$B^2\Sigma^-$	$1^2\Sigma^+$	$1^2\Delta$	$A^4\Sigma^-$	$1^4\Sigma^+$	$1^4\Pi$
$X_1^2\Pi_{3/2}$	4.2	98.3				1.2		
	4.4 ^a	97.4				1.9		
	5.0	90.9				7.6		
	5.3	84.1				13.8		
	5.5	76.9				19.4		
	6.5	60.5				33.6		
$X_2^2\Pi_{1/2}$	4.2	98.9						
	4.4 ^a	98.7						
	5.0	87.5				11.3		
	5.3	44.7	1.0			52.6		
	5.5	18.0		1.7		77.4		
	6.5	3.9	1.9	2.9		82.8		2.4
$A_1^4\Sigma_{1/2}^-$	4.2			4.2		94.8		
	4.4			4.2		94.4		
	5.0 ^a	10.7		4.7		83.4		
	5.3	52.5		3.9		41.7		
	5.5	76.9		3.3		16.8		
	6.5	39.4 ^b	42.3			4.4		5.8
$A_2^4\Sigma_{3/2}^-$	4.2	1.2				98.4		
	4.4	1.8				98.0		
	5.0 ^a	7.3				91.4		
	5.3	13.1				84.8		
	5.5	19.6				77.4		
	6.5	27.4			2.9	55.9 ^b	2.6	12.5
$B^2\Sigma_{1/2}^-$	4.2		91.4	7.2		1.1		
	4.4		91.1	7.3				
	5.0		89.9	7.1		1.1		
	5.3 ^a		88.4	7.0		1.0		
	5.5		86.7	6.8				
	6.5	6.1 ^b	25.9 ^b	36.1		17.8 ^b	9.1	

^a An approximate equilibrium distance for this state.

^b Contributions from the higher-lying roots of this symmetry are included.

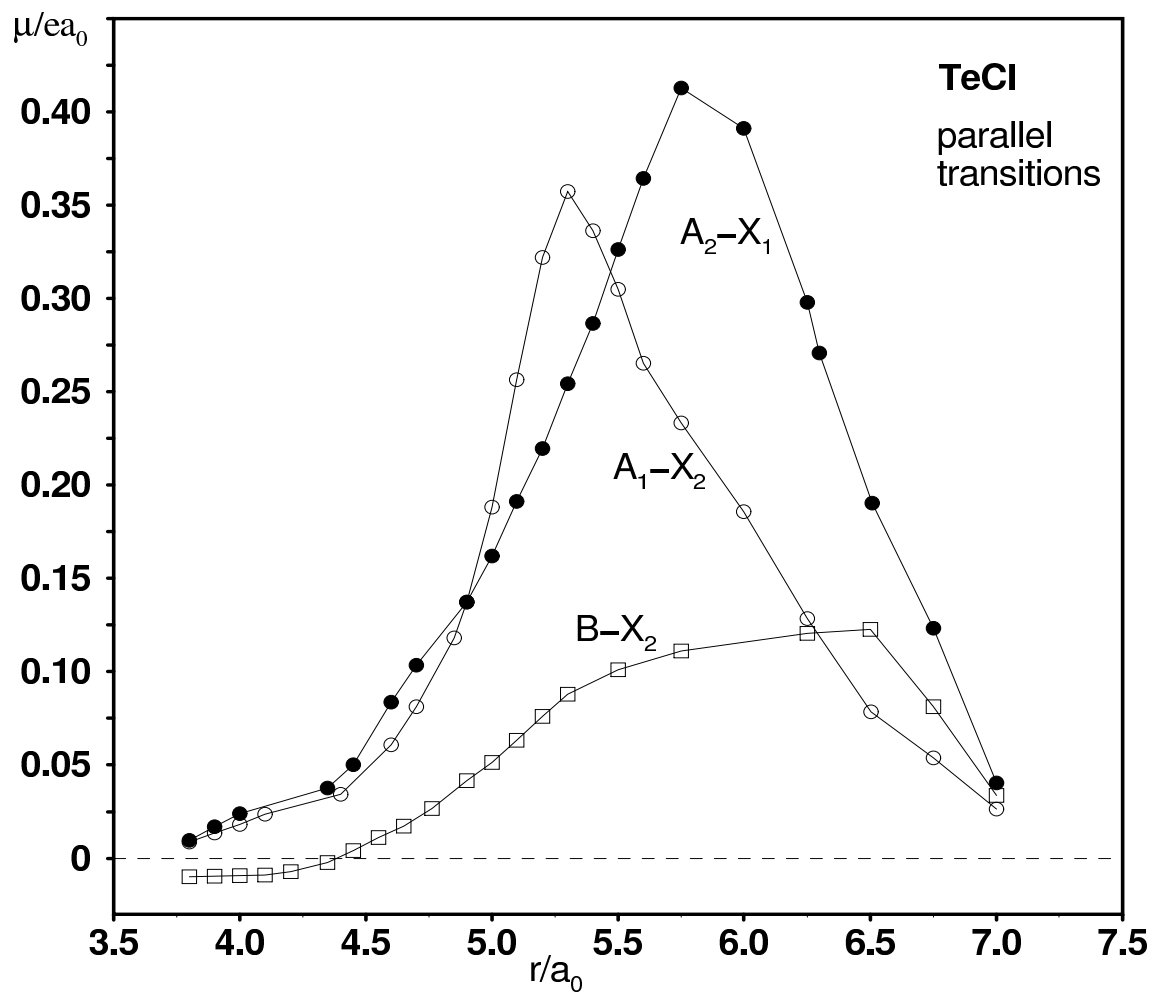


Figure 3.3: Computed electric dipole moments for parallel transitions from the A_1 $4\Sigma_{1/2}^-$, A_2 $4\Sigma_{3/2}^-$, and B $2\Sigma_{1/2}^-$ states to the X_1 $2\Pi_{3/2}$ and X_2 $2\Pi_{1/2}$ states of TeCl.

Table 3.4: Partial and total radiative lifetimes (in s) for transitions from the $v' = 0$ level of the TeCl excited states to the $X_1^2\Pi_{3/2}$ (τ_1) and $X_2^2\Pi_{1/2}$ (τ_2) states.

State	τ_1	τ_2			τ_{tot}
		τ_{\perp}	τ_{\parallel}	τ	
$X_2^2\Pi_{1/2}$	18.3 (-3) ^a				18.3 (-3)
$A_1^4\Sigma_{1/2}^-$	70.0 (-3)	46.2	378 (-6)	378 (-6)	376 (-6)
$A_2^4\Sigma_{3/2}^-$	29.4 (-6)	0.77			29.4 (-6)
$B^2\Sigma_{1/2}^-$	6.8 (-3)	467 (-3)	106 (-6)	106 (-6)	104 (-6)

^a Numbers in parentheses indicate powers of ten.

lated to be 18.3 ms (Table 3.4) and is quite similar to the value of 8.2 ms obtained for TeF. The $A_1 - X_1$ perpendicular transition has a longer lifetime than that of the $A_1 - X_2$ transition. The parallel component of the $A_1 - X_2$ transition is significantly stronger than the corresponding perpendicular component. Similarly, the perpendicular $A_2 - X_2$ has a longer lifetime than the corresponding parallel transition. Figs. 3.3 and 3.4 show the parallel transition moments for $A_1 - X_2$ and $A_2 - X_1$ to be more than an order of magnitude larger than the respective perpendicular transition moments. In the case of TeF the difference is somewhat smaller. The magnitudes of the $A_1 - X_2$ and $A_2 - X_1$ μ_z transition moments (Fig. 3.3) are comparable near the equilibrium distance of the $A_{1,2}$ states ($\approx 4.96 a_0$). The difference in lifetimes is mostly due to the difference in their transition energies.

Qualitatively, the two molecules, TeF and TeCl, seem to be very similar. Viewed from the quantitative perspective, however, the systems are seen to have some impor-

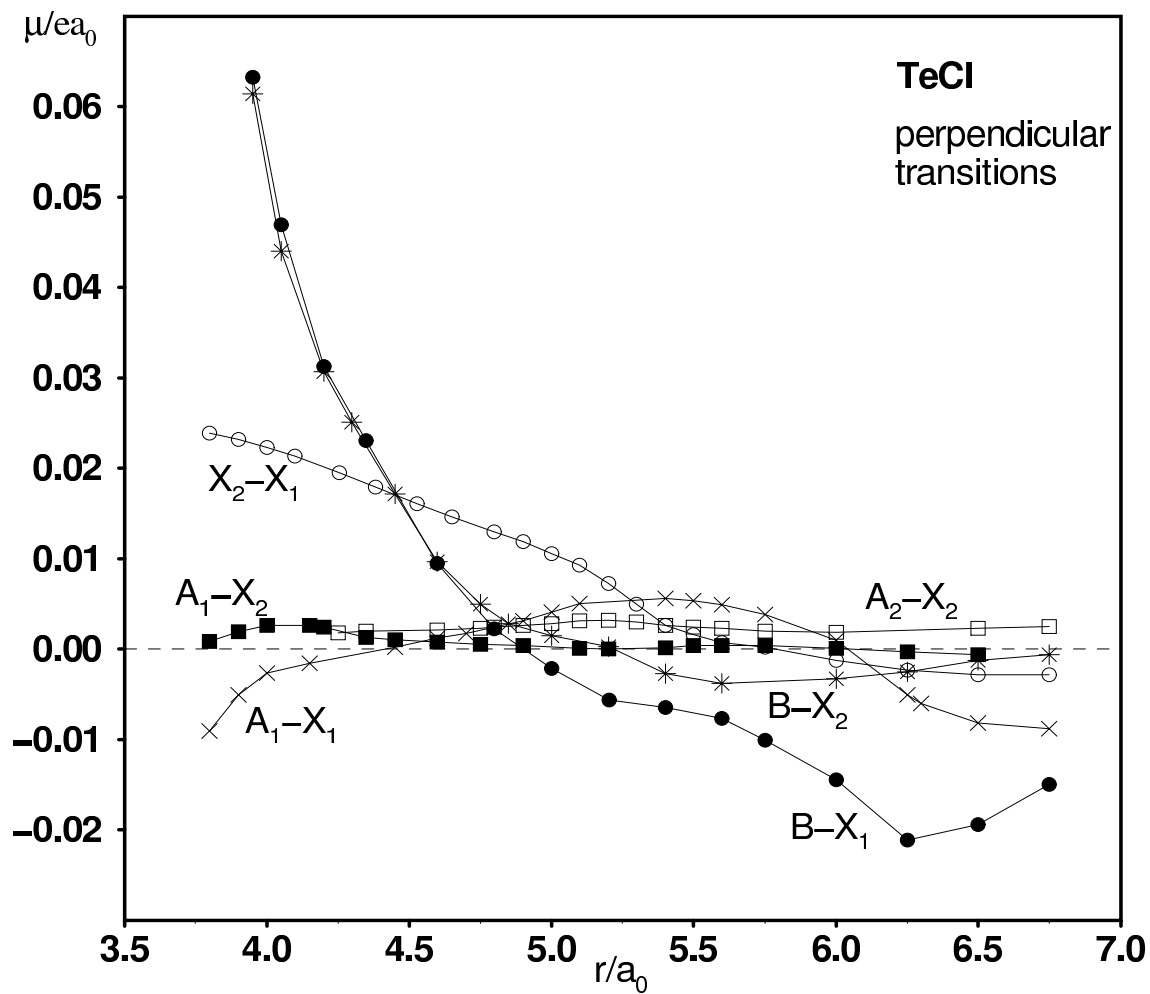


Figure 3.4: Computed electric dipole moments for perpendicular transitions from the $X_2 \ ^2\Pi_{1/2}$, $A_1 \ ^4\Sigma_{1/2}^-$, $A_2 \ ^4\Sigma_{3/2}^-$, and $B \ ^2\Sigma_{1/2}^-$ states to the X_1 and X_2 states of TeCl.

tant differences. The $B - X$ transitions in the two systems demonstrates this optimally. In TeF, the perpendicular transitions $B - X_1(1/2 - 3/2)$ and $B - X_2(\pm 1/2 - \mp 1/2)$ are found to be quite strong, with lifetimes in the microsecond range and both had a $\Lambda - S$ origin. In the case of TeCl the situation is significantly different. A look at the compositions of the various Ω states (Table 3.3) explains why. Around $5.3 a_0$, the approximate equilibrium distance of the B state, the $\Lambda - S$ composition of the X_1 and X_2 states changes rapidly. This occurs due to the crossing of the $X^2\Pi$ and $A^4\Sigma^-$ states in this distance range and their strong spin-orbit coupling. The effect is particularly pronounced for the X_2 and A_1 states, which undergo an avoided crossing at $r \approx 5.3 a_0$ (Fig. 3.2). This leads to a change in character of the X_2 state from $X^2\Pi$ to $A^4\Sigma^-$. This in turn causes a rapid fall in the $B - X_{1,2} \mu_{x,y}$ transition moment values and even a change in sign (Fig. 3.4), and as a consequence the lifetime is increased (Table 3.4). It is to be noted that such a change in the behaviour of the $B - X_{1,2}$ transition moments near the equilibrium distance of the B state makes the corresponding τ values very sensitive to the quality of the calculations. Thus the accuracy may not be as good as that for the strong transitions. In the case of TeF the spin-orbit mixing occurs much closer to the dissociation limit and hence does not cause nearly as much irregular behaviour for the $B \rightarrow X_{1,2}$ transitions.

Chapter 4

Tellurium Bromide (TeBr)

The present chapter deals with the results of *ab initio* multireference configuration interaction calculations including spin-orbit coupling for valence electronic states of tellurium bromide (TeBr). The results obtained are compared with those for the isovalent TeF and TeCl systems obtained earlier at a similar level of theoretical treatment and also with the available experimental data.

4.1 Details of the Theoretical Treatment

The $(4s4p5d2f)/[4s4p2d2f]$ basis set for Te, as described in Chapter 2, has been used to treat the $4d$, $5s$, and $5p$ electrons of the Te atom in the present theoretical treatment. For the bromine atom only seven outer electrons have been treated explicitly. The 28-electron RECP of ref. [57] was employed to describe the inner shells of the bromine atom. The basis set for Br is of the $(5s6p2d1f)$ type and has been taken from ref. [21], with omission of the $(1s1p1d)$ diffuse functions.

The theoretical treatment is essentially the same as in the previous cases. The

first step is the construction of molecular orbitals (MOs), as linear combinations of atomic orbitals (LCAOs) by an SCF calculation which is performed for the first excited state, $^4\Sigma^-(\sigma^2\pi^4\pi^{*2}\sigma^*)$, of the neutral TeBr radical. The π and π^* MOs are found to be predominantly Br($p_{x,y}$) and Te($p_{x,y}$) in character respectively throughout the internuclear distance range considered which varies from $3.4 a_0$ to $8.5 a_0$. The σ MO has predominantly Te(s) character in the FC region and towards longer internuclear distance becomes pure Te(p_z) in character. The σ^* MO has a mixed character of Te(s), Te(p_z), Br(s) and Br(p_z) atomic orbitals at short internuclear distances and in the FC region. Towards the dissociation limit it is almost a pure Br(p_z) atomic orbital.

Prior to beginning the CI level of treatment, the $4d$ electrons of Te were frozen as a core since they are not of much significance in the present studies of the low-lying states of the molecule and besides, this procedure simplifies the calculations. The details of the multireference CI treatment for the $\Lambda - S$ states are presented in Table 4.1 for the approximate equilibrium distance of the TeBr molecule ($\approx 4.70 a_0$). The calculations are carried out in formal C_{2v} symmetry. The configuration selection threshold T was set to be $2.0 \times 10^{-6} E_h$. The total number of generated symmetry adapted functions (SAFs) lies in the range of $(11 - 26) \times 10^6$, of which about $(2 - 13) \times 10^4$ are selected at the set T value. The number of roots calculated for the doublet states is six to nine, whereas for the quartet states the number of roots calculated is less and varies from two to five. The number of reference configurations lies in the range, 55 – 148, depending on the $\Lambda - S$ symmetry. The $\sum c_i^2$ values over the chosen reference space are seen to fall uniformly in the 0.90 – 0.92 range in each case. The leading electronic configuration for each root has also been listed in Table 4.1.

The $\Lambda - S$ eigenfunctions are then used as a basis for the final spin-orbit CI calculations. The spin-eigenfunctions thus obtained are then combined with the $\Lambda - S$

Table 4.1: Technical details of the MRD-CI calculations of TeBr.^a

C_{2v}	N_{ref}/N_{root}	SAFTOT/SAFSEL	$C_{\infty v}$	Leading conf.	Σc_i^2
${}^2B_{1,2}$	148/9	25879663/132931	$1^2\Pi$	$\sigma^2\pi^4\pi^*3$	0.91
			$2^2\Pi$	$\sigma^2\pi^3\pi^*4$	0.90
			$3^2\Pi$	$\sigma^2\pi^4\pi^*\sigma^*2$	0.90
			$1^2\Phi$	$\sigma\pi^4\pi^*3\sigma^*$	0.89
			$4^2\Pi$	$\sigma^2\pi^4\pi^*2\pi^{**}$	0.90
			$5^2\Pi$	$\sigma^2\pi^4\pi^*2\pi^{**}$	0.90
			$6^2\Pi$	$\sigma^2\pi^4\pi^*2\pi^{**}$	0.90
			$7^2\Pi$	$\sigma^2\pi^3\pi^*2\sigma^*2$	0.90
			$8^2\Pi$	$\sigma^2\pi^4\pi^*2\pi^{**}$	0.90
2A_1	84/8	13276005/87805	$1^2\Delta$	$\sigma^2\pi^4\pi^*2\sigma^*$	0.91
			$1^2\Sigma^+$	$\sigma^2\pi^4\pi^*2\sigma^*$	0.90
			$2^2\Sigma^+$	$\sigma\pi^4\pi^*4$	0.90
			$2^2\Delta$	$\sigma^2\pi^3\pi^*3\sigma^*$	0.90
			$3^2\Sigma^+$	$\sigma^2\pi^3\pi^*3\sigma^*$	0.90
			$3^2\Delta$	$\sigma^2\pi^3\pi^*3\sigma^*$	0.90
			$4^2\Delta$	$\sigma^2\pi^4\pi^*2\sigma^{**}$	0.90
			$4^2\Sigma^+$	$\sigma^2\pi^3\pi^*3\sigma^*$	0.90
			$1^2\Sigma^-$	$\sigma^2\pi^4\pi^*2\sigma^*$	0.92
2A_2	114/6	24804685/77340	$1^2\Delta$	$\sigma^2\pi^4\pi^*2\sigma^*$	0.92
			$2^2\Sigma^-$	$\sigma^2\pi^3\pi^*3\sigma^*$	0.92
			$3^2\Sigma^-$	$\sigma^2\pi^4\pi^*2\sigma^{**}$	0.91
			$2^2\Delta$	$\sigma^2\pi^3\pi^*3\sigma^*$	0.92
			$3^2\Delta$	$\sigma^2\pi^3\pi^*3\sigma^*$	0.92
			$1^4\Pi$	$\sigma\pi^4\pi^*3\sigma^*$	0.91
			$2^4\Pi$	$\sigma^2\pi^4\pi^*2\pi^{**}$	0.91
			$3^4\Pi$	$\sigma^2\pi^3\pi^*2\sigma^*2$	0.91
			$1^4\Delta$	$\sigma^2\pi^3\pi^*3\sigma^*$	0.90
4A_1	55/2	11635838/29968	$1^4\Sigma^+$	$\sigma^2\pi^3\pi^*3\sigma^*$	0.90
			$1^4\Sigma^-$	$\sigma^2\pi^4\pi^*2\sigma^*$	0.91
4A_2	56/5	11161682/91955	$1^4\Delta$	$\sigma^2\pi^3\pi^*3\sigma^*$	0.91
			$2^4\Sigma^-$	$\sigma^2\pi^4\pi^*2\sigma^{**}$	0.90
			$3^4\Sigma^-$	$\sigma^2\pi^3\pi^*3\sigma^*$	0.90
			$4^4\Sigma^-$	$\sigma^2\pi^4\pi^*2\sigma^{***}$	0.90

^a The number of selected SAFs and the Σc_i^2 values over reference configurations are given for $r = 4.7$ $a_0 \approx r_e$. SAFTOT designates the total number of generated, SAFSEL the number of selected SAFs, N_{ref} and N_{root} refer to the number of reference configurations and roots treated, respectively.

transition moment data to determine the corresponding Ω – state electronic transition moments at each r value. The Numerov-Cooley numerical integration procedure [32,33] was employed to solve the nuclear Schrödinger equations in order to obtain the corresponding vibrational energies and wave functions.

4.2 Potential Curves

Potential energy curves have been calculated for the three lowest dissociation limits, $\text{Te}(^3P)+\text{Br}(^2P^o)$, $\text{Te}(^1D)+\text{Br}(^2P^o)$, and $\text{Te}(^1S)+\text{Br}(^2P^o)$. Most of the states are seen to be repulsive in nature (Fig. 4.1). The ground state symmetry is found to be $^2\Pi(\sigma^2\pi^4\pi^{*3})$. The dissociation energy calculated without inclusion of spin-orbit coupling is 17360cm^{-1} for the ground state. The lowest excited states are $A^4\Sigma^-$, $B^2\Sigma^-$, $C^2\Delta$, and $1^2\Sigma^+$ in ascending order of energy. All these states have the same $\sigma^2\pi^4\pi^{*2}\sigma^*$ leading configuration in the FC region, which corresponds to the $\pi^* \rightarrow \sigma^*$ excitation relative to the ground state. As can be seen in Fig. 4.1, only the ground and the first excited state show a well-defined potential minimum. The other states are repulsive. This confirms the remark made in the previous chapter regarding the smaller number of bound states as one moves to the heavier monohalides of tellurium.

The calculated potential energy curves for the Ω states resulting after the diagonalisation of the full SO Hamiltonian in the basis of the $\Lambda - S$ states are shown in Fig. 4.2 Only states converging to the two lowest limits have been included in the figure. The valence states dissociating to the higher limits are repulsive and have been omitted. The computed D_e value for the $X_1\ ^2\Pi_{3/2}$ ground state is obtained from calculations carried out for $r = 8.50\ a_0$ and is found to be $16000\ \text{cm}^{-1}$. The lowering in the dissociation energy caused due to SO coupling is $\approx 1360\ \text{cm}^{-1}$, which is larger than in

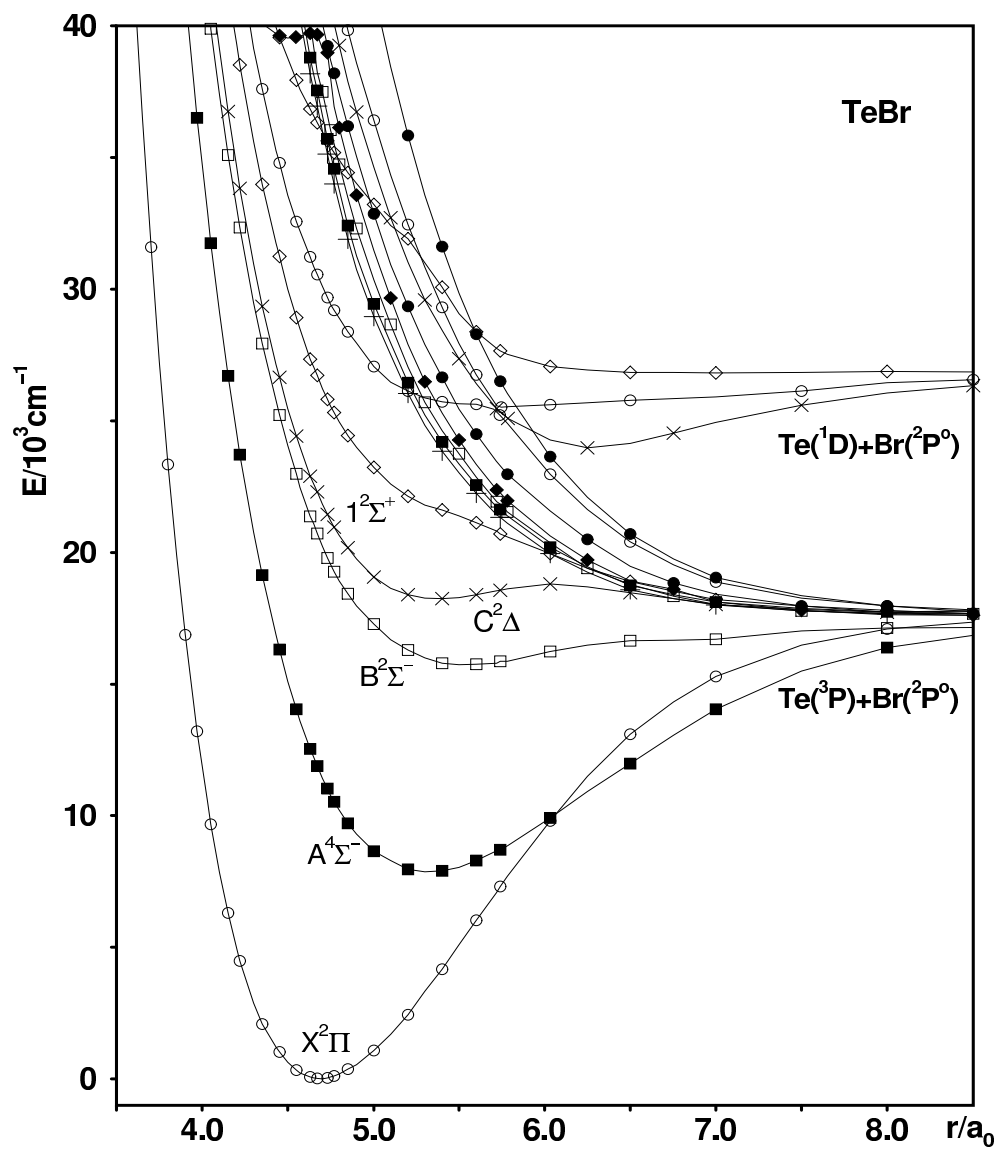


Figure 4.1: Computed potential energy curves for the low-lying $\Lambda - S$ states of TeBr obtained without inclusion of spin-orbit interaction.

Table 4.2: Calculated (this work) and experimental spectroscopic properties of $^{130}\text{TeBr}$ (transition energy T_e , bond length r_e , and vibrational frequency ω_e).

State	T_e/cm^{-1}		$r_e/\text{\AA}$		ω_e/cm^{-1}	
	calc.	exp.	calc.	exp.	calc.	exp.
$X_1^2\Pi_{3/2}$	0	0	2.494	-	250	-
$X_2^2\Pi_{1/2}$	4311	4067 [10]	2.491	-	257	-
$A_1^4\Sigma_{1/2}^-$	9756	-	2.774	-	221	-
$A_2^4\Sigma_{3/2}^-$	10592	-	2.805	-	181	-

the previous two cases by virtue of the much stronger spin-orbit contribution from the heavier halogen atom at the dissociation limit.

There are five Ω states that dissociate to the second atomic limit, $\text{Te}(^3P_2)+\text{Br}(^2P_{1/2}^o)$. They are all repulsive and only two have been included in Fig. 4.2. The calculated spectroscopic constants for TeBr are listed in Table 4.2 along with the available experimental data. The $X^2\Pi$ spin-orbit splitting of the ground state is overestimated by 244cm^{-1} . A similar overestimation has been observed in the present calculations for all the TeX systems. Our test calculations for the free Te atom have shown that this error arises partly from RECP spin-orbit operator deficiencies as well as from the Te basis set incompleteness. The r_e value of the X_2 state is calculated to be $\approx 0.03\text{\AA}$ larger than the corresponding value for the X_1 state. No experimental results are available for comparison purposes, however.

As in the previous cases, $A^4\Sigma^-$ state shows a much smaller SO splitting (836cm^{-1})

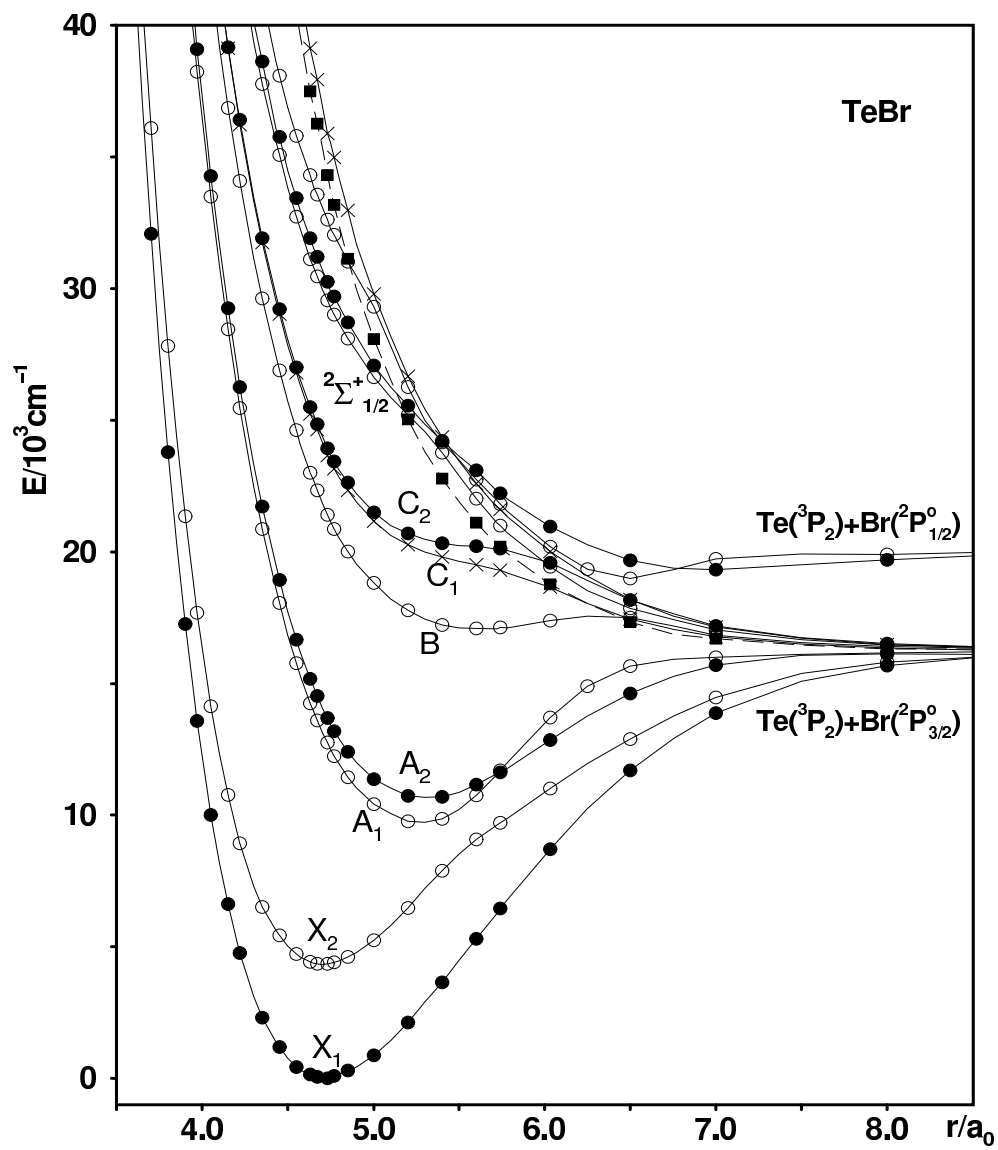


Figure 4.2: Computed potential energy curves for the low-lying Ω states of TeBr: \circ - $\Omega = 1/2$ states; \bullet - $\Omega = 3/2$ states; \times - $\Omega = 5/2$ states; and \blacksquare - $\Omega = 7/2$ state.

than the $X^2\Pi$ ground state. This splitting is comparable to that calculated for TeF (890cm^{-1}) and TeCl (792cm^{-1}), emphasising the dominant role of the Te atom in this effect. As in TeCl, the $A_1^4\Sigma_{1/2}^-$ component is lower in energy and exhibits an avoided crossing with $X_2^2\Pi_{1/2}$, resulting in a steep attractive branch of the A_1 potential, and as a consequence, in a significantly larger ω_e value for the A_1 state than for the A_2 state, similarly as in the case of TeCl. The next excited state is the $B^2\Sigma^-$, also as in the previous cases. It has a very shallow minimum at about $5.6 a_0$. The $C^2\Delta$ Ω components and the $1^2\Sigma_{1/2}^+$ state are also repulsive in the case of TeBr (Fig. 4.2).

4.3 Transition Moments and Radiative Lifetimes

The c^2 percentage contributions of the various $\Lambda - S$ states in the five lowest Ω states of TeBr are listed in Table 4.3 for various internuclear distances. From this table it is clear that in the FC region of the ground state, there is very little mixing and the states are predominantly $\Lambda - S$ in character. The $A_1^4\Sigma_{1/2}^-$ state is, however, seen to have a 4.8% admixture of $^2\Sigma^+$ state in the FC region of the ground state. There is an admixture of $X^2\Pi$, reaching 6.5% at $r = 5.20 a_0 \approx r_e(A_1)$. At an internuclear distance of $5.72 a_0$ the composition of the $X_2^2\Pi_{1/2}$ and $A_1^4\Sigma_{1/2}^-$ states changes completely, the former now exhibiting about 71% $^4\Sigma^-$ character and only 23% $^2\Pi$ character. The A_1 state at $5.72 a_0$ is an admixture of 73% $^2\Pi$, 22% $^4\Sigma^-$ and about 2% $^2\Sigma^+$ $\Lambda - S$ states. The A_2 wavefunction also shows a gradual increase in $X^2\Pi$ character, but mixing with other $\Lambda - S$ states is insignificant. The complete change of character observed for the 1/2 components of the X and A states is not found in the corresponding 3/2 Ω components (Table 4.3).

The calculated transition moments for parallel and perpendicular transitions in

Table 4.3: Composition of the five lowest Ω states of TeBr (c^2 , %) at various bond distances r . Entries are only made for contributions with $c^2 \geq 1.0$ %.

State	r/a_0	$X^2\Pi$	$B^2\Sigma^-$	$1^2\Sigma^+$	$1^2\Delta$	$A^4\Sigma^-$	$1^4\Sigma^+$	$1^4\Pi$	$1^4\Delta$
$X_1^2\Pi_{3/2}$	4.50	98.0				1.0			
	4.70 ^a	97.5				1.7			
	5.20	93.3				5.1			
	5.72	82.7				14.3			
	5.74	81.9				15.0			
	6.25	67.3				27.0			
	7.00	53.5				36.5 ^b	1.5		2.1
$X_2^2\Pi_{1/2}$	4.50	98.0				1.0			
	4.70 ^a	98.1				1.0			
	5.20	91.1				6.8			
	5.72	23.1				71.0			
	5.74	20.2	1.1	2.2		73.8			
	6.25	5.2	1.0	3.8 ^b		85.0			
	7.00	2.7	1.8	2.9 ^b		75.4		13.4 ^b	
$A_1^4\Sigma_{1/2}^-$	4.50			4.8		94.1			
	4.70			4.8		93.5			
	5.20 ^a	6.5		4.8		86.5			
	5.72	72.9		2.1		21.7			
	5.74	74.2	1.1	1.8		19.0			
	6.25	72.0	12.3			6.8 ^b			
	7.00	27.5 ^b	42.1 ^b			4.9 ^b	3.5	16.1 ^b	
$A_2^4\Sigma_{3/2}^-$	4.50					98.0			
	4.70	1.6				97.6			
	5.20 ^a	5.1				93.7			
	5.72	13.4				83.0			
	5.74	14.0				82.3			
	6.25	23.7				66.9 ^b	1.2	3.5	
	7.00	23.5				41.2 ^b	6.0	21.4 ^b	
$B^2\Sigma_{1/2}^-$	4.50		90.0	8.0		1.2			
	4.70		90.0	7.8		1.2			
	5.20	1.2 ^b	88.1	7.7		1.1			
	5.72 ^a	3.2 ^b	82.4	7.9		1.0			
	5.74	3.4 ^b	81.7	8.1		1.0		2.1	
	6.25	8.8	53.0 ^b	18.5		3.7 ^b		8.2 ^b	
	7.00	3.6 ^b	31.9 ^b	31.7		12.3 ^b	15.5		

^a An approximate equilibrium distance for this state.

^b Contributions from the higher-lying roots of this symmetry are included.

Table 4.4: Partial and total radiative lifetimes (in s) for transitions from the $v' = 0$ level of the TeBr excited states to the $X_1^2\Pi_{3/2}$ (τ_1) and $X_2^2\Pi_{1/2}$ (τ_2) states.

State	τ_1	τ_2			τ_{tot}
		τ_{\perp}	τ_{\parallel}	τ	
$X_2^2\Pi_{1/2}$	29.9 (-3) ^a				29.9 (-3)
$A_1^4\Sigma_{1/2}^-$	18.4 (-3)	0.97	396 (-6)	396 (-6)	388 (-6)
$A_2^4\Sigma_{3/2}^-$	17.3 (-6)	5.2			17.3 (-6)
$B^2\Sigma_{1/2}^-$	511 (-6) ^b	306 (-3) ^b	294 (-6)		

^a Numbers in parentheses indicate powers of ten.

^b An estimate at $r_e(B)$.

TeBr are plotted in Figs. 4.3 and 4.4, respectively. The $X_1 - X_2$ transition is quite weak, as for TeF and TeCl, with a radiative lifetime of 29.9 ms (Table 4.4) for the X_2 state.

The parallel $A_2 - X_1$ and $A_1 - X_2$ transition moment values are much larger than that of their perpendicular counterparts, and, hence, their lifetimes are much shorter. The perpendicular transition $A_1 - X_1$ has a (partial) lifetime of 18.4 ms , comparable to that of TeF (7.2 ms). The transition moment values for the perpendicular $A_1 - X_1$ transition are quite similar in the two cases, being 0.01 ea_0 and 0.007 ea_0 at the approximate equilibrium bond length of the X_1 state for TeF and TeBr, respectively. The corresponding values at the equilibrium bond length of the A_1 state in TeF ($\approx 3.95 a_0$) and TeBr ($\approx 5.20 a_0$) are 0.007 ea_0 in both cases. The shorter radiative lifetime in the case of TeF is mainly due to the $\Delta\bar{E}^3$ factor [see equation (1.41)] that is present in the formula for these quantities. The transition moment values for TeCl are about ten times smaller

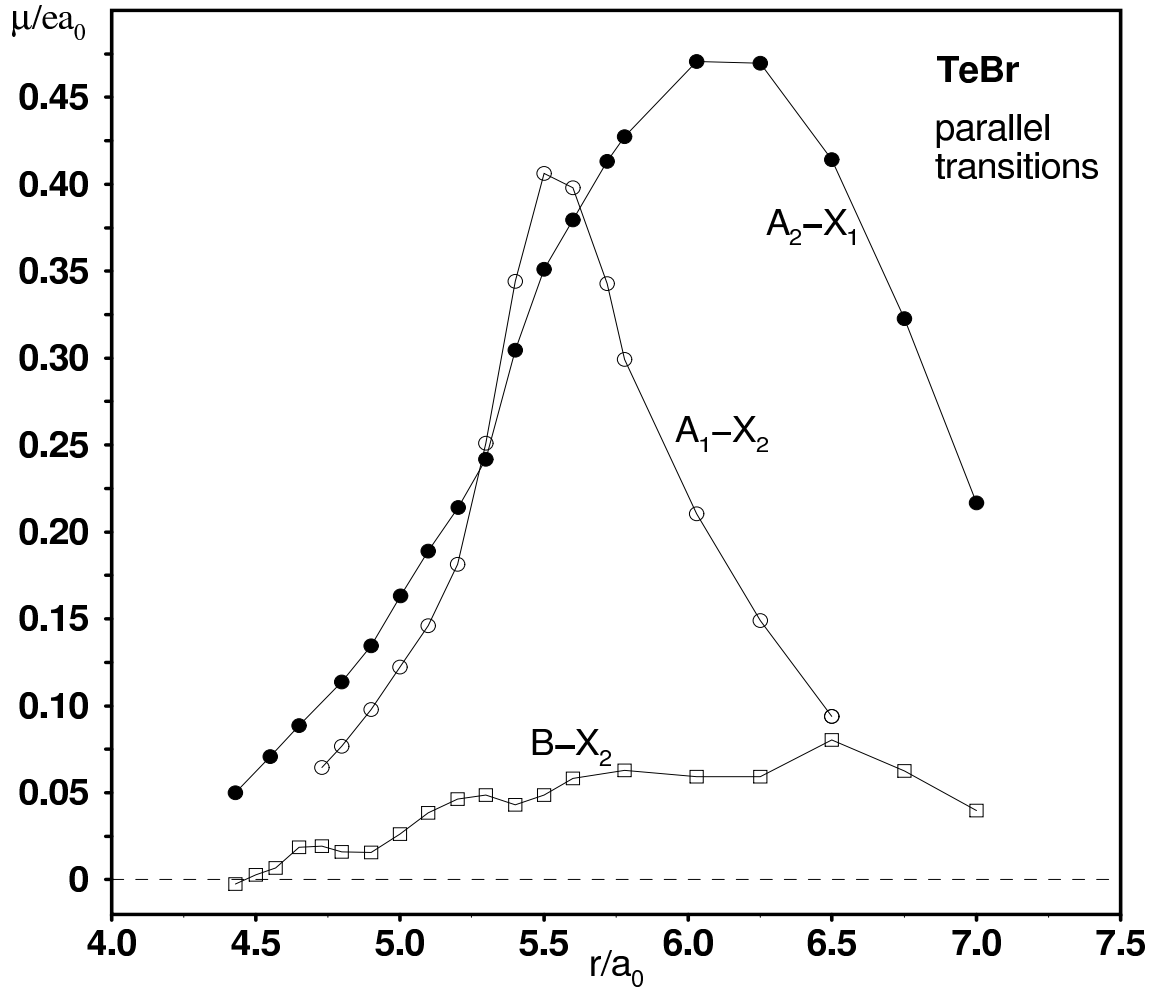


Figure 4.3: Computed electric dipole moments for parallel transitions from the A_1 $4\Sigma_{1/2}^-$, A_2 $4\Sigma_{3/2}^-$, and B $2\Sigma_{1/2}^-$ states to the X_1 $2\Pi_{3/2}$ and X_2 $2\Pi_{1/2}$ states of TeBr.

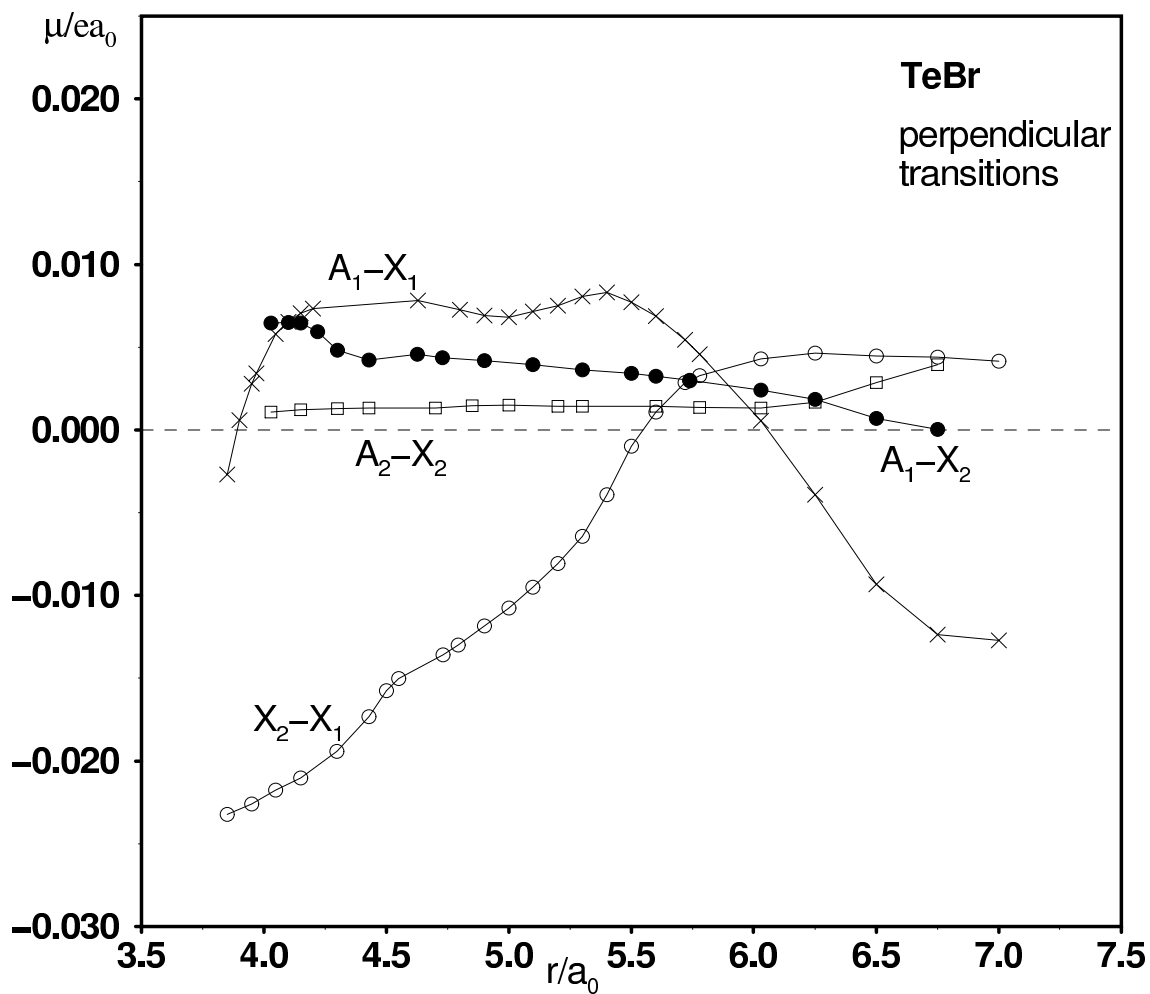


Figure 4.4: Computed electric dipole moments for perpendicular transitions from the $X_2 \ ^2\Pi_{1/2}$, $A_1 \ ^4\Sigma_{1/2}^-$, and $A_2 \ ^4\Sigma_{3/2}^-$ states to the X_1 and X_2 states of TeBr.

than that in TeF and TeBr and hence the corresponding lifetime for this transition is comparatively longer (70 ms) in TeCl (Table 3.4). The $A_1 - X_2$ perpendicular transition is calculated to have a partial lifetime of 0.97 s , which is quite long compared to that in TeF (91.4 ms) but shorter than that calculated for TeCl (46.2 s), the reason being the same as discussed in the above case for the $A_1 - X_1$ perpendicular transition. The parallel $A_1 - X_2$ transitions have comparable partial lifetimes in TeCl and TeBr, however, and are much shorter than in TeF. The explanation for this is simple, namely, as can be seen from Tables 3.3 and 4.3, the A_1 and X_1 states in TeCl and TeBr have contributions from the same $\Lambda - S$ states near r_e of the A_1 state, whereas in the case of TeF (Table 2.3) mixing at such short internuclear distances is negligible.

The B state in TeBr has a very shallow minimum at $r_e \approx 5.72 a_0$. The radiative lifetime for this state have been calculated at this r_e value. It is about 13 times shorter than for TeCl due to the significantly larger value of the $B - X_1$ transition moment in TeBr. The $B - X_2$ transitions have comparable lifetimes in TeCl and TeBr.

Chapter 5

Tellurium Iodide (TeI)

Tellurium iodide is the only monohalide of tellurium mentioned on the internet [58]. The webpage referred to describes tellurium iodide as being a black solid. The melting and boiling points, as well as the density are said to be unknown at the present time.

5.1 Details of the Theoretical Treatment

The $(4s4p5d2f)/[4s4p2d2f]$ basis set for Te, as described in Chapter 2, has been used to treat the $4d$, $5s$, and $5p$ electrons of the Te atom in the present theoretical treatment. For the iodine atom, as in the case of the previously discussed halides, only seven outer electrons have been treated explicitly. The 46-electron RECP of LaJohn et al. [34] was employed to describe the inner shells of the I atom. The basis set for iodine is of the type $(5s6p2d1f)$, similar to that used for the Br atom, and has been taken from ref. [21], except for the omission of the $(1s1p1d)$ diffuse functions.

The theoretical treatment follows a $\Lambda-S$ contracted spin-orbit (LSC-SO-CI) scheme [37,54]. The SCF calculations, performed for the first excited state ($^4\Sigma^-$) of TeI, gen-

erate the molecular orbitals (MOs) to be used in the CI stage of the calculation. As in other cases, the π and π^* MOs are found to be predominantly I($p_{x,y}$) and Te($p_{x,y}$) in character, respectively, throughout the internuclear distance range considered. The σ MO has predominantly Te(s) character in the FC region, but towards longer internuclear distances becomes pure I(p_z) in character, whereas in the other cases it assumes pure Te(p_z) character towards the dissociation limit. The σ^* MO has a mixed character of Te(s), Te(p_z), I(s) and I(p_z) atomic orbitals at short internuclear distances and in the FC region. Towards the dissociation limit it is almost a pure Te(p_z) atomic orbital.

Details of the multireference CI treatment for the $\Lambda - S$ states (without inclusion of the spin-orbit interaction) are given in Table 5.1 for the calculated equilibrium bond length of $5.05 a_0$. Calculations were carried out in C_{2v} symmetry, as in the other cases. The configuration selection threshold T was set to be $2.0 \times 10^{-6} E_h$. The number of symmetry adapted functions selected at this threshold lies in the $(17 - 71) \times 10^{-3}$ range, stemming from 66 – 102 reference configurations, depending on the $\Lambda - S$ symmetry. For the doublet states of each C_{2v} irreducible representation six roots were calculated, whereas for the quartet states 2 – 4 roots were calculated (Table 5.1). The $\sum c_i^2$ values over the reference configurations are found to fall in the 0.89 – 0.91 range for each case. The leading configuration for each root is also listed in Table 5.1. The $4d$ electrons of Te were treated as a frozen core in Tel as for the other three halides.

The $\Lambda - S$ eigenfunctions are employed as a basis for the final spin-orbit CI calculations. The spin-eigenfunctions thus obtained are then combined with the $\Lambda - S$ transition moment to obtain the corresponding $\Omega -$ state electronic transition moments at each r value. The Numerov-Cooley numerical integration procedure [32,33] was employed to solve the nuclear Schrödinger equations in order to obtain the corresponding vibrational energies and wave functions.

Table 5.1: Technical details of the MRD-CI calculations of TeI.^a

C_{2v}	N_{ref}/N_{root}	SAFTOT/SAFSEL	$C_{\infty v}$	Leading conf.	Σc_i^2
${}^2B_{1,2}$	102/6	11535337/71476	$1^2\Pi$	$\sigma^2\pi^4\pi^{*3}$	0.91
			$2^2\Pi$	$\sigma^2\pi^3\pi^{*4}$	0.90
			$3^2\Pi$	$\sigma^2\pi^4\pi^{*2}\sigma^{*2}$	0.90
			$1^2\Phi$	$\sigma\pi^4\pi^{*3}\sigma^*$	0.89
			$4^2\Pi$	$\sigma^2\pi^4\pi^{*2}\pi^{**}$	0.89
			$5^2\Pi$	$\sigma^2\pi^3\pi^{*2}\sigma^{*2}$	0.90
2A_1	98/6	9877459/42122	$1^2\Delta$	$\sigma^2\pi^4\pi^{*2}\sigma^*$	0.91
			$1^2\Sigma^+$	$\sigma^2\pi^4\pi^{*2}\sigma^*$	0.90
			$2^2\Sigma^+$	$\sigma\pi^4\pi^{*4}$	0.90
			$2^2\Delta$	$\sigma^2\pi^3\pi^{*3}\sigma^*$	0.90
			$3^2\Sigma^+$	$\sigma^2\pi^3\pi^{*3}\sigma^*$	0.90
			$4^2\Delta$	$\sigma^2\pi^3\pi^{*3}\sigma^*$	0.90
2A_2	71/6	9932446/49915	$1^2\Sigma^-$	$\sigma^2\pi^4\pi^{*2}\sigma^*$	0.90
			$1^2\Delta$	$\sigma^2\pi^4\pi^{*2}\sigma^*$	0.91
			$2^2\Sigma^-$	$\sigma^2\pi^3\pi^{*3}\sigma^*$	0.90
			$2^2\Delta$	$\sigma^2\pi^3\pi^{*3}\sigma^*$	0.90
			$3^2\Sigma^-$	$\sigma^2\pi^4\pi^{*2}\sigma^{**}$	0.90
			$4^2\Sigma^-$	$\sigma^2\pi^3\pi^{*3}\sigma^*$	0.90
${}^4B_{1,2}$	162/3	23493624/43821	$1^4\Pi$	$\sigma\pi^4\pi^{*3}\sigma^*$	0.90
			$2^4\Pi$	$\sigma^2\pi^3\pi^{*2}\sigma^{*2}$	0.90
			$3^4\Pi$	$\sigma^2\pi^4\pi^{*2}\pi^{**}$	0.89
4A_1	66/2	8823549/17891	$1^4\Delta$	$\sigma^2\pi^3\pi^{*3}\sigma^*$	0.90
4A_2	89/4	11551848/46137	$1^4\Sigma^+$	$\sigma^2\pi^3\pi^{*3}\sigma^*$	0.90
			$1^4\Sigma^-$	$\sigma^2\pi^4\pi^{*2}\sigma^*$	0.91
			$1^4\Delta$	$\sigma^2\pi^3\pi^{*3}\sigma^*$	0.89
			$2^4\Sigma^-$	$\sigma^2\pi^3\pi^{*3}\sigma^*$	0.89
			$3^4\Sigma^-$	$\sigma^2\pi^4\pi^{*2}\sigma^{**}$	0.90

^a The number of selected SAFs and the Σc_i^2 values over reference configurations are given for $r = 5.05$ $a_0 \approx r_e$. SAFTOT designates the total number of generated, SAFSEL the number of selected SAFs, N_{ref} and N_{root} refer to the number of reference configurations and roots treated, respectively.

5.2 Potential Curves

Potential energy curves have been calculated for all 23 $\Lambda - S$ states converging to the three lowest limits of $\text{Te}(^3P) + \text{I}(^2P^o)$, $\text{Te}(^1D) + \text{I}(^2P^o)$, and $\text{Te}(^1S) + \text{I}(^2P^o)$. Most of them are repulsive and hence only 12 states going to the lowest $\text{Te}(^3P)$ limit and two of the nine states correlating with the $\text{Te}(^1D)$ asymptote are shown in Fig. 5.1. The ground state symmetry is found to be $^2\Pi(\sigma^2\pi^4\pi^{*3})$, as in the other monohalides. The ground state dissociation energy calculated without inclusion of the spin-orbit interaction is 14430 cm^{-1} . The potential well for the ground state is shallower than in previous three cases and the equilibrium bond length is longer than in each of these cases. This trend is consistent with the increase in the size of the halogen atom radius and weakening of the bond relative to lighter TeX systems.

The lowest excited states are again $A^4\Sigma^-$, $B^2\Sigma^-$, $C^2\Delta$, and $1^2\Sigma^+$ in order of increasing energy, all arising from the $\pi^* \rightarrow \sigma^*$ excitation relative to the ground state. In TeI, only the ground state and the first excited states are seen to have a well defined potential minimum (Fig. 5.1), all other low-lying excited states having a repulsive potential.

Inclusion of the spin-orbit interaction yields the Ω states (Fig. 5.2). The ground state is an inverted $^2\Pi$. The ground state bonding in TeI (12100 cm^{-1}) is found to be the weakest of all the monohalides discussed in this work. The SO interactions lower the dissociation energy by 2300 cm^{-1} and are caused by the large contribution of the heavy I atom. The calculated spectroscopic constants for TeI, along with the available experimental results, are listed in Table 5.2. Except for the ground state splitting, no other experimental data are available for comparison.

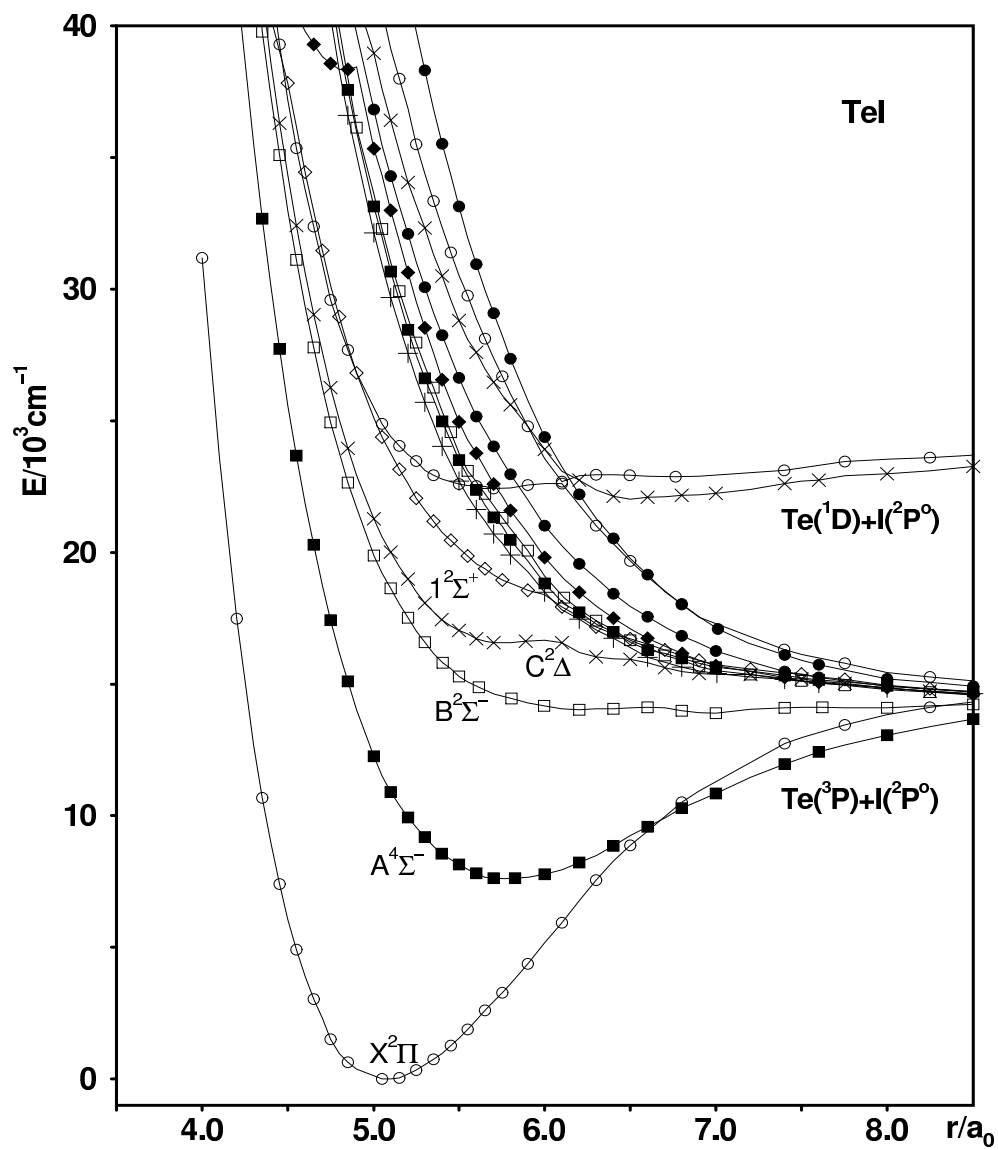


Figure 5.1: Computed potential energy curves for the low-lying $\Lambda - S$ states of TeI obtained without inclusion of the spin-orbit interaction.

Table 5.2: Calculated (this work) and experimental spectroscopic properties of ^{130}TeI (transition energy T_e , bond length r_e , and vibrational frequency ω_e).

State	T_e/cm^{-1}		$r_e/\text{\AA}$		ω_e/cm^{-1}	
	calc.	exp.	calc.	exp.	calc.	exp.
$X_1^2\Pi_{3/2}$	0	0	2.697	-	196	-
$X_2^2\Pi_{1/2}$	4348	4130 [10]	2.689	-	202	-
$A_1^4\Sigma_{1/2}^-$	9239	-	3.019	-	178	-
$A_2^4\Sigma_{3/2}^-$	10082	-	3.081	-	125	-

As in the case of the other halides, the $X_2^2\Pi_{1/2}$ component has a shorter r_e ($\approx 0.008 \text{ \AA}$) than the X_1 state. The ground state splitting is overestimated by about 218 cm^{-1} . The SO splitting of the $A^4\Sigma^-$ (843 cm^{-1}) state is much smaller than that of the X state. The $A_1^4\Sigma_{1/2}^-$ component is lower in energy and exhibits an avoided crossing with $X_2^2\Pi_{1/2}$, just as for TeCl and TeBr. Since the excitation energy of the A state is the lowest for TeI, this avoided crossing occurs much closer to the A_1 equilibrium distance than for either TeBr or TeCl. As a result of this avoided crossing the ω_e value of the A_1 state is much larger than that of the A_2 state. Both the A_1 and A_2 Ω states have longer r_e values than the $X_{1,2}$ states, which is consistent with their shallow potential wells. Most other states are calculated to be repulsive (Fig. 5.2) in TeI.

The c^2 percentage contributions of the various $\Lambda - S$ states in the four lowest Ω states of TeI are listed in Table 5.3 for various internuclear distances. As observed for the lighter monohalides, the SO effects in the FC region of the ground state are negligible. Also, as in the other monohalides, the $1/2$ Ω components of the X and

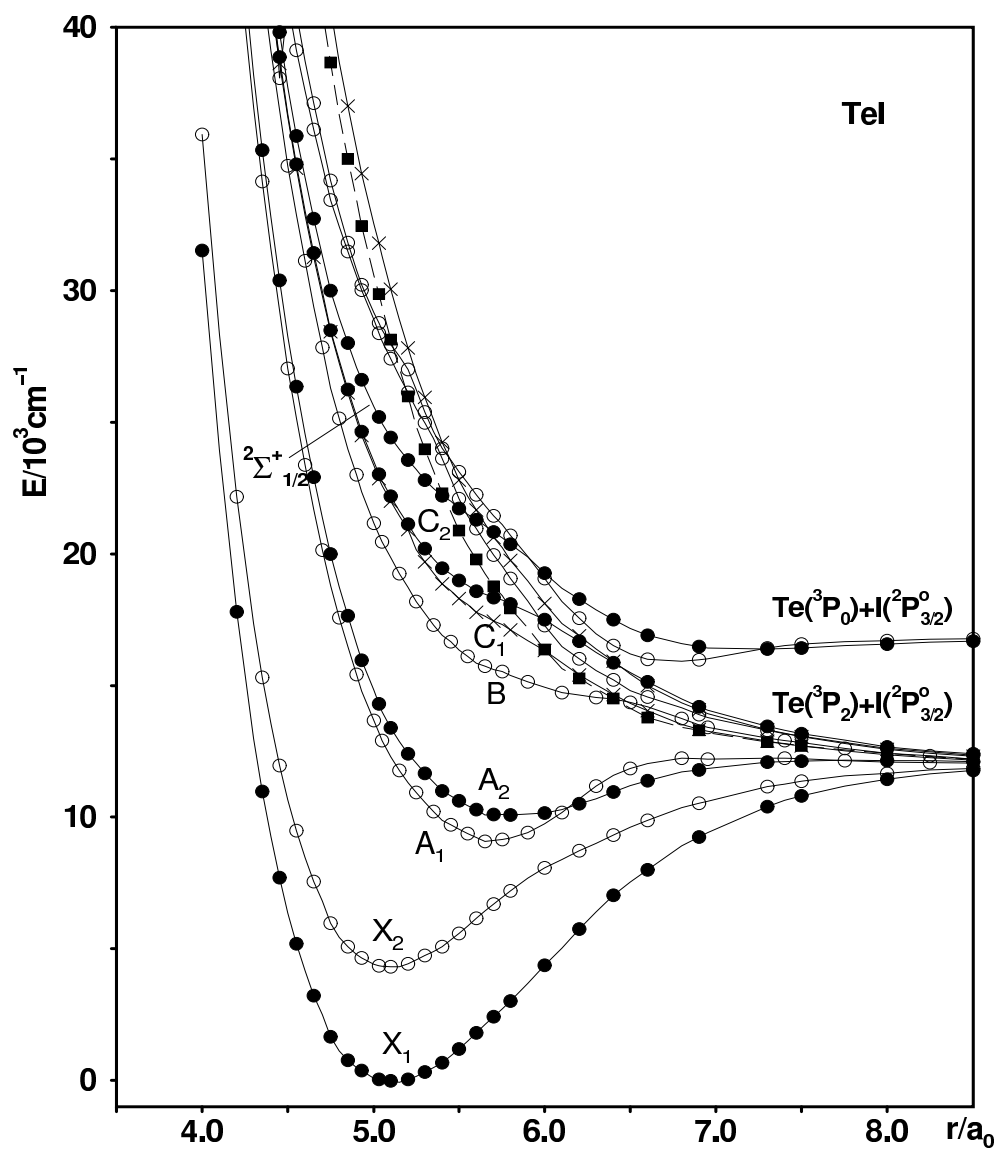


Figure 5.2: Computed potential energy curves for the low-lying Ω states of TeI: \circ - $\Omega = 1/2$ states; \bullet - $\Omega = 3/2$ states; \times - $\Omega = 5/2$ states; and \blacksquare - $\Omega = 7/2$ state.

A states tend to have more SO mixing than the corresponding $3/2$ components. The A_1 $^4\Sigma_{1/2}^-$ state has 11 % $^2\Pi$ and about 5.4 % $^2\Sigma^+$ admixture at its potential minimum. At $r \approx 6.10 a_0$ the A_1 state has predominantly $^2\Pi \Lambda - S$ character with admixture of 31 % $^4\Sigma^-$, 2 % $^2\Sigma^-$, and 1.6 % $^2\Sigma^+$. The X_2 state takes on predominantly $^4\Sigma^- \Lambda - S$ character at the same internuclear distance.

It is interesting to note that the second dissociation limit for the TeI radical is $\text{Te } (^3P_0) + \text{I } (^2P_{3/2}^o)$ rather than $\text{Te } (^3P_0) + \text{I } (^2P_{1/2}^o)$ as in the lighter systems. This is a result of the very strong $\text{I } (^2P_{1/2}^o - ^2P_{3/2}^o)$ splitting, but it has no serious consequences for the behaviour of the low lying states in this system.

5.3 Transition Moments and Radiative Lifetimes

The calculated parallel and perpendicular transition moments for TeI are shown in Figs. 5.3 and 5.4, respectively. As already mentioned, only the ground and the first excited states have attractive potentials, hence the variety of transitions expected in TeF should not be observed in TeI.

As for the lighter halides, the $X_1 - X_2$ fine structure transition is quite weak, with the calculated radiative lifetime for the transition being 62.9 *ms*. The other calculated radiative lifetimes are listed in Table 5.4.

The $A_1 - X_2$ and $A_2 - X_1$ parallel transitions are of comparable strength as in TeCl and TeBr. The parallel transition moment (μ_z) values for the two transitions at the r_e for X and A states are larger than the corresponding values for TeBr and TeCl, but the $\Delta\bar{E}$ values are smaller than in latter two radicals. Hence, the overall effect is that the computed lifetime is nearly the same as in TeCl and TeBr. As already mentioned

Table 5.3: Composition of the four lowest Ω states of TeI (c^2 , %) at various bond distances r . Entries are only made for contributions with $c^2 \geq 1.0$ %.

State	r/a_0	$X^2\Pi$	$B^2\Sigma^-$	$1^2\Sigma^+$	$1^2\Delta$	$A^4\Sigma^-$	$1^4\Sigma^+$	$1^4\Pi$
$X_1^2\Pi_{3/2}$	4.70	99.0						
	5.05 ^a	98.0						
	5.30	96.6				1.3		
	5.70	93.0				3.4		
	6.20	81.9				10.2	2.0	
	7.75	50.2				28.1 ^b	4.5	3.7 ^b
$X_2^2\Pi_{1/2}$	4.70	98.3						
	5.05 ^a	97.4						
	5.30	95.8				1.3		
	5.70	83.7				10.8		
	6.20	14.4	1.5	4.8 ^b		72.3		
	7.75	3.4	3.8 ^b	3.0 ^b		57.3 ^b		25.8 ^b
$A_1^4\Sigma_{1/2}^-$	4.70			7.0		91.3		
	5.05			6.4		91.4		
	5.30	1.4		6.3		90.2		
	5.70 ^a	11.3		5.4		79.9		
	6.20	66.1	6.9			17.4 ^b	1.0	
	7.75	23.6 ^b	38.5 ^b			6.1 ^b	4.8	26.5 ^b
$A_2^4\Sigma_{3/2}^-$	4.70					98.8		
	5.05					97.6		
	5.30	1.2				96.5		
	5.70 ^a	3.2				93.1		
	6.20	8.8				80.1 ^b		5.9 ^b
	7.75	19.0 ^b				31.0 ^b	7.5	37.6 ^b

^a An approximate equilibrium distance for this state.

^b Contributions from the higher-lying roots of this symmetry are included.

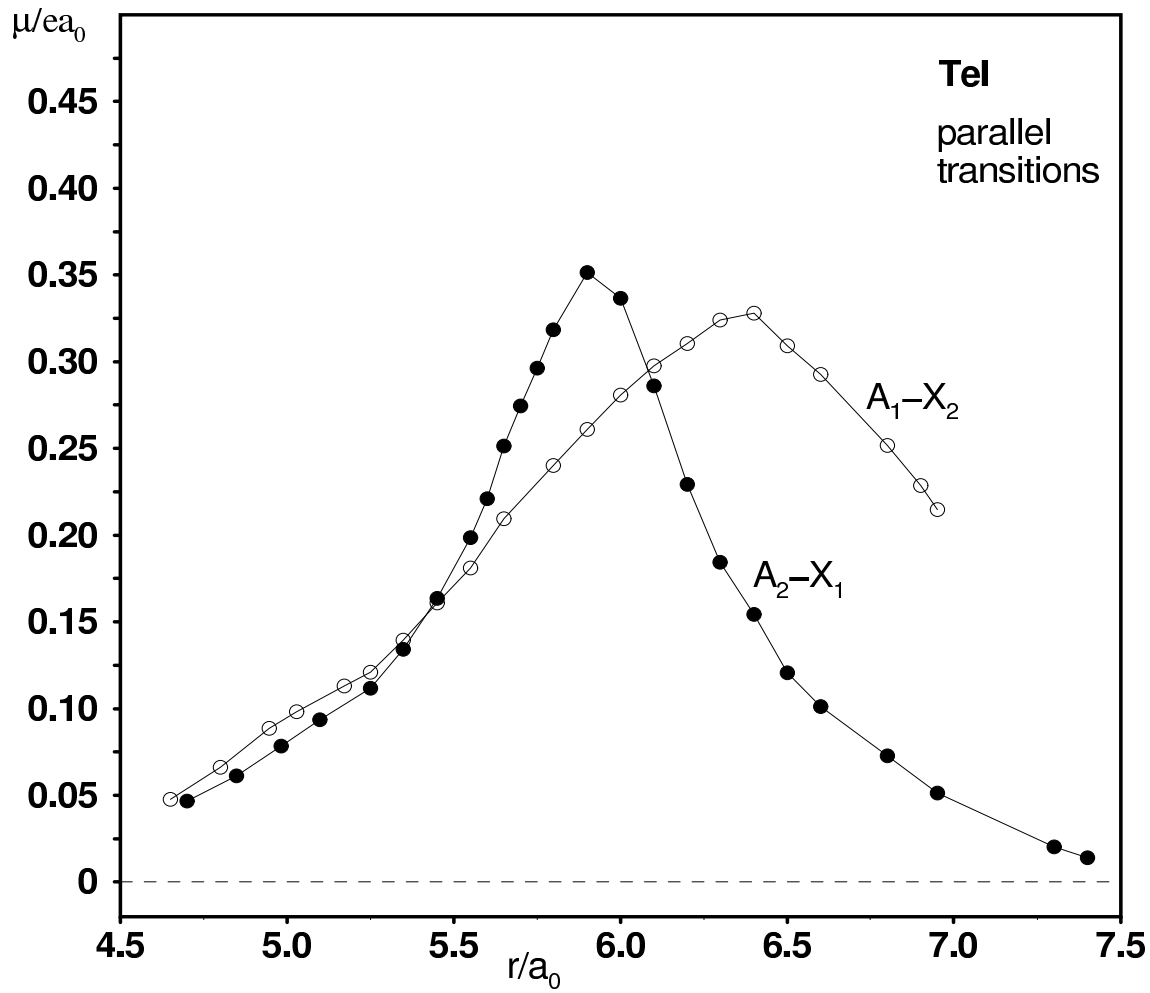


Figure 5.3: Computed electric dipole moments for parallel transitions from the A_1 $4\Sigma_{1/2}^-$ and A_2 $4\Sigma_{3/2}^-$ states to the X_1 $2\Pi_{3/2}$ and X_2 $2\Pi_{1/2}$ states of TeI.

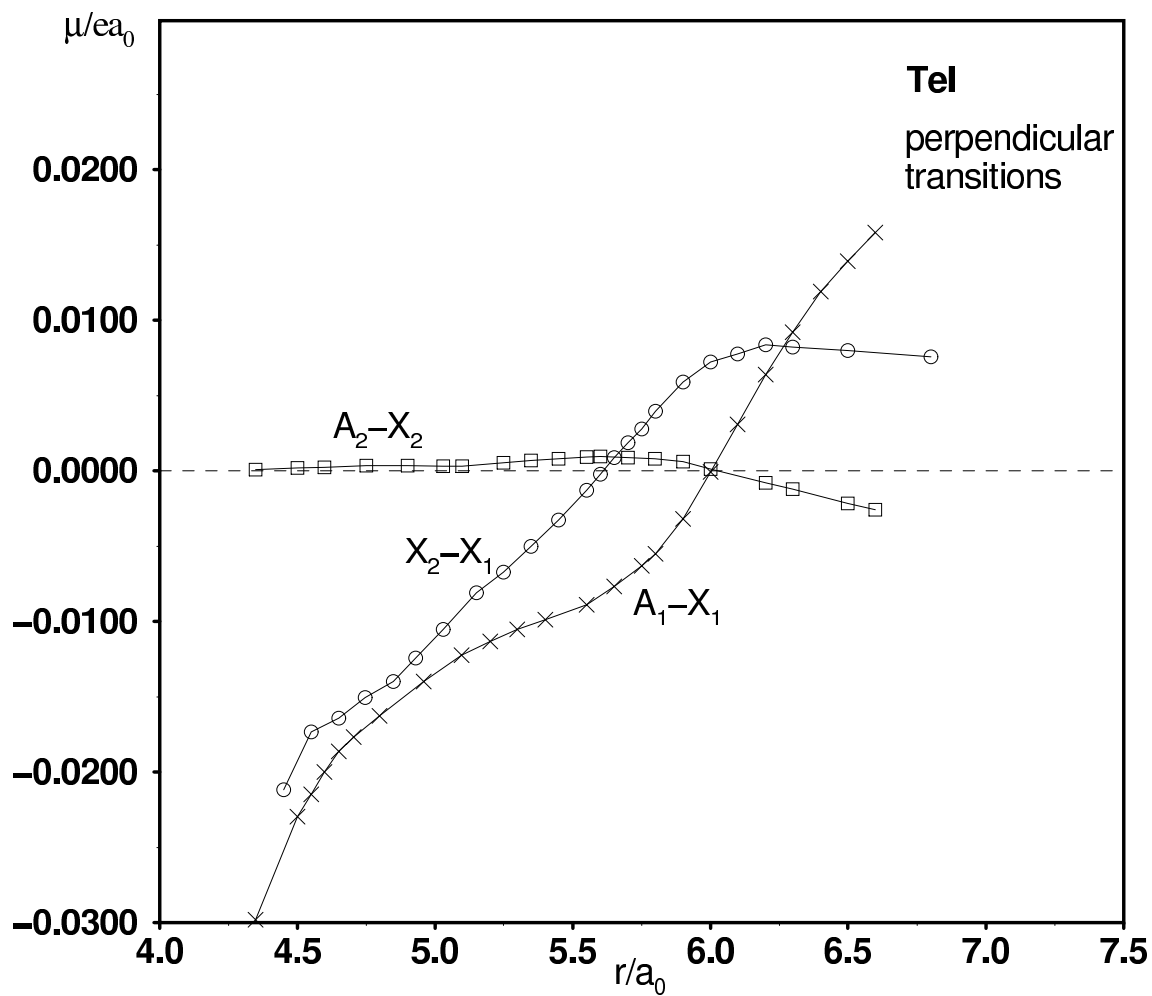


Figure 5.4: Computed electric dipole moments for perpendicular transitions from the X_2 $^2\Pi_{1/2}$, A_1 $^4\Sigma_{1/2}^-$, and A_2 $^4\Sigma_{3/2}^-$ states to the X_1 and X_2 states of TeI.

Table 5.4: Partial and total radiative lifetimes (in s) for transitions from the $v' = 0$ level of the TeI excited states to the $X_1^2\Pi_{3/2}$ (τ_1) and $X_2^2\Pi_{1/2}$ (τ_2) states.

State	τ_1	τ_2			τ_{tot}
		τ_{\perp}	τ_{\parallel}	τ	
$X_2^2\Pi_{1/2}$	62.9 (-3) ^a				62.9 (-3)
$A_1^4\Sigma_{1/2}^-$	22.2 (-3)	2.4	302 (-6)	302 (-6)	298 (-6)
$A_2^4\Sigma_{3/2}^-$	25.2 (-6)	29.7			25.2 (-6)

^a Numbers in parentheses indicate powers of ten.

for the case of TeBr, the $A_1 - X_2$ perpendicular transition is stronger than in the case of TeCl but relatively weak compared to TeF. The reason is the same as for TeBr, namely the μ_x values are comparable in TeF, TeBr and TeI and the difference in the lifetimes is mostly due to the larger $\Delta\bar{E}$ values in the case of TeF.

Since other states in TeI do not possess potential wells deep enough to support any vibrational states, other transitions possible for the lighter monohalides should not be observed in this case.

Conclusion

The series of *ab initio* calculations carried out for the tellurium monohalides, and the analysis of the data thus obtained lead to interesting observations. For example, the first excited state primarily thought of as $^2\Pi$ by experimentalists is found to be a $^4\Sigma^-$, explaining the low intensity of the bands observed; and the B state is actually a $^2\Sigma^-$ instead of $^2\Sigma^+$. Also, the four radicals seem to be almost identical in their character on the surface. They have the same ordering of electronic states, the potential curves are nearly identical in each case, as are the electronic configurations for each state and the excitations leading to them. With so many obvious similarities one would expect hardly any difference to occur in their behaviour.

That the radicals do have significant differences due to the smaller excitation energies in the heavy radicals and the increasing spin-orbit coupling is demonstrated very clearly by the compositions of the various Ω -states obtained after the SO calculations. It is found that the SO coupling has a negligible effect for the low-lying bound states of TeF. The SO effect of the heavy tellurium atom in this case makes itself felt only at large internuclear distances, producing a simple $\Lambda - S$ character of the electronic states in the FC region of TeF. This fact is also reflected in the transition moment values for TeF. For diatomic molecules the parallel transitions ($\Delta\Omega = 0$) are generally more intense than perpendicular transitions. TeF is an exception to this rule because of the almost negligible SO mixing in the FC region. There are only two allowed $\Lambda - S$ transitions

among the low-lying states, namely $B^2\Sigma^-, C^2\Delta \rightarrow X^2\Pi$ and they are perpendicular. The difference between TeF and other monohalides of tellurium becomes evident as soon as one looks at the composition of the Ω states in TeCl, which already exhibits the increasing influence of SO mixing. In the case of the TeCl, TeBr, and TeI radicals, the low-lying electronic states are found to have mixed $\Lambda - S$ character in the FC region. The transition moments corresponding to parallel transitions ($\Delta\Omega = 0$) are found to be much larger than that for perpendicular transitions in these radicals.

A very clear proof of the difference is seen from the $B \rightarrow X_{1,2}$ transitions. The strongest transition in TeF is found to be the perpendicular $B^2\Sigma_{1/2}^- \rightarrow X_1^2\Pi_{3/2}$. In TeI the B state has a repulsive potential and hence this transition is absent. In TeCl and TeBr the B state has a shallow minimum and the $B \rightarrow X$ transitions should give rise to a discrete spectrum. The nature of the transition is, however, quite different from that in TeF. In the heavier monohalides it is the parallel $B^2\Sigma_{1/2}^- \rightarrow X_2^2\Pi_{1/2}$ transition which is the strongest. The $A_{1,2} \rightarrow X_{1,2}$ spectra are dominated by parallel transitions, with the $A_2 \rightarrow X_1$ being the strongest. The A and B states have been experimentally observed in TeF, whereas for TeCl, TeBr, and TeI they are as yet unobserved.

The calculated results are seen to be in very good agreement with the available experimental data. This work has provided a great deal of new information about these lesser-known monohalides. It will be interesting to compare the results reported in the present study with experimental results which hopefully will become available at a later period.

References

- [1] K. P. Huber and G. Herzberg, 1979, *Molecular Spectra and Molecular Structure, Vol.4*, (Princeton, NJ; van Nostrand Reinhold).
- [2] P. F. Bernath and S. McLeod, *DiRef, A Database of References Associated with the Spectra of Diatomic Molecules*, *J. Mol. Spec.* **207**, 287 (2001).
- [3] W. G. Thorpe, W. R. Carper, and S. J. Davis, *J. Chem. Phys.* **83**, 4544 (1985).
- [4] G. A. Oldershaw and K. Robinson, *Chem. Commun.*, 540 (1970).
- [5] G. A. Oldershaw and K. Robinson, *J. Mol. Spec.* **37**, 314 (1971).
- [6] G. A. Oldershaw and K. Robinson, *Trans. Faraday Soc.* **67**, 907 (1971).
- [7] D. E. Newlin, G. W. Stewart, and J. L. Gole, *Can. J. Phys.* **57**, 2217 (1979).
- [8] D. E. Newlin, G. W. Stewart, and J. L. Gole, *Can. J. Phys.* **59**, 441 (1981).
- [9] W. G. Thorpe, W. R. Carper, and S. J. Davis, *J. Chem. Phys.* **83**, 5007 (1985).
- [10] E. H. Fink, K. D. Setzer, D. A. Ramsay, and M. Vervloet, *Chem. Phys. Lett.* **177**, 265 (1991).
- [11] K. Ziebarth, K. D. Setzer, and E. H. Fink, *J. Mol. Spec.* **173**, 488 (1995).
- [12] C. Uibel, (1999), Dissertation, Bergische Universität Wuppertal, Germany.
- [13] G. DiLonardo and A. Trombetti, *Trans. Faraday Soc.* **66**, 2694 (1970).
- [14] S. Roszak, M. Krauss, A. B. Alekseyev, H.-P. Liebermann, and R. J. Buenker, *J. Phys. Chem. A* **104**, 2999 (2000).
- [15] A. B. Alekseyev, H.-P. Liebermann, I. Boustani, G. Hirsch, and R. J. Buenker,

Chem. Phys. 173, 333 (1993).

[16] I. Boustani, S. N. Rai, H.-P. Liebermann, A. B. Alekseyev, G. Hirsch, and R. J. Buenker, Chem. Phys. 177, 45 (1993).

[17] H.-P. Liebermann, I. Boustani, S. N. Rai, A. B. Alekseyev, G. Hirsch, and R. J. Buenker, Chem. Phys. Lett. 214, 381 (1993).

[18] K. K. Das, A. B. Alekseyev, H.-P. Liebermann, G. Hirsch, and R. J. Buenker, Chem. Phys. 196, 395 (1995).

[19] A. B. Alekseyev, K. K. Das, H.-P. Liebermann, R. J. Buenker, and G. Hirsch, Chem. Phys. 198, 333 (1995).

[20] M. K. Gilles, M. L. Pollak, and W. C. Lineberger, J. Chem. Phys. 95, 4723 (1991).

[21] A. B. Alekseyev, H.-P. Liebermann, R. Lingott, R. J. Buenker, and J. S. Wright, Mol. Phys. 91, 777 (1997).

[22] A. B. Alekseyev, H.-P. Liebermann, R. J. Buenker, and D. B. Kokh, J. Chem. Phys. 112, 2274 (2000).

[23] A. B. Alekseyev, H.-P. Liebermann, R. J. Buenker, N. Balakrishnan, H. R. Sadeghpour, S. T. Cornett, and M. J. Cavagnero, J. Chem. Phys. 113, 1514 (2000).

[24] A. B. Alekseyev, H.-P. Liebermann, D. B. Kokh, and R. J. Buenker, J. Chem. Phys. 113, 6174 (2000).

[25] M. Born and J. R. Oppenheimer, Ann. Physik 84, 457 (1927).

[26] J. C. Slater, *Quantum Theory of Matter*, 2nd ed., McGraw-Hill, New York, 1968.

[27] C. C. J. Roothaan, New Developments in Molecular Orbital Theory, Rev. Mod. Phys. 23, 69 (1951).

[28] R. J. Buenker and S. D. Peyerimhoff, Theor. Chim. Acta. 35, 33 (1974); 39, 217 (1976); R. J. Buenker, S. D. Peyerimhoff, and W. Butscher, Mol. Phys. 35, 771 (1978).

[29] E. R. Davidson, in *The World of Quantum Chemistry*, edited by R. Daudel and B. Pullman (Reidel, Dordrecht, 1974) p.17.

[30] S. F. Boys, Proc. Roy. Soc. (London) A201, 125 (1920).

- [31] L. E. McMurchie and E. R. Davidson, *J. Comp. Phys.* 44, 289 (1981).
- [32] J. W. Cooley, *Math. Comput.* 15, 363 (1961).
- [33] M. Perić, R. Runau, J. Römlet, S. D. Peyerimhoff, and R. J. Buenker, *J. Mol. Spec.* 78, 309 (1979).
- [34] L. A. LaJohn, P. A. Christiansen, R. B. Ross, T. Atashroo, and W. C. Ermler, *J. Chem. Phys.* 87, 2812 (1987).
- [35] L. F. Pacios and P. A. Christiansen, *J. Chem. Phys.* 82, 2664 (1985).
- [36] G. Hirsch, P. J. Bruna, S. D. Peyerimhoff, and R. J. Buenker, *Chem. Phys. Lett.* 52, 442 (1977); D. B. Knowles, J. R. Alvarez-Collado, G. Hirsch, and R. J. Buenker, *J. Chem. Phys.* 92, 585 (1990).
- [37] R. J. Buenker, A. B. Alekseyev, H. -P. Liebermann, R. Lingott, and G. Hirsch, *J. Chem. Phys.* 108, 3400 (1998).
- [38] A. B. Alekseyev, H. -P. Liebermann, R. J. Buenker, G. Hirsch, and Y. Li, *J. Chem. Phys.* 100, 8956 (1994).
- [39] I. C. Lane and A. J. Orr-Ewing, *J. Phys. Chem. A* 104, 8759 (2000).
- [40] F. Tamassia, J. M. Brown, and S. Saito, *J. Chem. Phys.* 112, 5523 (2000).
- [41] F. Tamassia, S. M. Kermode, and J. M. Brown, *J. Molec. Spectrosc.* 205, 92 (2001).
- [42] S. Schmidt, Th. Benter, and R. N. Schindler, *Chem. Phys. Lett.* 282, 292 (1998).
- [43] W. H. Howie, I. C. Lane, S. M. Newman, D. A. Johnson, and A. J. Orr-Ewing, *J. Phys. Chem. Chem. Phys.* 1, 3079 (1999).
- [44] I. C. Lane, W. H. Howie, and A. J. Orr-Ewing, *J. Phys. Chem. Chem. Phys.* 1, 3087 (1999).
- [45] A. Toniolo, M. Persico, and D. Pitea, *J. Chem. Phys.* 112, 2790 (2000).
- [46] R. F. Demdahl and K. -H. Gericke, *J. Chem. Phys.* 109, 2049 (1998).
- [47] M. D. Wheeler, S. M. Newman, T. Ishiwata, M. Kawasaki, and A. J. Orr-Ewing, *Chem. Phys. Lett.* 285, 346 (1998).

- [48] Y. Li, J. S. Francisco, and K. A. Peterson, *J. Chem. Phys.* **113**, 8556 (2000).
- [49] B. J. Drouin, C. E. Miller, H. S. P. Müller, and E. A. Cohen, *J. Molec. Spectrosc.* **205**, 128 (2001).
- [50] P. Hassanzadeh, K. K. Irikura, and R. D. Johnson III, *J. Phys. Chem.* **101**, 6897 (2000).
- [51] S. M. Newman, W. H. Howie, I. C. Lane, M. R. Upson, and A. J. Orr-Ewing, *J. Chem. Soc. Faraday Trans.* **94**, 2681 (1998).
- [52] E. H. Fink, private communication.
- [53] J. S. Wright, D. J. Carpenter, A. B. Alekseyev, H.-P. Liebermann, R. Lingott, and R. J. Buenker, *Chem. Phys. Lett.* **266**, 391 (1997).
- [54] A. B. Alekseyev, R. J. Buenker, H.-P. Liebermann, R. Lingott, and G. Hirsch, *J. Chem. Phys.* **100**, 2989 (1994).
- [55] R. J. Buenker and R. A. Philips, *J. Mol. Struct. (THEOCHEM)* **123**, 291 (1985).
- [56] S. Krebs and R. J. Buenker, *J. Chem. Phys.* **103**, 5613 (1995).
- [57] M. M. Hurley, L. F. Pacios, P. A. Christiansen, R. B. Ross, and W. C. Ermler, *J. Chem. Phys.* **84**, 6840 (1986).
- [58] www.webelements.com:80/webelements/compounds/text/Te/l1Te1-12600429.html

List of Tables

2.1	Technical details of the MRD-CI calculations of TeF. ^a	34
2.2	Calculated (this work) and experimental spectroscopic properties of ¹³⁰ TeF (transition energy T_e , bond length r_e , and vibrational frequency ω_e). . . .	38
2.3	Composition of the eight lowest Ω states of TeF (c^2 , %) at various bond distances r . Entries are only made for contributions with $c^2 \geq 1.0$ %. . .	44
2.4	Partial and total radiative lifetimes (in s) for transitions from the $v' = 0$ level of the TeF excited states to the $X_1^2\Pi_{3/2}$ (τ_1) and $X_2^2\Pi_{1/2}$ (τ_2) states.	46
2.5	Calculated partial (τ_{\perp} , τ_{\parallel} , τ) and total (τ_{tot}) radiative lifetimes (in μs) for the $B \rightarrow X_1, X_2$ transitions from the $v' = 0 - 5$ vibrational levels of the upper state.	49
2.6	Partial and total radiative lifetimes (in s) for transitions from the $v' = 0$ level of the TeF $C_{1,2}$ states to the $X_{1,2}$ states at various internuclear distances.	51
3.1	Technical details of the MRD-CI calculations of TeCl. ^a	55
3.2	Calculated (this work) and experimental spectroscopic properties of ¹³⁰ TeCl (transition energy T_e , bond length r_e , and vibrational frequency ω_e). . . .	60
3.3	Composition of the five lowest Ω states of TeCl (c^2 , %) at various bond distances r . Entries are only made for contributions with $c^2 \geq 1.0$ %. . .	62

3.4	Partial and total radiative lifetimes (in s) for transitions from the $v' = 0$ level of the TeCl excited states to the $X_1^2\Pi_{3/2} (\tau_1)$ and $X_2^2\Pi_{1/2} (\tau_2)$ states.	64
4.1	Technical details of the MRD-CI calculations of TeBr. ^a	69
4.2	Calculated (this work) and experimental spectroscopic properties of ¹³⁰ TeBr (transition energy T_e , bond length r_e , and vibrational frequency ω_e).	72
4.3	Composition of the five lowest Ω states of TeBr (c^2 , %) at various bond distances r . Entries are only made for contributions with $c^2 \geq 1.0$ %.	75
4.4	Partial and total radiative lifetimes (in s) for transitions from the $v' = 0$ level of the TeBr excited states to the $X_1^2\Pi_{3/2} (\tau_1)$ and $X_2^2\Pi_{1/2} (\tau_2)$ states.	76
5.1	Technical details of the MRD-CI calculations of TeI. ^a	83
5.2	Calculated (this work) and experimental spectroscopic properties of ¹³⁰ TeI (transition energy T_e , bond length r_e , and vibrational frequency ω_e).	86
5.3	Composition of the four lowest Ω states of TeI (c^2 , %) at various bond distances r . Entries are only made for contributions with $c^2 \geq 1.0$ %.	89
5.4	Partial and total radiative lifetimes (in s) for transitions from the $v' = 0$ level of the TeI excited states to the $X_1^2\Pi_{3/2} (\tau_1)$ and $X_2^2\Pi_{1/2} (\tau_2)$ states.	92

List of Figures

2.1	Computed potential energy curves for the low-lying $\Lambda - S$ states of TeF obtained without inclusion of spin-orbit interaction.	37
2.2	Computed potential energy curves for the low-lying Ω states of TeF: $\circ - \Omega = 1/2$ states; $\bullet - \Omega = 3/2$ states; $\times - \Omega = 5/2$ states; and $* - \Omega = 7/2$ state.	39
2.3	Computed electric dipole moments for parallel transitions from the $A_1^4\Sigma_{1/2}^-$, $A_2^4\Sigma_{3/2}^-$, and $B^2\Sigma_{1/2}^-$ states to the $X_1^2\Pi_{3/2}$ and $X_2^2\Pi_{1/2}$ states of TeF.	47
2.4	Computed electric dipole moments for perpendicular transitions from the $X_2^2\Pi_{1/2}$, $A_1^4\Sigma_{1/2}^-$, $A_2^4\Sigma_{3/2}^-$, $B^2\Sigma_{1/2}^-$, $C_1^2\Delta_{5/2}$, and $C_2^2\Delta_{3/2}$ states to the X_1 and X_2 states of TeF.	48
3.1	Computed potential energy curves for the low-lying $\Lambda - S$ states of TeCl obtained without inclusion of the spin-orbit interaction.	57
3.2	Computed potential energy curves for the low-lying Ω states of TeCl: $\circ - \Omega = 1/2$ states; $\bullet - \Omega = 3/2$ states; $\times - \Omega = 5/2$ states; and $\blacksquare - \Omega = 7/2$ state.	59
3.3	Computed electric dipole moments for parallel transitions from the $A_1^4\Sigma_{1/2}^-$, $A_2^4\Sigma_{3/2}^-$, and $B^2\Sigma_{1/2}^-$ states to the $X_1^2\Pi_{3/2}$ and $X_2^2\Pi_{1/2}$ states of TeCl.	63

3.4	Computed electric dipole moments for perpendicular transitions from the $X_2^2\Pi_{1/2}$, $A_1^4\Sigma_{1/2}^-$, $A_2^4\Sigma_{3/2}^-$, and $B^2\Sigma_{1/2}^-$ states to the X_1 and X_2 states of TeCl.	65
4.1	Computed potential energy curves for the low-lying $\Lambda - S$ states of TeBr obtained without inclusion of spin-orbit interaction.	71
4.2	Computed potential energy curves for the low-lying Ω states of TeBr: $\circ - \Omega = 1/2$ states; $\bullet - \Omega = 3/2$ states; $\times - \Omega = 5/2$ states; and $\blacksquare - \Omega = 7/2$ state.	73
4.3	Computed electric dipole moments for parallel transitions from the $A_1^4\Sigma_{1/2}^-$, $A_2^4\Sigma_{3/2}^-$, and $B^2\Sigma_{1/2}^-$ states to the $X_1^2\Pi_{3/2}$ and $X_2^2\Pi_{1/2}$ states of TeBr.	77
4.4	Computed electric dipole moments for perpendicular transitions from the $X_2^2\Pi_{1/2}$, $A_1^4\Sigma_{1/2}^-$, and $A_2^4\Sigma_{3/2}^-$ states to the X_1 and X_2 states of TeBr.	78
5.1	Computed potential energy curves for the low-lying $\Lambda - S$ states of TeI obtained without inclusion of the spin-orbit interaction.	85
5.2	Computed potential energy curves for the low-lying Ω states of TeI: $\circ - \Omega = 1/2$ states; $\bullet - \Omega = 3/2$ states; $\times - \Omega = 5/2$ states; and $\blacksquare - \Omega = 7/2$ state.	87
5.3	Computed electric dipole moments for parallel transitions from the $A_1^4\Sigma_{1/2}^-$ and $A_2^4\Sigma_{3/2}^-$ states to the $X_1^2\Pi_{3/2}$ and $X_2^2\Pi_{1/2}$ states of TeI.	90
5.4	Computed electric dipole moments for perpendicular transitions from the $X_2^2\Pi_{1/2}$, $A_1^4\Sigma_{1/2}^-$, and $A_2^4\Sigma_{3/2}^-$, states to the X_1 and X_2 states of TeI.	91